Analytical and Numerical Advances in Radial Basis Functions

by

Cécile Piret

B.S., Metropolitan State College of Denver, 2002

M.S., University of Colorado at Boulder, 2005

A thesis submitted to the

Faculty of the Graduate School of the

University of Colorado in partial fulfillment

of the requirements for the degree of

Doctor of Philosophy

Department of Applied Mathematics

2007

This thesis entitled:
Analytical and Numerical Advances in Radial Basis Functions
written by Cécile Piret
has been approved for the Department of Applied Mathematics

Prof. Bengt Fornberg

Prof. Tom Manteuffel

Dr. Natasha Flyer

Prof. James Curry

Prof. Ben Herbst

Date

The final copy of this thesis has been examined by the signatories, and we find that both the content and the form meet acceptable presentation standards of scholarly work in the above mentioned discipline.

Piret, Cécile (Ph.D., Applied Mathematics)

Analytical and Numerical Advances in Radial Basis Functions

Thesis directed by Prof. Bengt Fornberg

The radial basis functions (RBF) method is meshfree, easy to implement in any number of dimensions and spectrally accurate for certain types of radial functions. However, it still has stability and complexity issues which keep it from being used more widely. In this dissertation, we study problems related to the complexity and stability properties of the RBF method. In particular, we first study the locality property of the RBFs expansion coefficients. We are able to show and quantify how a perturbation in the function value at one node will affect expansion coefficients associated with only the neighboring nodes. This locality property is a key in the development of fast iterative methods (Powell, Faul, etc.), and our study is valuable in a time where the lack of a generally applicable fast algorithm is one of the biggest obstacles that the RBF methodology is facing. We also study the role of the shape parameter on the stability of the method. It has been known for quite some time that certain nice properties (especially high accuracy) are linked with flat RBF interpolants (small values of the shape parameter). However, the lack of stability associated with small shape parameters has lead people to believe that computations of the interpolant in this regime of the shape parameter were impossible. Fornberg and Wright developed the first tool (the Contour-Padé algorithm) to get around the instability and thereby disprove the phenomenon described by Schaback as the "uncertainty principle." We present a second algorithm, which we call the RBF-QR algorithm. It is also designed to stably compute interpolants in the case of flat RBFs, but is easier to implement and doesn't have restrictions on the number of nodes. We use this tool to study the role of the shape parameter on the error when interpolating as well as when solving a convection equation on the sphere.

Dedication

A mes parents, Marguerite et Jean-Marie Piret-Raskin.

Acknowledgements

I first and foremost wish to express gratitude to my adviser, Professor Bengt Fornberg, for his mentoring and for his kind support and understanding. I also wish to thank Dr. Natasha Flyer for her generosity and sensitivity, and for her wonderful advice. They are both examples in my life.

Je remercie mes parents et ma soeur pour m'avoir apporté le goût et l'ambition des études, et surtout, pour m'avoir offert un soutien impérissable qui m'a permis de vivre ma passion jusqu'au bout. Je remercie aussi pour leur soutien mon parrain Jean-Marie Raskin et son épouse Christiane, aussi pour m'avoir donné l'amour des sciences et des mathématiques. Et je remercie Cédric Delvaux pour être et avoir été mon ami et mon frère à travers les épreuves de la vie.

I am grateful for the brilliant, inspiring and wonderful people who I have been lucky to meet throughout my years in Colorado: Dr. Nancy Thompson, Dr. Linda Sundbye, and of course, Dr. Mark Hoefer, Cynthia Cappel, Jill Pilon, and Pamela and Pema Anain.

I want to express my gratitude to the remainder of my committee: Professors Tom Manteuffel, Jim Curry, and Ben Herbst. Their help and support have been invaluable.

Finally, I wish to thank Professor Bengt Fornberg for his quote "If you're not in a state of sheer panic at least 20% of the time, then you're not doing good research", as it saved me from countless instances of complete despair.

Contents

Chapter

Tables

Table

Figures

Figure

Chapter 1

Introduction

This dissertation describes the four main research projects on which the author has worked in the past two years. All four projects treat different aspects of the radial basis functions (RBF) method. The papers which resulted from these projects have been included as appendices. The first chapter will give an introduction to the RBF method. Each following chapter will describe one project, give the motivation behind it, a summary of the resulting paper, and will include results that, for a reason or another, did not find a place in the submitted version of the paper. The work presented here was done in collaboration with our RBF research group members Prof. Bengt Fornberg, Dr. Natasha Flyer and Susan (Tyger) Hovde. The main contributors to the different results covered in this thesis will be indicated with their initials. As of now, the paper entitled "Localization properties of RBF expansion coefficients for cardinal interpolants. I. Equispaced nodes" (B. Fornberg, N. Flyer, S. Hovde and C. Piret) is accepted in IMA Journal on Numerical Analysis. "A stable algorithm for flat radial basis functions on a sphere" (Bengt Fornberg and Cécile Piret) has appeared in SIAM J. Sci. Comp. "On choosing a radial basis function and a shape parameter when solving a convective PDE on a sphere" (Bengt Fornberg and Cécile Piret) has been accepted by the Journal of Computational Physics.

1.1 History of RBFs

The RBF methodology was introduced in 1971 by Rolland Hardy [25]. He originally presented the method for the multiquadric (MQ) radial function. The method emerged from a cartography problem, where a bivariate interpolant of sparse and scattered data was needed to represent topography and produce contours. None of the existing interpolation methods (e.g. Fourier, polynomial, bivariate splines) were satisfactory because they were either too smooth or too oscillatory. Furthermore, the non-singularity of their interpolation matrices was not guaranteed. In fact, Haar's theorem states the existence of a set of distinct nodes for which the interpolation matrix associated with node-independent basis functions is singular in two or higher dimensions [33]. In 1982, Richard Franke popularized the MQ method with his report on 32 of the most commonly used interpolation methods [23]. He subjected those methods to thorough tests, and found the MQ method overall to be the best one. Franke also conjectured the unconditional non-singularity of the interpolation matrix associated with the multiquadric radial function, but it was not until a few years later, in 1986, that Charles Micchelli [34] was able to prove it, making use of work by Schoenberg from the 30s and 40s.

The main feature of the MQ method is that the interpolant is a linear combination of translations of a basis function which only depends on the Euclidean distance from its center. This basis function is therefore radially symmetric with respect to its center. The MQ method was generalized to other "radial functions", such as the thin plate spline [9], the gaussian, the cubic, etc. and the method was called the 'Radial Basis Function' method. In the 1990s the RBF methodology was once again brought to the spotlight when Ed Kansa introduced a way to use it for solving parabolic, elliptic and (viscously damped) hyperbolic PDEs [27], [28].

Name of RBF	Abbreviation	$\phi(r), r \geq 0$	Smoothness
multiquadric	MQ	$\sqrt{1+(\varepsilon r)^2}$	Infinitely smooth
inverse multiquadric	IMQ	$\frac{1}{\sqrt{1+(\varepsilon r)^2}}$	
inverse quadratic	IQ	$\frac{1}{1+(\varepsilon r)^2}$	
Generalized multiquadric	GMQ	$(1+(\varepsilon r)^2)^{\beta}$	
Gaussian	GA	$e^{-(\varepsilon r)^2}$	
Thin Plate Spline	TPS	$r^2 \log(r)$	Piecewise smooth
Linear	LN	r	
Cubic	CU	r^3	
Monomial	MN	r^{2k-1}	

Table 1.1: Definitions of some radial functions.

1.2 Formulation of the interpolation problem

A radial basis function interpolant takes the form

$$s(\underline{x}) = \sum_{i=1}^{n} \lambda_i \, \phi(\|\underline{x} - \underline{x}_i\|), \tag{1.1}$$

when we interpolate data values f_i at the scattered node locations $\underline{x}_i$, $i = 1, 2, \ldots n$ in d dimensions, and where $\|\cdot\|$ denotes the Euclidean 2-norm.

We obtain the expansion coefficients λ_i by solving a linear system $A\,\underline{\lambda} = \underline{f}$, based on the interpolation conditions $s(\underline{x}_i) = f_i$. The system takes the form

$$\begin{bmatrix} \phi(\|\underline{x}_1 - \underline{x}_1\|) & \phi(\|\underline{x}_1 - \underline{x}_2\|) & \cdots & \phi(\|\underline{x}_1 - \underline{x}_n\|) \\ \phi(\|\underline{x}_2 - \underline{x}_1\|) & \phi(\|\underline{x}_2 - \underline{x}_2\|) & & \phi(\|\underline{x}_2 - \underline{x}_n\|) \\ \vdots & & & \vdots \\ \phi(\|\underline{x}_n - \underline{x}_1\|) & \phi(\|\underline{x}_n - \underline{x}_2\|) & \cdots & \phi(\|\underline{x}_n - \underline{x}_n\|) \end{bmatrix} \begin{bmatrix} \lambda_1 \\ \lambda_2 \\ \vdots \\ \lambda_n \end{bmatrix} = \begin{bmatrix} f_1 \\ f_2 \\ \vdots \\ f_n \end{bmatrix} \tag{1.2}$$

There are two kinds of radial functions, the piecewise smooth and the infinitely smooth radial functions. For the infinitely smooth radial functions, we have a shape parameter, ε. The closer this parameter is to 0, the flatter the radial function becomes. Table 1.1 contains a list of the most widely used radial functions $\phi(r)$.

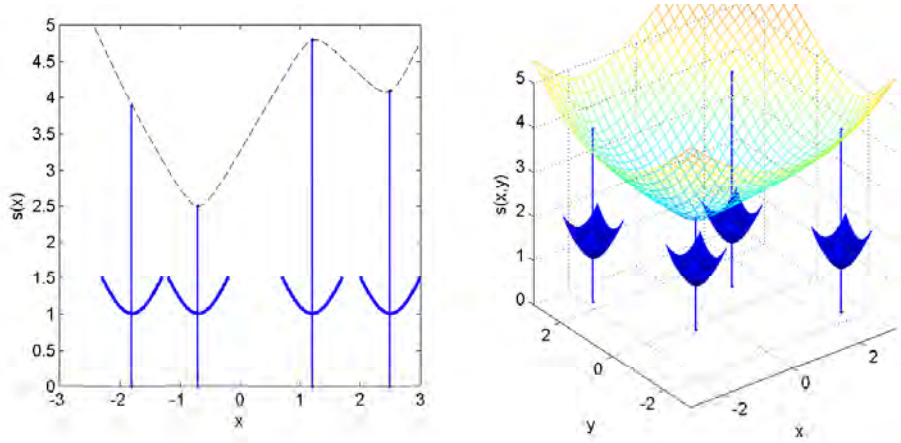

Figure 1.1: The RBF method consists in centering a radial function at each node location and imposing that the interpolant takes the node's associated function value.

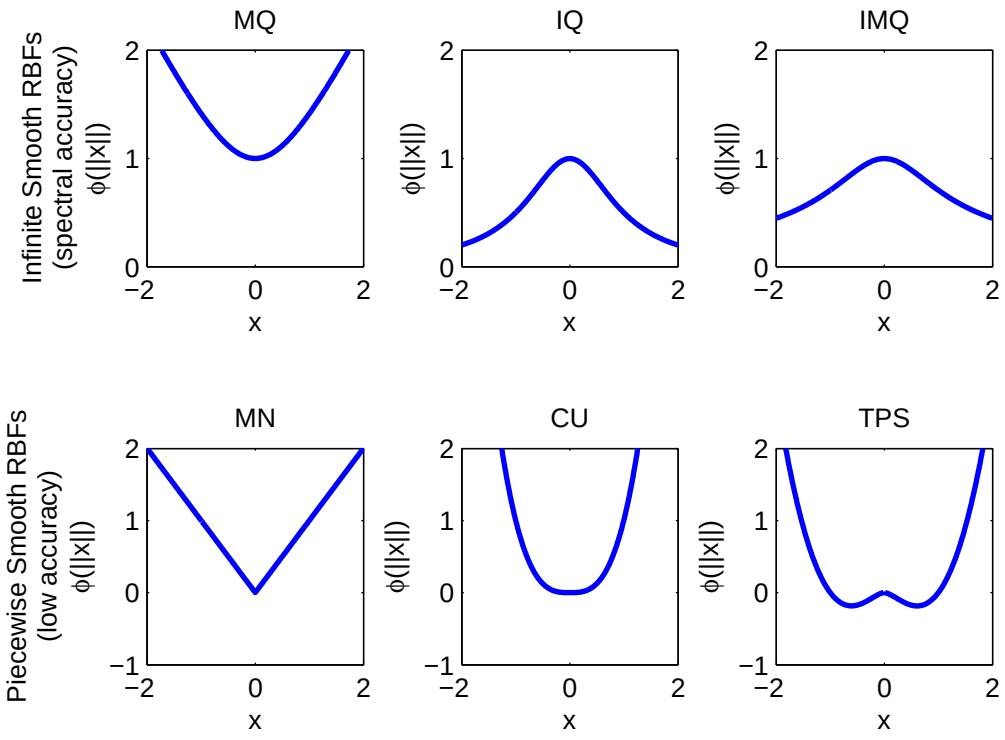

Figure 1.2: The most commonly used radial functions. The piecewise smooth RBFs only give rise to low accuracy while the infinitely smooth RBFs provide spectral accuracy. MN is shown in the case of $k = 1$, i.e. $\phi(r) = r$.

1.3 Properties of RBFs as an interpolant

1.3.1 Accuracy

The cubic radial function $\phi(r) = r^3$, producing a cubic spline interpolant in 1-D and has a jump in its 3rd derivative and its interpolant is $O(h^4)$ accurate (h is inversely proportional to the number of node points, n. It can be thought of as the typical node distance, since no grid is required.) The quintic radial function, $\phi(r) = r^5$, has a jump in its 5th derivative and leads to an $O(h^6)$ accurate interpolant. In general, the MN radial function $\phi(r) = r^{2k-1}$ has a jump in its $2k-1$st derivative and its interpolant will be $O(h^{2k})$ accurate. Thus, the smoothness of the radial function is the key factor behind the accuracy of its interpolant. The piecewise continuous radial functions therefore converge algebraically towards the interpolated function, as we increase the number of node points. We note here that a radial function could not take the form $\phi(r) = r^{2k}$ since it could interpolate a maximum of 2k+1 nodes (in 1-D), due to the fact that the resulting interpolant reduces to a polynomial of degree $2k$. On the other hand, a radial function which is infinitely continuously differentiable (and not of polynomial form) will produce a spectrally accurate interpolant, which converges as $O(e^{-\frac{const}{h}})$ towards the interpolated function, if no counterpart to the Runge phenomenon enters [22]. The Gaussian RBF is an exception to the rule, as it converges as $O(e^{-\frac{const}{h^2}})$, i.e.'super-spectrally' [15]. The accuracy of the infinitely smooth radial functions also depends on their shape parameter and can be improved by changing the flatness of the radial function. The limit of $\varepsilon \to 0$, has become very interesting in that respect. The range of small ε used to be inaccessible because of the ill-conditioning that it caused. Since the introduction of the Contour-Padé method, developed by Fornberg and Wright [20], this obstacle commonly known as 'the uncertainty principle' was lifted and it was finally possible to explore the features of the small ε RBFs [21], [44], [29], [30]. In fact, in the limit of $\varepsilon \to 0$, the RBF interpolant in 1-D was found to converge towards

the Lagrange interpolation polynomial, and thereby reproduce the traditional spectral methods such as Fourier and Chebyshev, if the node locations are chosen accordingly [8]. We observe that, for a fixed n, the error (when interpolating smooth functions) decreases exponentially as ε decreases, until $\varepsilon = \varepsilon_{opt}$, at which point the Runge phenomenon picks up and increases the error or halts further error reductions [22].

1.3.2 Stability

The stability can be a serious concern when using the RBF method. Although the non-singularity of the collocation matrix is guaranteed for all of the smooth RBF choices mentioned (MQ, IMQ, IQ, GA, etc.), no matter how the nodes are scattered in any number of dimension, its condition number tends to increase with the number of node points, making it very difficult or impossible to find the interpolant. In the case of the infinitely smooth radial functions, stability is also dependent on their shape parameter. The interpolant belongs to the space spanned by radial function translates centered at each node point. When the shape parameter is close to 0, all those translates become flat, and thus highly linearly dependent with each other. The system then becomes severely ill-conditioned.

1.3.3 Computational cost

Computational cost is another issue linked to using radial basis functions. Smooth radial functions are global, thus the collocation matrices associated to them are dense. Because of the necessity to invert this matrix, the direct implementaion via (1.1) and (1.2) has an $O(n^3)$ complexity. Although various efforts are underway to speed up the process ([7] and [11]), the lack of a widely applicable, robust and fast algorithm is a significant drawback in using RBFs. On the other hand, the algorithm is identical when interpolating in any number of dimensions, i.e. the complexity doesn't grow with the dimension, which is a big advantage in using RBFs.

1.4 RBFs for solving PDEs

Ed Kansa was the first to use the RBF method to solve PDEs. His method consisted in approximating spatial partial derivatives by differentiating smooth RBF interpolants to solve parabolic, elliptic, and viscously damped hyperbolic PDEs to spectral accuracy, in a completely mesh-free manner [27].

1.5 The holy grail of RBFs: The 'unattainable' flat limit

We saw earlier that the flatter the radial function, the more ill-conditioned the system becomes. Finding the 'optimal' shape parameter has for a long time been a major theme in RBF research. For many years, the optimal shape parameter was usually chosen to be the smallest one not severely affected by ill-conditioning, because generally, flatter radial functions gave rise to a better interpolation space. However, this trend was at some 'optimal' point interrupted by the worsening conditioning of the system. Buhmann was the first to give some theoretical importance to the flat limit, although it was viewed as unattainable, both because of ill-conditioning and because his results were specific to infinite lattices. In 1995, Robert Schaback introduced the term 'uncertainty principle', or 'trade-off principle' to identify the seemingly necessary trade-off between accuracy and acceptable conditioning of the RBF method (See Chapter 3). He proved that it was impossible to have simultaneously flat or near-flat basis functions and a well-conditioned matrix. However, without him noticing the distinction, his proof concerned more the 'direct' RBF method (via (1.1) and (1.2)) than the RBF method in itself. In 2002, Driscoll and Fornberg [8] showed not only the flat limit of the interpolant exists but that it is well behaved. In fact, in the flat limit, the RBF interpolant in 1-D converges towards the Lagrange interpolating polynomial. This result was later generalized to more dimensions [21]. Consequently, it was shown that this flat limit is a generalization to irregular domains and scattered nodes to the PS methods. In 2004,

Fornberg and Wright disproved completely the notion of the 'uncertainty principle', which had started to fade after Driscoll and Fornberg's results of 2002, by introducing the very first algorithm that allowed a stable computation of the interpolant in the flat radial functions regime, the Contour-Padé method [20]. It was finally possible to explore the errors produced by flat or near-flat radial functions. It resulted in the new insight that, although the interpolation space became better as the radial functions became flat, there emerged again another 'flatness' threshold, after which the error was either flat or increasing. This one was not due to ill-conditioning anymore but to the Runge phenomenon [22]. Indeed, the Runge phenomenon is prominent in high degree polynomial interpolation, thus also in flat RBF interpolation since one is the limiting value of the other. Also, the Contour Padé method only works on a limited amount of nodes, which lead Fassauher to note another "trade-off" of accuracy and stability versus the problem size [10]. In 2006, Fornberg and Zuev introduced the variable shape parameter RBF method [22], which was designed to reduce the Runge phenomenon. Finally, Fornberg and Piret [18] introduced the RBF-QR method, designed just like the Contour-Padé method to go past the ill-conditioning 'barrier' of the radial functions, but this time, without the limit on node numbers, thus destroying also the concept of Fassahuer's trade-off. Not only was this RBF-QR method applied to interpolation (Chapter 3), it was also later used to generalize Flyer and Wright's results on solving a purely convective type PDE on the surface of the sphere (Chapter 4), and it was after that modified to allow for variable shape parameters (Chapter 5). This revolutionary method is the main subject of this dissertation.

1.6 RBF theory

The direct method (RBF-Direct) as expressed in (1.1) and (1.2) entails inverting the collocation matrix A in order to find the expansion coefficients, thus the RBF interpolant. As it was mentioned earlier, the non-singularity of the RBF collocation

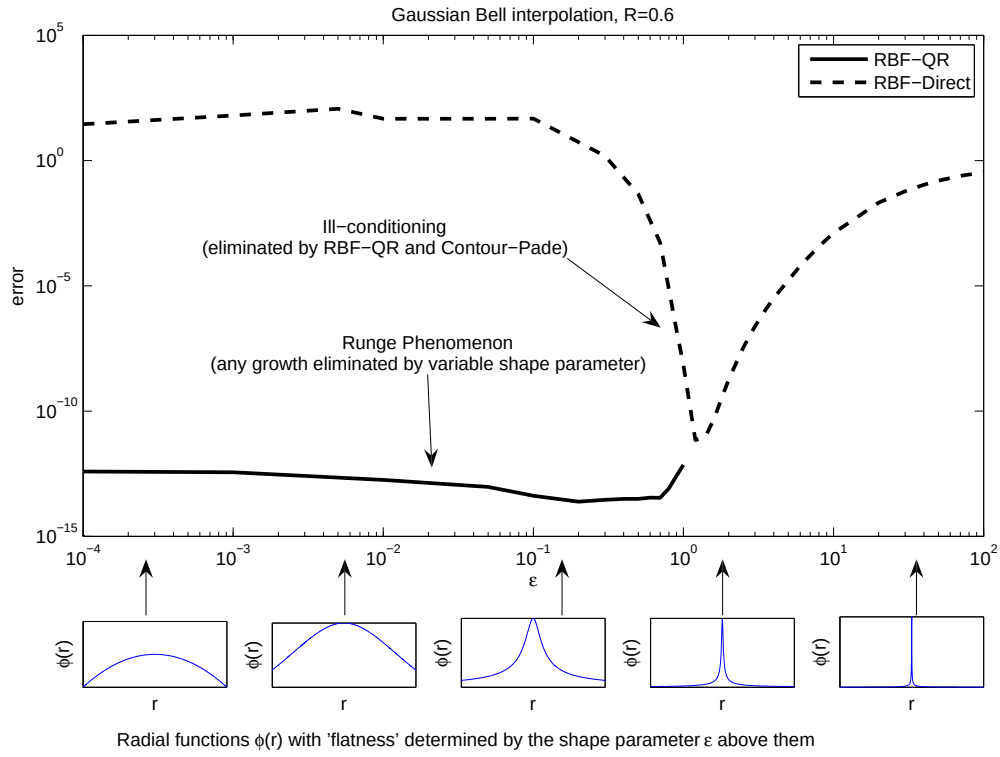

Figure 1.3: Illustration of the typical behavior of the interpolation error (and the method that prevents it into parentheses) in function of the shape parameter (in this case, with the IMQ radial function).

matrices is a huge incentive to using the RBF method. We now consider the invertibility of the collocation matrices associated with the most common radial functions. The proof of this key feature was completed in two stages. First, Schoenberg in 1938 proved the unique solvibility of (1.2) for a small class of radial functions. Then, Micchelli in 1986 extended Schoenberg's results to a larger class of functions, which includes more popular ones, such as the MQ or the TPS RBFs. In addition to [34] and to [41], we use the following sources for this section: [10], [38], [43].

1.6.1 The 'basic' RBF method (1.2)

We will call 'basic', the RBF method characterized by (1.2). It gives an expression for the interpolant on the condition that the system (1.2) is uniquely solvable. In 1938, Schoenberg proved in the set of theorems presented next, that a certain class of radial functions, the completely monotonic functions, gives rise to strictly positive definite, thus unconditionally non-singular collocation matrices.

Definition: Positive Definite Matrices A real symmetric matrix A is called *strictly positive definite* if its associated quadratic form is positive

$$\sum_{j=1}^{n}\sum_{k=1}^{n} c_j c_k A_{jk} > 0 \tag{1.3}$$

for all non-vanishing $\underline{c} \in R^n$. Consequently, the eigenvalues of a positive definite matrix are all strictly positive.

Theorem 1 Assume that d is any positive integer and that the points $\underline{x}_i \in R^d$, $i = 1, 2, ..., n$, are all distinct. If ϕ can be written in the form

$$\phi(r) = \int_0^\infty e^{-\alpha r^2} w(\alpha) d\alpha, \tag{1.4}$$

where $w(\alpha) \geq 0$ for $\alpha \geq 0$ and $\int_\delta^\infty w(\alpha)d\alpha > 0$ for some $\delta > 0$, then the collocation matrix A with entries $A_{i,j} = \phi(\|\underline{x}_i - \underline{x}_j\|)$ is positive definite.

Definition: Completely monotonic functions A function $\phi(r) = \int_0^\infty e^{-\alpha r^2} w(\alpha) d\alpha$, $r \geq 0$, where $w \geq 0$ is said to be *completely monotonic on* $[0, \infty)$ if, when considering

$$\psi(r) = \phi(r^{1/2}) = \int_0^\infty e^{-\alpha r} w(\alpha) d\alpha. \tag{1.5}$$

- $\psi(r) \geq 0$, and
- $(-1)^k \psi^{(k)}(r) \geq 0$, $r \geq 0$ for all positive integers k.

Theorem 2 $\phi(r)$ can be expressed as $\int_0^\infty e^{-\alpha r^2} w(\alpha) d\alpha$ *if and only if* $\psi(r) \geq 0$, $r \geq 0$ is completely monotonic.

Examples of completely monotonic functions

- GA: $\phi(r) = e^{-\varepsilon^2 r^2}$
- Generalized IMQ: $\phi(r) = (1 + \varepsilon^2 r^2)^\beta$, $\beta < 0$

By the fact that these radial functions are completely monotonic, they give rise to strictly positive definite collocation matrices.

However, Theorem 2 does not apply to radial functions such as LN, MQ or TPS. Franke conjectured the non-singularity of the interpolation matrix associated with the excellent MQ radial functions, but it was only in 1986 that Micchelli completed the proof for LN and MQ radial functions with the RBF representation (1.2).

Theorem 3 Let $\psi(r) = \phi(r^{1/2}) \in C^0[0, \infty), \psi(r) > 0$ for $r > 0$, and $\psi'(r)$ completely monotone but not constant on $(0, \infty)$. Then, for any set of n distinct points $\{\underline{x}_j\}_{j=1}^n$, the nxn matrix A with entries $A_{i,j} = \phi(\|\underline{x}_i - \underline{x}_j\|)$ is non-singular. Furthermore, for $n \geq 2$, the matrix has $n - 1$ negative eigenvalues and one positive eigenvalue.

Examples of radial functions to which Theorem 3 applies

- LN : $\phi(r) = r$

- MQ : $\phi(r) = (1 + \varepsilon^2 r^2)^{1/2}$

So, although these radial functions do not give rise to strictly positive definite matrices, they nonetheless give rise to invertible matrices, permitting the interpolant to be uniquely solvable unconditionally via (1.2).

1.6.2 The augmented RBF method

Radial functions such as TPS do not satisfy the necessary conditions for either Theorems 2 or 3 to hold. In fact, when using the TPS RBF, there exist node sets which produce a singular collocation matrix. In order to have sufficient conditions for a non-singular system, Micchelli added restrictions, new requirements on top of (1.2) and thereby introduced the *augmented RBF method*

Definition: The augmented RBF method The RBF interpolant of the given data values f_i at the scattered node locations $\underline{x}_i$, $i = 1, 2, \ldots n$ in d dimensions, now takes the form

$$s(\underline{x}) = \sum_{i=1}^{n} \lambda_i \, \phi(\|\underline{x} - \underline{x}_i\|) + \sum_{k=1}^{\tilde{m}} \mu_j p_j(\underline{x}), \underline{x} \in R^d, \tag{1.6}$$

with the additional constraint that

$$\sum_{j=1}^{n} \lambda_j p_k(\underline{x}_j) = 0, k = 1, 2, ..., M \tag{1.7}$$

with $\{p_j : j = 1, 2, ..., \tilde{m}\}$ a basis for Π_{m-1} (the space of the polynomials of degree at most m-1 from R^d to R), and $m \in N$ defined later.

The equivalent matrix equation to (1.6) takes the form

$$\left[\begin{array}{c|c} A & P \\ \hline P^T & 0 \end{array}\right] \left[\begin{array}{c} \lambda \\ \hline \mu \end{array}\right] = \left[\begin{array}{c} f \\ \hline 0 \end{array}\right] \tag{1.8}$$

where matrix A is the collocation matrix defined in (1.2) and where matrix P is $\tilde{m}$xn and $P_{ij} = p_i(\underline{x}_j)$, $i = 1, 2, ..., \tilde{m}$, $j = 1, 2, ..., n$.

Theorem 4 Let $\psi(r) = \phi(r^{1/2}) \in C^0[0,\infty), \psi(r) > 0$ for $r > 0$, and $\psi^{m+1}(r)$ completely monotone but not constant on $(0,\infty)$, for $m \geq 0$. Then, for any set of n distinct points $\{\underline{x}_j\}_{j=1}^n$ that satisfy the condition $rank(P) = \tilde{m}$, where P is the $\tilde{m} \times n$ matrix in 1.8, the $(n+\tilde{m})$x$(n+\tilde{m})$ matrix in 1.8 is non-singular. Furthermore, if $\bar{m}$ is the smallest m such that $\psi^{m+1}(r)$ is completely monotone, then for any non-zero vector $\alpha \in R^n$ that satisfies the condition $P^T\alpha = 0$, the following relation holds $(-1)^{\bar{m}+1}\alpha^T A\alpha > 0$, where A is the nxn matrix in (1.2).

Examples of radial functions that can now be considered

- TPS : $\phi(r) = r^{2k}Log(r)$ $(m = k+1)$
- Generalized MQ : $\phi(r) = (1+\varepsilon^2 r^2)^\beta$, $\beta > 0$ $(m = \lceil\beta\rceil$, where $\lceil\beta\rceil$ means the smallest integer larger than $\beta)$
- MN : $\phi(r) = r^{2k-1}$, $k \in N$ $(m = k)$

These radial functions, which could not be considered using the direct method (1.2), now can be used to find a unique RBF interpolant via (1.8). We note that all the radial functions which give a unique solution to (1.2) can also be used via (1.8). In fact, in the case where the functions are completely monotonic, we will recover (1.2) from (1.8) since in that case, $m = 0$. By using the representation (1.8) rather than (1.2), although we have relaxed the conditions on the radial functions, thus opening the door to a much larger class of radial functions, we have added new restrictions on the data node sets. For this reason and because the most common radial functions don't require the augmented form (MQ, GA, IMQ, IQ, etc.), we make use principally, in the work presented here, of the representation (1.2), rather than the augmented RBF method (1.8).

1.7 Overview of thesis topics

This dissertation is divided into six Chapters. Chapter 2 contains a summary of our work on studying the decay rates of the RBFs expansion coefficients when interpolating cardinal data. In short, we study the locality property of the RBF method, with respect to its expansion coefficients space. A completely different topic is studied in the subsequent chapters, the RBF-QR method. In Chapter 3, we introduce the RBF-QR method and apply it to interpolation. Chapters 4 and 5 focus on applying RBF schemes to solve purely convective PDEs on the surface of the sphere. Both the RBF-QR with fixed and with variable shape parameters are introduced and utilized in these contexts. Finally, Chapter 6 offers conclusions.

Chapter 2

Localisation properties of RBF expansion coefficients for cardinal interpolation

2.1 Motivation

Despite the great qualities of the RBF method, such as its spectral accuracy or the fact that it is meshfree, its high computational cost is the main reason for which it is not being used more widely. Most radial functions are global which implies that the interpolation matrix to which they give rise, is dense. The bulk of the method's high cost comes from the process of inverting this matrix. Several research groups (Faul, Powell, Beatson, Greengard, etc.) have been working on finding algorithms to decrease this complexity. However, in the hope of better understanding the RBF method and perhaps of advancing research towards an efficient fast algorithm, we instead focus on analyzing the RBF interpolants' intrinsic locality property of their expansion coefficients. Indeed, RBFs have this property which none of the most popular pseudospectral methods exhibit, that a perturbation in a function value will only affect the expansion coefficients associated with the nodes neighboring that perturbation location. This chapter is intended to study this property and to give insights on why and how it can be used to reduce the complexity of the RBF method. Bengt Fornberg, Natasha Flyer, Tyger Hovde and the author all contributed to this project.

2.2 Definition of 'locality' in this context

The property of locality which RBF's expansion coefficients possess is illustrated in Figure 2.1. In this figure, we show the impact of the perturbation of one function value on both the RBF and the Fourier expansion coefficients. The plot of the difference between the original and the perturbed cases demonstrates that, in the RBFs case, the impact decreases exponentially fast as we move away from the perturbed node. However, in the Fourier case, all of the expansion coefficients have been affected, which shows the lack of the locality in the Fourier coefficients. For simplicity, our study focuses on infinite integer lattice. We based it on Fourier analysis, the perfect tool for such a setting. The more general case of semi-infinite integer lattice case and the scattered data case were recently considered by Tyger Hovde, but no paper on this subject is yet available.

2.3 Consequences of such a property

In a counter-intuitive way, although most radial functions are global, and some, such as MQ even growing larger with increasing distances, they all still are found to possess an innate locality character with respect to their expansion coefficients. This property, which had not been pointed out clearly in earlier literature, or been analyzed, is advantageous to us in a few respects.

2.3.1 The conditioning of the interpolation matrix

The property of locality is tied in with the unconditional non-singularity of the interpolation matrix to which the radial function gives rise. A perfect locality would imply a diagonal interpolation matrix, thus a perfectly conditioned system which is trivial and quick to invert. Any amount of locality will likely make our system better conditioned. A consequence of this will be that iterative methods [7], [11] to find the interpolant will therefore converge faster and this is one possible way out of the $O(n^3)$

complexity.

2.3.2 Fast algorithms

Locality gives us an opportunity for fast algorithms. As we mentioned above, it enters in the convergence rates of some of the existing algorithms. But the importance of the locality property when it comes to fast algorithms is explained very schematically in Figure 2.2

- Consider interpolating n data points in 1-D. In order to compute the interpolant (i.e. in order to find the expansion coefficients of the interpolant,) we will need $O(n^3)$ operations since inverting a dense matrix is necessary. The first row of Figure 2.2 illustrates this situation.

- Now, consider splitting the n nodes into clusters of neighboring points, as on the second, third and fourth rows of Figure 2.2 . When we interpolate these clusters, the property of locality implies that the expansion coefficients associated with the interior nodes of the cluster will be resolved up to some accuracy (which depends on how much in the "interior" the nodes are).

- Assuming that we split n points into m clusters. The work for each cluster will be $O(n/m)^3$ operations. We perform this about $2 * m$ times (the factor of 2 comes from the overlapping nodes). Thus the total process will cost $O(n^3/m^2)$. Take $m \approx \sqrt(n)$ and we get an $O(n^2)$ method.

2.3.3 Benefits due to the locality property on scattered nodes

Although it is not documented in a paper yet, Tyger Hovde's work suggests that the locality property is not confined to interpolation on integer lattice, but arrises also for scattered data. The benefits of the locality property which we described above will therefore also be useful on non-regular lattice. Another one of the consequences will be

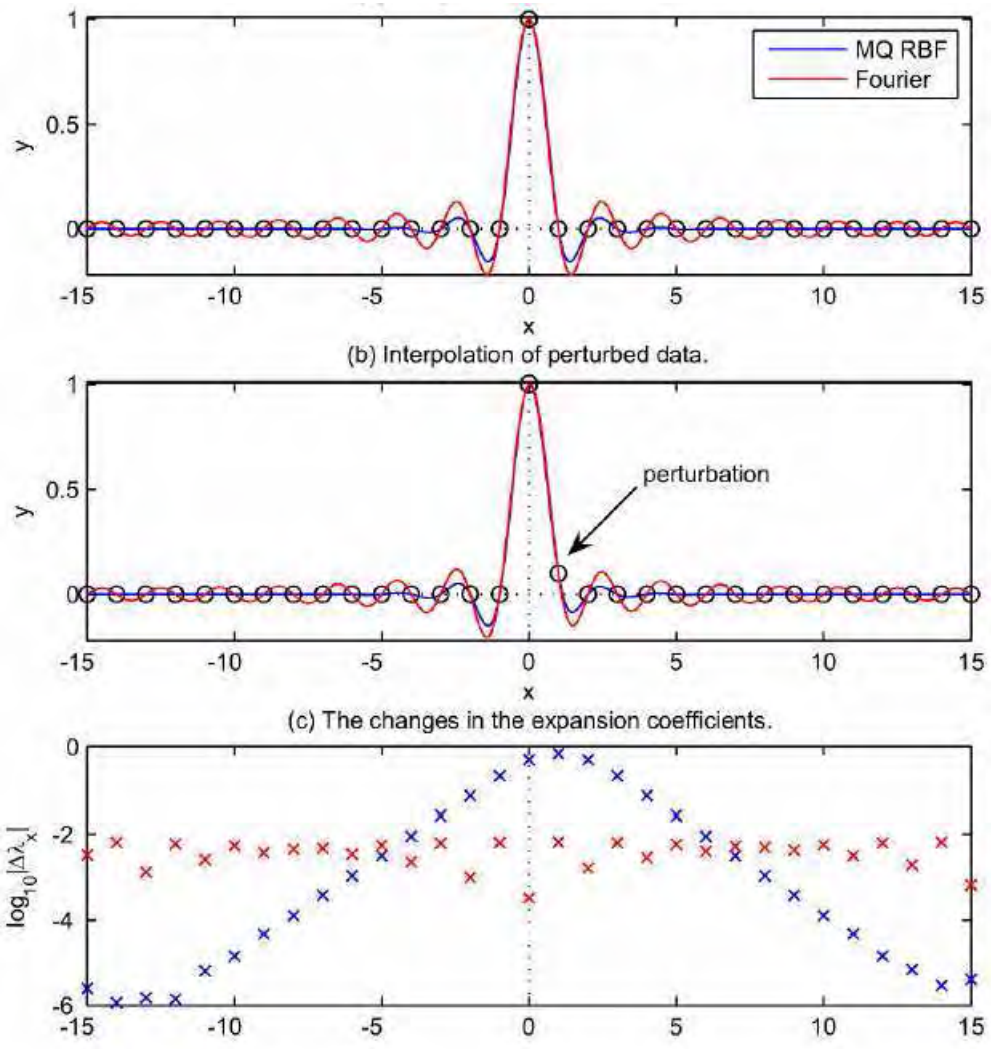

Figure 2.1: Plots demonstrating the locality property of the RBF expansion coefficients (Figure produced by TH)

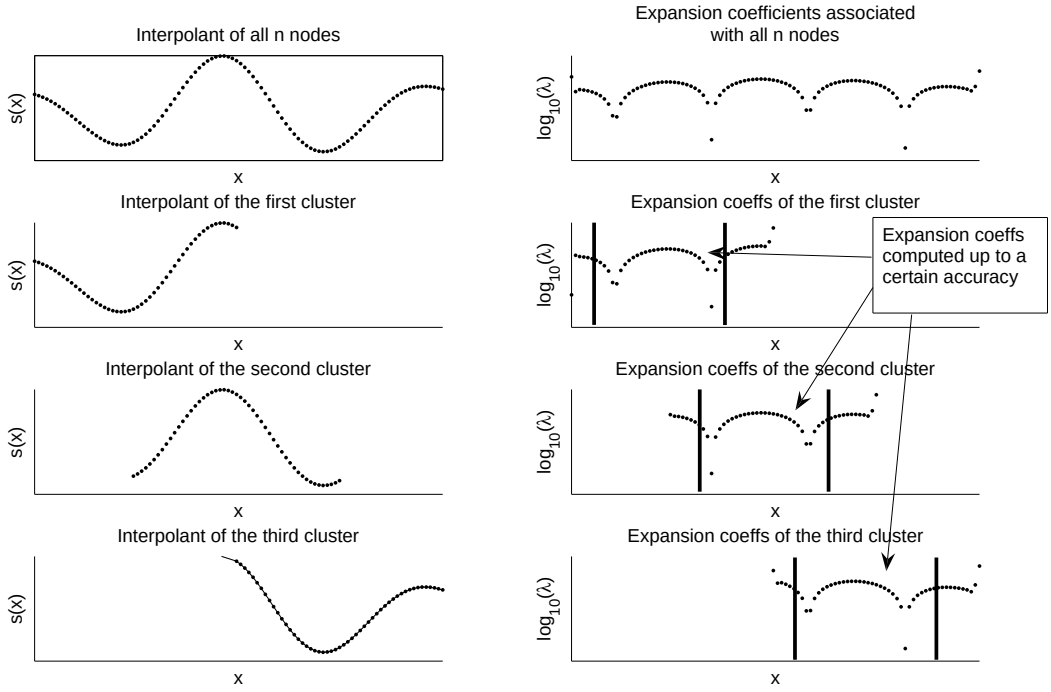

Figure 2.2: Illustration of a fast algorithm scheme which makes use of the RBF expansion coefficients locality property.

the easy addition of node points to an interpolant, since it will not necessitate solving the system all over again, but rather, solving a system that only includes the neighboring nodes to the point which we are adding.

Our work on analyzing the locality property of the RBF expansion coefficients [16] can be found as Appendix A and is about to appear in the IMA Journal on Numerical Analysis.

2.4 Summary of paper

2.4.1 Introduction

In this section, we motivate the project. Although the RBF method is a generalization of all classical pseudospectral methods (to scattered nodes and irregular domains, Driscoll & Fornberg, 2002), there are important differences between the two types of methods; if the classical PS basis sets have an inherent orthogonality property, RBFs on the other hand, provide an unconditional non-singularity of the collocation matrix, even in scattered node multi-dimensional cases. The RBF interpolants exhibit a strong property of locality, which PS methods lack. The concept of locality is then introduced and defined. We explain how the lack of locality can be responsible for ill-conditioning and how the degree of locality enters in the convergence rates of fast iterative methods. We give a brief sketch on how we will quantify the degree of locality for each of the most commonly used radial functions in one and in two-dimensions by analysing the expansion coefficients obtained when interpolating cardinal data (i.e. 1 at the datum, and 0 at each other integer lattice node). We then outline the different sections.

Our work on analyzing locality builds on Buhmann's references [5], [6] where he found integral formulas for the expansion coefficients to the cardinal data interpolant, which we show next. While adopting the definition for the Fourier transforms $f(x) = \frac{1}{\sqrt{2\pi}} \int_{-\infty}^{\infty} \widehat{f}(\omega) e^{i\omega x} d\omega$ and $\widehat{f}(\omega) = \frac{1}{\sqrt{2\pi}} \int_{-\infty}^{\infty} f(x) e^{-i\omega x} dx$, the expansion coefficients can

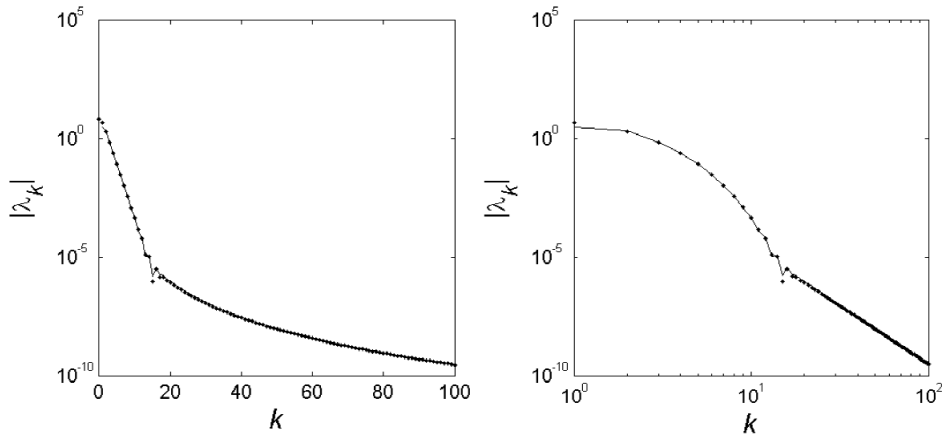

Figure 2.3: Plots of λ in function of k in the case of MQ for $\varepsilon = 1$. Notice the exponential decay for small k, followed by the algebraic decay. The dots show the true λ, while the solid line shows the results of our 2-term asymptotic formula.

be written as

$$\lambda_k = \frac{1}{(2\pi)^{3/2}} \int_0^{2\pi} \frac{e^{ik\xi}}{\sum_{j=-\infty}^{\infty} \widehat{\phi}(|\xi + 2\pi j|)} d\xi \tag{2.1}$$

Buhmann studied the decay rates of their interpolant $s(\underline{x})$ as $||x|| \to \infty$. In [16], we analyze instead the decay rates of the expansion coefficients of the interpolant to cardinal data, by finding closed form expressions or asymptotic expansions to (2.1) for all of the commonly used radial functions. In 1-D, we find that for small k, the expansion coefficients λ_k decay exponentially for all radial functions. For larger k, the coefficients λ_k either revert to an algebraic deay (e.g., TPS, IQ, MQ) or don't (e.g., GA, CU). In 2-D, we find the same kind of decay as in the 1-D case (example in Figure 2.3) characterized by an exponential decay followed possibly by an algebraic decay. We also find a dependence of the decay on the angle in the coefficient space k_1, k_2. In the 1-D case and in the 2-D case, we examine the effect of the shape parameter on the decay rates.

2.4.2 Closed form expressions for cardinal coefficients

In this section, we derive general integral formulas for the expansion coefficients when interpolating cardinal data in d-dimensions. We base our work on Martin Buhmann's formula (A.2.3), generalize it to d-dimensions and devise a plan to obtain explicit expressions for all radial functions. For some radial functions, it is possible to obtain fairly simple expressions for the cardinal data expansion coefficients in 1D. These special cases, which include CU, IQ, GA and SH are thouroughly worked out. Most of the analytic work of this section was done by NF and by BF.

2.4.3 Asymptotic analysis in 1-D by means of contour integration

As we mentioned earlier, it is rare to be able to find a closed form explicit formula (i.e. not an integral formula) for cardinal expansion coeffients. This section describes an original asymptotic approach to approximate these coefficients and their decay rates.

2.4.3.1 Methodology

The integral equation (A.2.3) for the expansion coefficients is a Fourier type integral

$$I(x) = \int_C f(z) e^{x(u(z)+v(z))} dz \tag{2.2}$$

where $u(z) = 0$ and where $v(z) = iz$ The method of the steepest descent constists in modifying the contour in order to integrate along the steepest descent of the exponentiated function $u(z)$. It follows from calculus that the path which will make $u(z)$ descent the fastest is also the path which will make $v(z)$ constant [1]. Instead of following the real axis from 0 to 2π, we follow $z = it$, which makes $u(z) = -t$ and $v(z) = 0$ and which conveniently makes our integral a Laplace's type integral with a fast decaying integrand, on which we use Laplace's method. In order to make the bridge from 0 to 2π (Figure A.2), we follow the path $z = ic + t$, where c is a large positive real number.

The integral takes the form $I(x) = \int_C f(z)e^{x(-c+it)}dz$, which is insignificant for large enough c by Jordan's lemma. It remains to calculate the residues at the poles that this new contour surrounds to get an asymptotic formula for the decay rates of the different radial functions. We notice that the vertical path, along the imaginary axis, goes along a branch cut for some radial functions. So, even though the integrand is 2π periodic, going up and down the path on each side of the cut will result in an algebraic contribution, while the pole will contribute with an exponential. The radial functions which do not have a branch cut on the imaginary axis will thus have expansion coefficients whose behavior is lead by only exponentials and won't have the second agebraic regime, observed in some cases. These two main contributions correspond to two different types of decay, dominating for different regimes of the index of the expansion coefficients. The contribution from the pole is an exponential part, producing an exponential decay as the index grows. The branch cuts give rise to an algebraic part, thus, an algebraic decay. We applied this method to the MQ (CP and TH), IQ (CP), GMQ (CP and TH), GA (BF), SH (BF) and BSL (BF) and found in each case asymptotic formulas for the decay of the expansion coefficients in terms of the index and of the shape parameter ε. In the case of the generalized multiquadric radial function GMQ, we explain why the MQ is 'optimal' also from the point of view of locality. Indeed, we find that when β is a half-integer, the algebraic decay is more abrupt than otherwise (Figure A.5). However, as β increases, the conditioning worsens making $\beta = 1/2$ especially attractive.

2.4.4 Summary of asymptotic observations in 1-D

This analysis allows us to find generalizations for the behavior of the expansion coeffients of the different radial functions.

- All radial functions see an exponential decay in their cardinal coefficients. This mostly influences the first few terms since the exponential decay is so abrupt.

- Some radial functions experience an algebraic decay. This type of decay dominates the character of the expansion coefficients later in the indices. There will be such a decay if the integrand in Equation (A.2.3) contains a branch cut.

- As the shape parameter ε goes to 0, the coefficients of the leading terms increase considerably, as shown in Table A.1, making the decay slower.

2.4.5 Analysis and observations in 2-D and higher

The natural follow up to this work is to consider the two-dimensional case and to figure out whether or not the localization trend is still present. We found numerically that in the two-dimensions case, this trend is still there for all of the radial functions which we considered. However, the lack of an analog to Cauchy's formula in higher dimensions made it impossible for us to carry out our asymptotics method in two dimensions. The exponential decay rate depends on the radial direction in the k_1, k_2-plane as seen in Figure A.8. In fact, it is important to note that this angular dependence comes from the node layout. The one presented here is a cartesian node layout and gives us a particular four-fold symmetry, while a hexagonal layout will give us a six-fold symmetry (this is being explored further by TH and by BF). With this considerable added difficulty, we were not able to find an expression for the exponential decay rates.

- GA: In the Gaussian case, we find a closed-form expression for the cardinal expansion coefficients in d-dimensions. In fact, the value of the cardinal expansion coefficients in d-dimensions can be written as the product of the 1-D coefficients along each dimension. This was proved by the author (CP).

- CU: We were only able to express the asymptotic algebraic rate for the cubic RBFs using an original method presented in Section A.5.2.1. This work was done by BF.

- TPS, GA and SH: There is no algebraic trend to the decay, since for all of these radial functions, the integrand does not contain any branch cut. We note that we also include a proof of the unconditional non-singularity of the collocation matrix associated with SH, for scattered data and in d-dimensions (BF and NF).

- MQ, IMQ, IQ: Using the same technique as for the cubic RBFs, we found the algebraic decay rates for these radial functions (BF).

2.4.6 Summary of observations for RBF cardinal coefficient decay

In this section, we summarize the important observations and conclusions that were made in this paper. We point out the significance of the exponential decay as the leading order behaviour.

2.5 Additional results

2.5.1 Introduction

Different efforts were put towards broadening this work. TH studied the decay rates of cardinal data expansion coefficients on the semi-infinite line and on scattered data on the 1-D infinite line. The author (CP) studied further the decay of equispaced cardinal data expansion coefficients on the unit circle, and how it varied from the 1-D infinite lattice case. This is presented next.

2.5.2 Equispaced cardinal data expansion coefficients on the unit circle

Let the radius r be fixed and let $\theta_i = \frac{2\pi}{n} i$, $i = 0, ..., n-1$.

The interpolant takes the form

$$s(\underline{x}) = \sum_{i=0}^{n-1} \lambda_i \phi(||\underline{x}_i - \underline{x}||) \tag{2.3}$$

Making the change of coordinates to polar, with $\underline{x} = (r\cos(\theta), r\sin(\theta)), \underline{x}_i = (r\cos(\theta_i), r\sin(\theta_i))$, and making use of some trigonometric identities, we get

$$s(\theta) = \sum_{i=0}^{n-1} \lambda_i \phi\left(2r\sin\left(\frac{\theta}{2} - \frac{\pi i}{n}\right)\right) \tag{2.4}$$

In order to interpolate the cardinal function, $f\left(\frac{2\pi k}{n}\right) = 1$ for $k = 0$, and $f\left(\frac{2\pi k}{n}\right) = 0$ for $k = 1, ..., n-1$ we require that

$$s\left(\frac{2\pi k}{n}\right) = \sum_{i=0}^{n-1} \lambda_i \phi\left(2r\sin\left(\frac{\pi k}{n} - \frac{\pi i}{n}\right)\right) \tag{2.5}$$

Let

$$\beta(\rho) = \phi\left(2r\sin\left(\frac{\pi}{N}(\rho)\right)\right) \tag{2.6}$$

Also, let

$$\Lambda(\xi) = \sum_{k=0}^{n-1} \lambda_k e^{ik\xi} \tag{2.7}$$

and

$$\Theta(\xi) = \sum_{k=0}^{n-1} \beta(k) e^{ik\xi} \tag{2.8}$$

Using the convolution theorem for discrete Fourier Transforms, we know that

$$\Theta(\xi)\Lambda(\xi) = 1 \tag{2.9}$$

Therefore,

$$\Lambda(\xi) = \frac{1}{\Theta(\xi)} \tag{2.10}$$

which gives us finally the analog to Equation (A.2.3) (given for the 1-D infinite line), the closed form expression of the cardinal expansion coefficients on the circle,

$$\lambda_k = \frac{1}{n} \sum_{j=0}^{n-1} \left(\frac{e^{-ik2\pi j/n}}{\sum_{m=0}^{n-1} \phi(2r\sin(\pi m/n)) e^{im2\pi j/n}} \right) \tag{2.11}$$

In order to make a comparison with the case of the 1-D infinite lattice and the analysis of its cardinal expansion coefficients decay rates, we consider Equation (A.2.3)

$$\lambda_k = \frac{1}{2\pi} \int_{-\pi}^{\pi} \frac{e^{-ik\xi}}{\sum_{j=-\infty}^{\infty} \phi(j) e^{ij\xi}} d\xi \tag{2.12}$$

We apply the composite trapezoidal rule on this integral (with a periodic integrand, thus giving us spectral precision), and we get

$$\lambda_k = \frac{1}{n}\sum_{j=0}^{n-1}\left(\frac{e^{-ik2\pi j/n}}{\sum_{m=-\infty}^{\infty}\phi(m)e^{im2\pi j/n}}\right) + O(e^{-\alpha n}) \tag{2.13}$$

Notice that (2.11) and (2.13) are identical except from their denominators. In order to be able to compare both equations more easily, we note that

$$\sum_{m=-\infty}^{\infty}\phi(m)e^{im2\pi j/n} = \sum_{m=0}^{n-1}e^{im2\pi j/N}\sum_{k=-\infty}^{\infty}\phi(m+kn) \tag{2.14}$$

Also we notice that, although $\sum_{k=-\infty}^{\infty}\phi(m+kN)$ obviously diverges for non-decaying RBFs, $\sum_{m=-\infty}^{\infty}\phi(m)e^{im2\pi j/n}$ converges. Indeed, from the Poisson summation formula,

$$\sum_{m=-\infty}^{\infty}\phi(m)e^{im2\pi j/n} = \sum_{k=-\infty}^{\infty}\hat{\phi}(2\pi j/n + 2\pi k) \tag{2.15}$$

which converges fast. Now, we have

$$\lambda_k = \frac{1}{n}\sum_{j=0}^{n-1}\left(\frac{e^{-ik2\pi j/N}}{\sum_{m=0}^{n-1}e^{im2\pi j/n}\sum_{k=-\infty}^{\infty}\phi(m+kn)}\right) + O(e^{-\alpha n}) \tag{2.16}$$

Thus for a fixed n large enough,

$$\sum_{m=0}^{n-1}e^{im2\pi j/n}\sum_{k=-\infty}^{\infty}\phi(m+kn) \approx \sum_{m=0}^{n-1}e^{im2\pi j/n}\sum_{k=-M}^{M}\phi(m+kn) \tag{2.17}$$

$$\approx \sum_{m=0}^{n-1}e^{im2\pi j/n}\phi(m) \tag{2.18}$$

So, for n large enough, we can approximate Equation (2.16) with

$$\lambda_k \approx \frac{1}{n}\sum_{j=0}^{n-1}\left(\frac{e^{-ik2\pi j/N}}{\sum_{m=0}^{n-1}e^{im2\pi j/n}\phi(m)}\right) \tag{2.19}$$

Equations (2.11) and (2.19) are very similar. Indeed, the only difference between those two are $\phi(2r\sin(\pi m/n))$ in Equation (2.11) versus $\phi(m)$ in Equation (2.19). In fact, to see how similar these two equations are, we look at the Taylor series expansion of $\phi(2r\sin(\pi m/n))$

$$2r\sin(\frac{\pi m}{n}) = 2r(\frac{\pi m}{n} - \frac{\pi^3 m^3}{3!n^3} + \frac{\pi^5 m^5}{5!n^5} - ...) \tag{2.20}$$

It is now obvious that for n very large,

$$2r\sin(\frac{\pi m}{n}) \approx 2r\frac{\pi m}{n} \tag{2.21}$$

Thus choosing $r = \frac{n}{2\pi}$ will lead to

$$2r\sin(\frac{\pi m}{n}) \approx m \tag{2.22}$$

which makes Equations (2.11) and (2.19) identical for very large n (The infinite line case presented in Appendix A is thus the limiting case of the circle one as the radius $r \to \infty$). This result is interesting in that it gives a link between the cases of the circle and of the 1-D infinite line, where our asymptotic formulas for the decay rates of the cardinal coefficients hold.

Chapter 3

The RBF-QR method

3.1 Introduction

The uncertainty principle was introduced by Robert Schaback in 1995 [39]. It states that it is impossible to simultaneously have a well conditioned system and good accuracy when using the RBF method. In general, decreasing the shape parameter ε has the effect of improving the accuracy of the interpolation [15], but also of raising dramatically the condition number of the collocation matrix. With their Contour-Padé method, Fornberg and Wright [20] disproved this theory and for the first time were able to stably compute interpolants in the region of very small ε for up to around a hundred node points in 1-D (a couple hundred points in 2-D and 3-D). The RBF-QR method, developed for the surface of the sphere by Fornberg and Piret [18], and for more general domains by Larsson and Fornberg [31], is intended to fulfill the same purpose, but for a much larger amount of node points. In addition, the RBF-QR method is faster (same complexity as the original RBF method) and is easier to implement than the Contour-Padé method. We can now compute an RBF interpolant, even when its shape parameter is much too small for the direct method to work, for thousands of node points.

In their recent works [12] and [13], Flyer and Wright compare common spectral methods (Spherical harmonics, double Fourier series and spectral element methods) for solving the pure convection PDE and the shallow water equations on the surface of the sphere, and show the superiority of RBFs in doing so. The strength of RBFs lies in

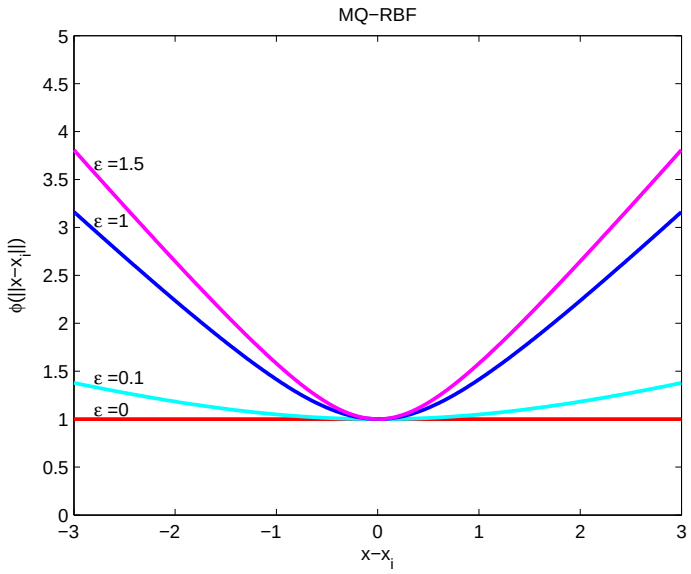

Figure 3.1: The "shape parameter" ε determines the flatness of the radial function.

the fact that it not only works with fewer nodes and longer time-steps than the other spectral methods to obtain the same level of accuracy, but also that it is much simpler to program. However, RBFs still are confronted with the stability and complexity issues mentioned earlier. The RBF-QR method is intended to solve the former. This chapter will focus on the method in itself and the application of interpolation only. Chapter 4 will however be dedicated to using the RBF-QR method to generalize Natasha Flyer and Grady Wright's results on their convection problem.

An article with the introduction of this new algorithm as well as the analysis of numerical results that it yields has appeared in the SIAM Journal of Scientific Computing [18].

3.2 Summary of paper

3.2.1 Introduction

In this section, we give the motivation behind the new RBF-QR method, as a way to go past the ill-conditioning issues that we encounter when we work with flat or

near-flat radial functions. Just like the Contour-Padé method, the RBF-QR method allows us to compute stably the interpolant (and the solution to PDEs in Chapter 4) even with flat radial functions. It has the advantages over the Contour-Padé method that is much easier to code and that it can handle thousands of node points and remain a stable algorithm.

The terms of the basis behind the direct RBF method are the RBF translates centered at each node location. They become awfully linearly dependent with each other when they become flat. But their interpolation space improves (explained in Chapter 1). The key behind the RBF-QR algorithm is the formation of an equivalent, in terms of the spaced spanned, but much better conditioned basis than the one associated with the direct method (RBF-Direct).

3.2.2 RBF methodology

In this section, we expose some of the basic RBF theory, also found in the first chapter of this dissertation.

3.2.3 The RBF-QR method

3.2.3.1 An equivalent basis

The key of this method is the basis transformation from a very ill conditioned one (made of the translates of the radial function) to a much better conditioned one, which spans the same exact space. Making such a basis change is exactly what we do when we go from the ill conditioned monomials $1, x, x^2, ..., x^n$ on [-1,1] to the much better conditioned Chebyshev basis $T_0(x), T_1(x), T_2(x), ..., T_n(x)$.

3.2.3.2 Sherical Harmonics (SPH)

Spherical harmonics can be considered as analogs of the Fourier modes on the surface of the sphere. Just like Fourier modes, spherical harmonics can be seen as a

set of orthogonal eigenfunctions to Laplace's equation, hence the origin of their name 'harmonic' [35]. Just like Fourier modes on the unit circle, we can see them as harmonic polynomials restricted to the surface of the sphere. They do not have a naturally associated node set but Euler points (latitude/longitude grid) are sometimes used - if so, with several times more nodes than there are SPH coefficients. However, there exists no clear fast algorithm like the FFT (although some approaches offer advantages in very large cases; see [40] and [36]) which would allow us to easily go from one native space to the next. Just like Fourier modes, Spherical harmonics offer no possible local refinement. We can't increase the accuracy in one specific area of the domain by clustering nodes in that specific area. Although SPH offer a spectral accuracy when it comes to solving PDEs on the surface of the sphere, their accuracy is uniform across the surface of the sphere.

3.2.3.3 Expansions

We base our method on the formulas explicitly given by Hubbert and Baxter [26] for MQ, IMQ and GA.

$$\phi(\|\underline{x} - \underline{x}_i\|) = \sum_{\mu=0}^{\infty} \sum_{\nu=-\mu}^{\mu} {}' \{c_{\mu,\varepsilon}\, \varepsilon^{2\mu}\, Y_\mu{}^\nu(\underline{x}_i)\}\, Y_\mu{}^\nu(\underline{x}) \,, \tag{3.1}$$

where the weights $c_{\mu,\varepsilon}$ can be found in table (B.3.2)

3.2.3.4 Matrix representation

In this section, we describe the matrix aglebra behind the RBF-QR method. First, the equivalent repesentation to the radial function translates in terms of SPH is displayed in (B.3.4) and in matrix $\times$ vector form in (B.3.5). A QR factorization is then applied to matrix B, and the ill-conditioning in the form of matrix E (B.3.6) is removed analytically (without leaving any trace of the original ill-conditioning). Another way to explain the method is by the following argument. Consider the direct RBF method

interpolation representation $A \cdot \lambda = f$. From equation (B.3.6), $A = Y^T \cdot R^T \cdot E \cdot Q^{-1}$. Thus, $Y^T \cdot R^T \cdot E \cdot Q^{-1} \cdot \lambda = f$. We observed that when the radial functions become flat (when $\varepsilon \to 0$), the expansion coefficients λ tend to $\pm\infty$. With this representation, we have isolated all the ill-conditioning in the matrix E (diagonal matrix whose terms are powers of ε) which then can be eliminated from the problem by letting $\sigma = E \cdot Q^{-1}\lambda$. We obtain the RBF-QR representation of the RBF interpolant $Y^T \cdot R^T \cdot \sigma = f$, where each term is well-behaved with respect to ε. The original idea of changing basis to analytically remove the singularity caused by powers of ε comes from (BF), and its evolution to the RBF-QR method was a collaborative work between (BF) and (CP). Thanks to this change of basis from the radial function's translates to ultimately a basis of the form (B.3.7), we prove that in the limit of $\varepsilon \to 0$, the RBF interpolant converges towards a unique spherical harmonics interpolant on the conditions that the number of nodes n is a square number and that the spherical harmonics interpolant exists. This result is the analog on the sphere to the one proved by Driscoll and Fornberg [8], which states that in 1-D, the RBF interpolant converges towards the Lagrange interpolating polynomial. This was proved by the author (CP) along with (BF).

3.2.3.5 Computational considerations

In this section, we discuss the complexity and we describe the approach that we took with respect to truncation.

- Code complexity. The computational cost is of $O(n^3)$. It originates from the cost of a QR factorization of the B matrix and the cost of a matrix inversion (which corresponds to finding the expansion coefficients of the interpolant with respect of the new basis), both of which are $O(n^3)$. It thus has the same order of computational cost as the direct method.

- Truncation. We need to guarantee an accuracy to machine precision (i.e. 16

digits of accuracy) of the SPH expansion of the radial function translates (according to Equation (B.3.3)). Each row of matrix B contains the SPH expansion coefficients of a radial function (Equation (B.3.5)). Thus we build matrix B by adding blocks which correspond to consecutive degrees of spherical harmonics. We stop adding blocks when the magnitude of the last entered block is 10^-16 smaller than the magnitude of the block containing the n^{th} SPH expansion coefficient.

3.2.4 Numerical results

We tested our method on the following two functions

$$\begin{aligned} \textbf{Gaussian bell:} \quad & g(x,y,z) = e^{-(\frac{2.25}{R}\arccos x)^2}, \\ \textbf{Cosine bell:} \quad & c(x,y,z) = \begin{cases} \frac{1}{2}(1+\cos(\frac{\pi}{R}\arccos x)) & x > \cos R, \\ 0 & x \le \cos R, \end{cases} \end{aligned} \tag{3.2}$$

of smoothness C_∞ and C_1, respectively. R is here a parameter which controls how peaked the bells are, going from spike-like at $R = 0$ to flat for increasing R. The cosine bell features a jump in the second derivative at the edge of its region of support. Figure 3.2 shows the error when we interpolate, at 1849 nodes, Gaussian bells of two different thicknesses and under two different node distributions (random distribution and minimum energy node distribution). We see that the error computed using the RBF-QR method smoothly continues the curve of the error obtained from the direct method when ill-conditioning kicks in at about $\varepsilon \approx 1$.

We observe that there is in all cases an ε, call it ε_{opt}, which yields the smallest error. As mentioned earlier, Fornberg and Zuev [22] ascribe the increase in the error when $\varepsilon < \varepsilon_{opt}$ to the Runge phenomenon. On the surface of the sphere, a similar phenomenon arises. As we mentioned earlier, as $\varepsilon \to 0$, the RBF interpolant tends to the spherical harmonics (SPH) interpolant of a certain degree depending on the number of node points. The SPH of a fixed degree can only resolve accurately peaks of a certain

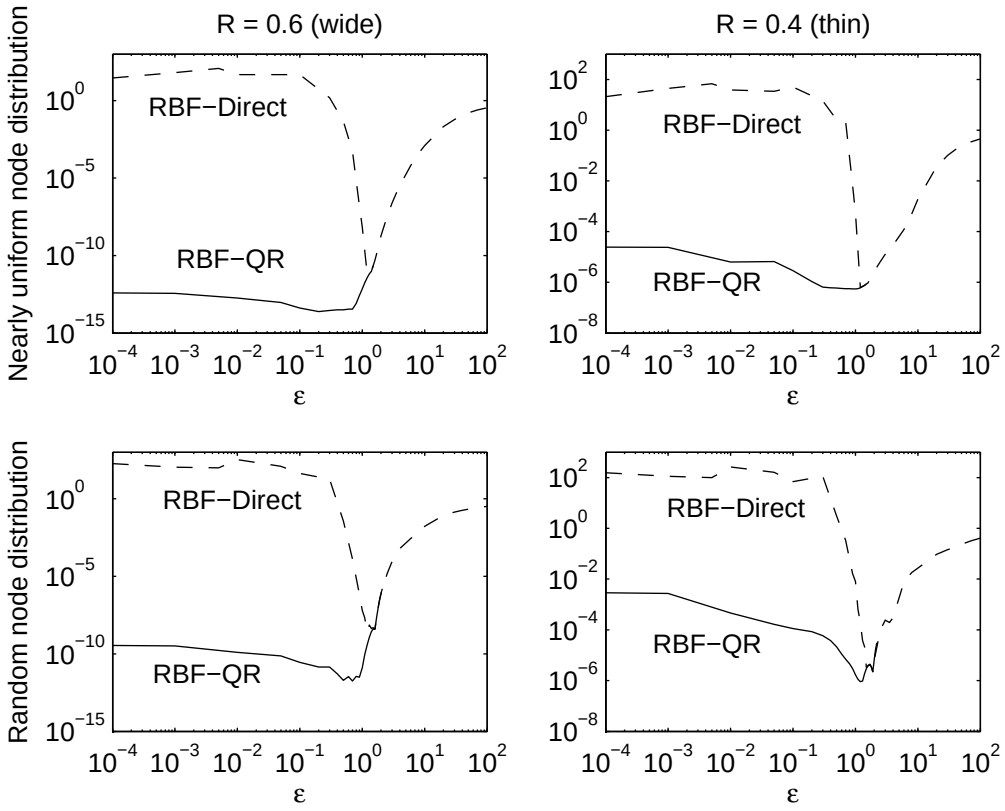

Figure 3.2: Interpolation error of a Gaussian bell in function of the shape parameter.

width. Therefore, thinner peaks cannot be resolved without introducing error at the base of the structure. This explains the increase in the error when ε tends to 0.

3.2.5 Some comments on the choice of optimal ε

In this section, we discuss the value of the 'optimal' shape parameter value. For years, people observed a decrease in the error as ε was getting smaller. On the other hand, as ε was getting smaller, the ill-conditioning of the collocation matrix was getting larger. There was a point finally where the ill-conditioning was too large to give an accurate result, and the error would start increasing as ε was getting smaller. People considered the ε value corresponding to the minimum error, the 'optimal' shape parameter value. Thanks to the RBF-QR method, we realize that this value is not actually the 'optimal' one, but the value at which the detrimental ill-conditioning of the collocation matrix starts to cause harm. We can now remove this detrimental ill-conditioning and observe that another phenomenon, the Runge phenomenon, generates an error as well, when ε gets smaller. The 'optimal' shape parameter is therefore the value of ε at which the Runge phenomenon appears.

3.2.6 Conclusion

This section contains the main conclusions. We reiterate the purpose and utility of the RBF-QR method. We also explain in which respects the RBF method is superior to the SPH method. Finally, we include a thouroughly documented *Matlab* code for the RBF-QR method.

3.3 Additional work

This additional analysis work was not included in [18]. It gives an explanation for the increase in the error as ε gets very small.

3.3.1 Interpretation of test results: Error levels when ε is very small

For non-periodic problems, it was noted in [22] that the polynomial Runge phenomenon often will explain the observed error growth as ε approaches zero. In the present periodic setting, we will next see that a similar effect will again arise, but which is this time best understood by considering properties of an SPH expansion.

Recalling the polynomial representation for the SPH basis functions, as displayed in Table B.3.1, it is clear that the function $f(x,y,z) = (\frac{1+x}{2})^{42}$ (like any other polynomial in x, y, z of degree up to 42) when restricted to the sphere $x^2 + y^2 + z^2 = 1$ will become exactly represented as an SPH interpolant over $n = 1849 = 43^2$ nodes when we are using SPH functions up to $\mu \leq 42$. This function $f(x,y,z)$ is displayed at the top of Figures 3.3 and 3.4. We can note that the width of this 'bell' falls somewhere in-between the Gaussian bells with $R = 0.6$ and $R = 0.4$, as were used to obtain the data for Figure B.4.4. In some sense, the $f(x,y,z)$ bell represents the narrowest one for which RBF interpolation is nearly perfect in the SPH $\varepsilon \to 0$ limit.

To understand how the SPH interpolation error will grow when bells are made even narrower than the one represented by $f(x,y,z)$, we can first note that Chebyshev polynomials oscillate by equal amplitude over $x \in [-1,1]$ but grow extremely fast outside this interval. Based on this observation, we can translate and scale the Chebyshev polynomial in x of degree 42 to become still much more peaked at $x = 1$ than the function $(\frac{1+x}{2})^{42}$. Like how we extended the univariate function $(\frac{1+x}{2})^{42}$ into $f(x,y,z) = (\frac{1+x}{2})^{42}$ (defined over the surface of a sphere), we also extend the translated and scaled Chebyshev polynomials, with the results as seen in the remaining subplots of Figures 3.3 and 3.4. In these cases, a is a free parameter, and

$$f(x,y,z) = \frac{1}{a} T_{42}\left((\frac{x+1}{2})\beta + (\frac{x-1}{2}) \right) \tag{3.3}$$

where β is chosen such that $T_{42}(\beta) = a$. The interval [-1,1] for x has become mapped to $[-1,\beta]$ where to $a = 10^4,\ 10^2,\ 10^1$ correspond $\beta = 1.0279,\ 1.00797,\ 1.00254$ respec-

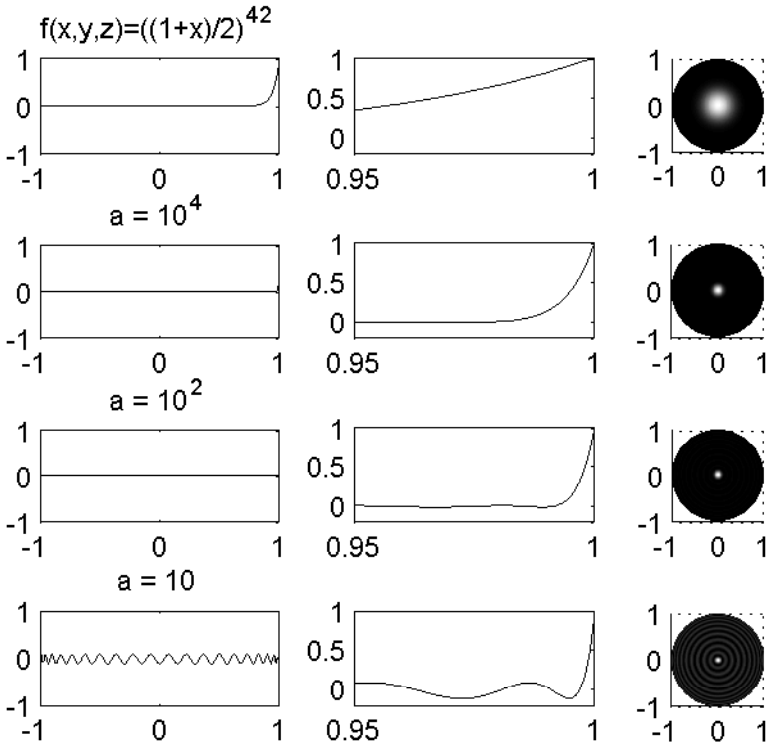

Figure 3.3: The function $f(x, y, z) = (\frac{1+x}{2})^{42}$ and Chebyshev-type bells for different values of their paratemer a, as defined by (3.3). In order to display the ripples better, the grey scale in the right column of subplots is different from the one used in Figures B.4.2 and B.4.3.

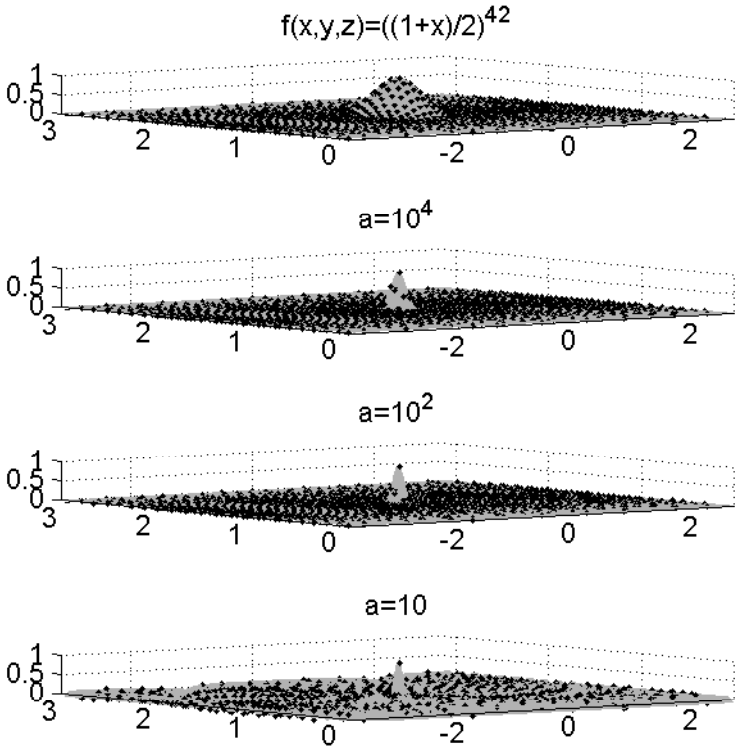

Figure 3.4: The same bell functions as in Figure 3.3, displayed over the φ, θ-plane, with the $n = 1849$ nodes also marked.

tively. These very peaked bells will again be interpolated exactly when using SPH (i.e. RBF with $\varepsilon = 0$) and $n = 1849$ points. However, this has come at the price of significant 'noise' (with amplitude $\frac{1}{a}$) away from the peak. In contrast to this SPH trade-off between sharpness of bells and a noisy base level, RBF with larger values of ε can easily represent very peaked bells without any background level of 'noise'. For GA, IQ and IMQ radial functions, this is immediately obvious, but can also be seen to be the case for MQ.

3.3.2 Fourier expansion coefficients on the circle

We present the analog in terms of Fourier modes on the circle to the expression of the radial function translates in terms of SPH on the sphere (B.3.3). Thanks to these expansions, we can easily modify the RBF-QR method presented in [18] to involve Fourier modes instead of SPH. This work was completed by the author (CP)

Let $\underline{x} = (\cos\theta, \sin\theta)$ and $\underline{x_i} = (\cos\theta_i, \sin\theta_i)$

3.3.2.1 Closed form expression for the Fourier coefficients

In rare cases, we can find a closed form expression for the Fourier expansion coefficients of the radial function translates. Here are two examples, GA and IQ.

$$\begin{aligned}
\phi(||\underline{x} - \underline{x_i}||) &= \phi\left(\sqrt{2 - 2\underline{x}.\underline{x_i}}\right) \\
&= \phi\left(\sqrt{2 - 2\cos(\theta - \theta_i)}\right) \\
&= \sum_{k=0}^{\infty} a_k \cos\left(k(\theta - \theta_i)\right) \\
&= \sum_{k=0}^{\infty} a_k (\cos\left(k\theta_i\right)\cos\left(k\theta\right) + \sin\left(k\theta_i\right)\sin\left(k\theta\right)
\end{aligned}$$

Let $\gamma = \theta - \theta_i$

$$a_k = \frac{1}{\pi}\int_{-\pi}^{\pi} \phi\left(\sqrt{2 - 2\cos\gamma}\right)\cos(k\gamma)d\gamma$$

- GA

$$\begin{aligned} a_k &= \frac{1}{\pi}\int_{-\pi}^{\pi} e^{-\varepsilon^2(2-2\cos\gamma)}\cos(k\gamma)d\gamma \\ &= \frac{2}{\pi}e^{-2\varepsilon^2}\int_{0}^{\pi} e^{2\varepsilon^2\cos\gamma}\cos(k\gamma)d\gamma \\ &= 2e^{-2\varepsilon^2}i^k J_k(-2i\varepsilon^2) \\ &= 2e^{-2\varepsilon^2}I_k(2\varepsilon^2) \end{aligned}$$

- IQ

$$\begin{aligned} a_k &= \frac{1}{\pi}\int_{-\pi}^{\pi} \frac{\cos(k\gamma)}{1+\varepsilon^2(2-2\cos\gamma)}d\gamma \\ &= \frac{2}{\pi}\int_{0}^{\pi} \frac{\cos(k\gamma)}{1+4\varepsilon^2\left(\sin\frac{\gamma}{2}\right)^2}d\gamma \\ &= \frac{2}{\sqrt{1+4\varepsilon^2}}\left(\frac{1+2\varepsilon^2-\sqrt{1+4\varepsilon^2}}{2\varepsilon^2}\right)^k \end{aligned}$$

3.3.2.2 General expression for the Fourier coefficients

Let $t = \underline{x}.\underline{x}_i$ and let $\psi(t) = \phi(\sqrt{2-2t})$. We can find the expansion of $\psi(t)$ in terms of legendre polynomials [26].

$$\psi(t) = \sum_{k=0}^{\infty} c_k L_k(t)$$

where the coefficients c_k are defined as follows

$$\begin{aligned} c_k &= \frac{2k+1}{2}\int_{-1}^{1} L_k(t)\psi(t)dt \\ &= \frac{2k+1}{2^{k+1}k!}\int_{-1}^{1}(1-t^2)^k\psi^{(k)}(t)dt \end{aligned}$$

For example in the IMQ case (Note that convergence analysis of the obtained series are considered in [26]),

$$\begin{aligned} c_k &= \frac{(-1)^k\varepsilon^{2k}\sqrt{\pi}}{\Gamma(1/2-k)}2^{4k+1}\frac{k!}{(2k)!}\frac{1}{\left(1+\sqrt{1+4\varepsilon^2}\right)^{2k+1}} \\ &= \frac{2k+1}{2^{k+1}k!}\int_{-1}^{1}(1-t^2)^k\psi^{(k)}(t)dt \end{aligned}$$

A legendre polynomial can always be expressed as a linear combination of Chebyshev polynomials

$$L_k(t) = \sum_{j=0}^{k} {}' b_{j,k} T_j(t)$$

where

$$b_{j,k} = \left(\frac{(-1)^j + 1}{\pi} \right) \frac{\Gamma\left(\frac{1}{2}(1 - j + k)\right) \Gamma\left(\frac{1}{2}(1 + j + k)\right)}{\Gamma\left(\frac{1}{2}(2 - j + k)\right) \Gamma\left(\frac{1}{2}(2 + j + k)\right)}$$

Thus we obtain

$$\psi(t) = \sum_{k=0}^{\infty} c_k \sum_{j=0}^{k} {}' b_{j,k} T_j(t)$$

Now, the Chebychev polynomial can easily be expressed in terms of Fourier modes

$$\begin{aligned} T_j(t) &= T_j(cos(\theta - \theta_i)) \\ &= \cos(j(\theta - \theta_i)) \\ &= \cos(j\theta)\cos(j\theta_i) + \sin(j\theta)\sin(j\theta_i) \end{aligned}$$

Therefore, the expansion of the radial functions in terms of Fourier modes is as follows

$$\begin{aligned} \phi\left(\sqrt{2 - 2\cos(\theta - \theta_i)}\right) &= \sum_{k=0}^{\infty} c_k \sum_{j=0}^{k} {}' b_{j,k} (\cos(j\theta)\cos(j\theta_i) + \sin(j\theta)\sin(j\theta_i)) \\ &= \sum_{j=0}^{\infty} \left(\sum_{k=j}^{\infty} {}' c_k b_{j,k} \right) (\cos(j\theta)\cos(j\theta_i) + \sin(j\theta)\sin(j\theta_i)) \end{aligned}$$

Chapter 4

The RBF-QR method applied to the solution of convective PDEs on the surface of the sphere

4.1 Introduction

All of the most commonly used pseudospectral methods to solve PDEs have weaknesses in the context of solving a convective model problem on the surface of the sphere. The most common PS methods are spherical harmonics, double Fourier series and spectral methods, and they all suffer major problems. For example, by Haar's theorem (see Chapter 1), certain node distributions will lead to singular systems, with the spherical harmonics method. Furthermore, it resolves modes uniformly, like the Fourier approach on the circle, thus it cannot have any local node refinement. The double Fourier technique does not allow any node refinement either. Because of the unnecessary clustering at the boundaries of each element, the spectral element method requires very small time steps. The RBF method gives rise to unconditionally non-singular collocation matrices, allows local node refinement, works on scattered data, does not introduce any singularity, allows for particularly large time steps and is extremely easy to implement on any geometry. Natasha Flyer and Grady Wright [12] showed that, although the computational cost of the RBF method is a problem (at least for now), less nodes and larger time steps give a comparable accuracy to the other PS methods, making the method advantageous to use. In this research project, we use the RBF-QR method to explore the error of convecting a bell around the surface of the sphere. We study the error on the

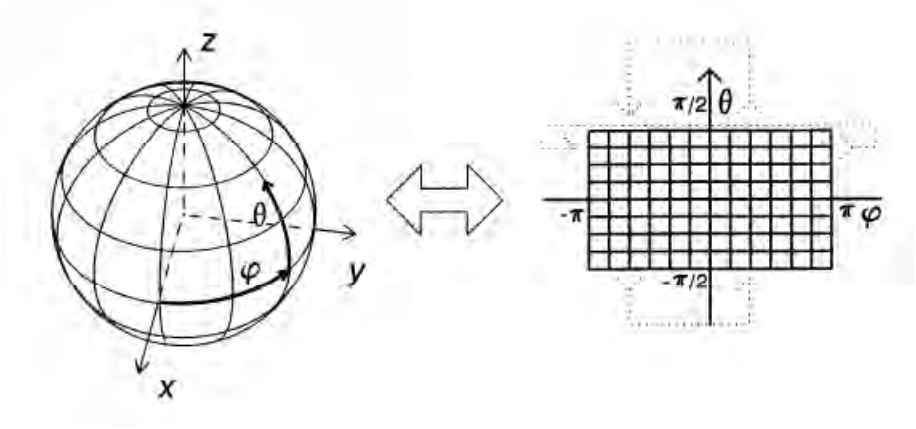

Figure 4.1: Double Fourier series: Necessary map to a lat/long grid.

Figure 4.2: Spectral elements method: implemented by means of the "cubed sphere".

whole range of shape parameter values and for all of the most common radial functions. This analysis gives us insights on which radial function and which shape parameter to use for integration over different lengths of time.

Our work on choosing a radial function and a shape parameter when solving a convective PDE on the sphere can be found as appendix C and has been accepted for publication in the Journal of Computational Physics [19].

4.2 Summary of paper

4.2.1 Introduction

In this section, we present the RBF method as a competitive way to solve the convection equation on the surface of the sphere. We refer to Natasha Flyer and Grady Wright's paper [12] which concludes that RBFs can be very promising when applied to this problem.

However, as we saw in the previous chapter, the direct RBF method is an ill-conditioned approach to a well-conditioned problem. When the shape parameter is small enough, translates of one radial function are very similar to each other, which produces an ill-conditioned system. The RBF-QR method was designed to get around this problem, and to evaluate the interpolant accurately by analytically removing the ill-conditioning of the matrix.

In Figure C.1, we show a few problems on which the RBF method has been applied. In each one of these problems, it was necessary to remove the ill-conditioning (using the Contour-Padé method or using the RBF-QR method) to explore the error as a function of the shape parameter, to ultimately find the optimal shape parameter value in each context.

4.2.2 RBF methodology

In this section, we give a brief introduction of the RBF method and of how it can be modified to solve PDEs.

4.2.3 Time dependent PDE on a sphere

4.2.3.1 Test problem

We consider the standard convection test problem around the surface of the sphere ([12], [17], [42], [4]). We use a different notation for the spherical coordinate system than in the preceding chapter:

$$\begin{cases} x &= \rho \cos\varphi \cos\theta \\ y &= \rho \sin\varphi \cos\theta \\ z &= \rho \sin\theta \end{cases} .$$

In this coordinate system, the convective-type PDE test problem can be expressed as

$$\frac{\partial u}{\partial t} + \left(\frac{\cos\alpha\cos\theta - \sin\theta\sin\varphi\sin\alpha}{\cos\theta} \right) \frac{\partial u}{\partial \varphi} - \cos\varphi \sin\alpha \frac{\partial u}{\partial \theta} = 0 \tag{4.1}$$

where the convection axis is tilted at the angle α relative to the polar axis, as shown in Figure C.2.

The initial condition which we choose to convect around the sphere is the same cosine bell as the one defined in Chapter 3, Equation (3.2).

4.2.3.2 Different node distributions

Because solving (4.1) on random distributions doesn't give nearly as nice results, we consider only solving it on near-uniform distributions. Two such distributions are used in this work, the ME (minimum energy; equilibrium state after letting particules with equal charges repel each other) and the MD (maximum determinant; maximized determinant of the Gram-matrix) node distributions (Figure C.4). In the shape pa-

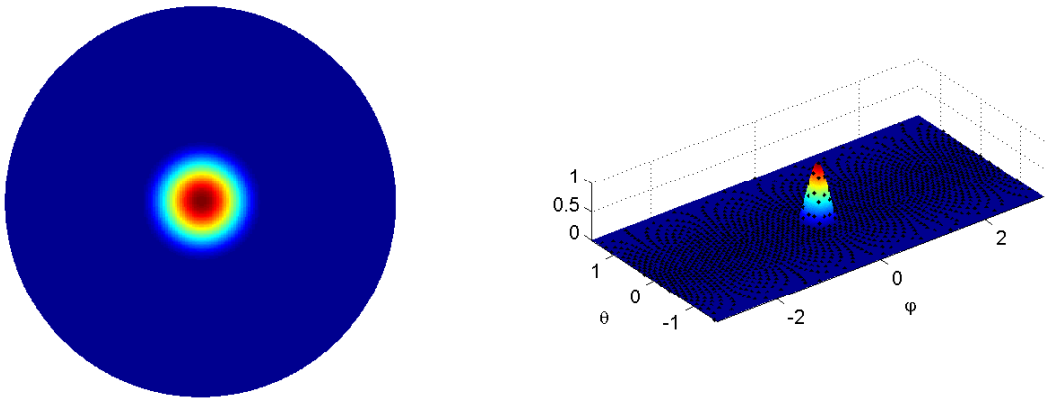

Figure 4.3: Illustrations of the Cosine bell (initial state) on the sphere surface, viewed from positive x-direction, and on an 'unrolled' φ, θ-plane (with the $n = 1849$ ME node locations also marked).

rameter regime where the direct method can be used safely (i.e. $\varepsilon \gg 1$), the two node distributions give the same error. However, when ε is small, the error obtained via solving the PDE on the two types of distribution is drastically different from one node set to the next. In fact, it has been observed that solving the PDE using spherical harmonics on the two different node sets gives extremely different results. Since we showed that the RBF interpolant converges towards the SPH interpolant as $\varepsilon \to 0$, it makes sense that RBFs with small shape parameters will also suffer a difference between the two distributions.

4.2.3.3 Method of lines formulation and time stepping

The method of lines (MOL) consists in discretizing the spatial operator and solving a system of ODEs in time. Thus, after rewriting the PDE as $\frac{\partial u}{\partial t} + L(u) = 0$, we approximate the continuous spatial operator of (4.1), L, using RBFs. We end up with the system of ODEs $\frac{d}{dt}\underline{u} + D\underline{u} = 0$ which we can either solve numerically, or exactly as $\underline{u}(t) = e^{-Dt}\underline{u}(0)$. The matrix D is the differentiation matrix and is defined as $D = B \cdot A^{-1}$, where A is defined in Equation (C.9) and B, in Equation (C.8). The matrix D will have purely imaginary eigenvalues since it is, by construction, a product of an antisymmetric with a positive definite matrix. The matrices A and B can also be defined using the RBF-QR basis. This allows us to remove analytically the ill-conditioning emerging when ε is small enough, as we showed in Chapter 3.

4.2.3.4 Numerical Tests

As we mentioned earlier, the error depends also on the node distribution which is being used. In fact, SPH (thus also small shape parameter RBFs) produce very inaccurate interpolants on the ME node distribution, Figure C.5, while they produce nice results on the MD node distribution. In order to homogenize the results with respect to node distributions (i.e. dispose of any singularity of the SPH method with

respect to the type of node set being used), we over-sample the lat/long grid and use a Least-Squares fit to smoothen the 'interpolant' of the initial condition of the bell, Figure C.6. This allows us to guarantee that the error does not come from an inaccurately interpolated initial state.

Figure C.7 shows the error of convection after $time = 10$ and $time = 10,000$ (one revolution corresponds to $time = 2\pi$). In subplot (a), we show the error obtained via the IMQ RBF, while in subplot (b), via the W6 RBF (Wendland of the 6^{th} order). We notice that the error doesn't increase much in the case of the infinitely smooth RBF, while in the case of the piecewise smooth one, the error increases drastically in time. We notice the same phenomenon in Figure C.8.

4.2.4 Comparisons between different RBF types

We show in Figures C.9 and C.10 the error of convection after $time = 10$ and $time = 10,000$ for all of the most common radial functions, in function of the shape parameter. We observe the same trend as before. The infinitely smooth radial functions perform admirably; the error increase is hardly visible from $time = 10$ to $time = 10,000$. On the other hand, all the piecewise smooth radial functions only perform reasonably for small integration time. We also notice that the error first decays then stabilizes as the shape parameter ε decreases. In fact, it seems that the minimum error is attained for smaller shape parameters as the integration time increases.

4.2.5 Analysis of the numerical results via properties of the DMs

Numerically solving this test problem introduces three sources of error: the discretization (differentiation matrix), the time stepping, and the error introduced when interpolating the solution in between the grid points. We only consider here the error introduced by the differentiation matrix. As we mentioned earlier, the method of lines approach is used, thus (4.1) is discretized as $\frac{d}{dt}\underline{u} + D\underline{u} = 0$ which is then solved

analytically $\underline{u}(t) = \underline{u}(0)e^{-Dt}$. In 1-D, we consider the analogous convection problem [14]

$$u_t = u_x$$

Assuming that $u(x) = e^{i\omega x}$, the true 1st derivative of $u(x)$ is $\frac{d}{dx}u(x) = i\omega e^{i\omega x}$. The second order finite difference gives an approximation of the first derivative of $u(x)$ as

$$\frac{u(x+h) - u(x-h)}{2h} = i\frac{\sin(\omega h)}{h}e^{i\omega x}$$

Plotting against ω the coefficients of $ie^{i\omega x}$, we see that FD2 is only accurate for small frequency ω. It does not resolve higher frequencies. The higher the order of the spatial approximation, the closer the coefficient is to ω, the exact coefficient of $ie^{i\omega x}$, Figure C.11. In the limit of increasing orders, we obtain the pseudospectral method, the Fourier PS method, which resolves exactly every possible mode that can be present with spacing h. We note that, although FD2 might be more accurate than PS for small time integration (since it features a smaller Gibbs phenomenon), PS yields an error that grows slower with time than FD2. The latter is because FD2 cannot resolve the high frequencies intrinsic to the solution. The error then accumulates and grows faster than it would if we had used a higher order solver.

On the sphere, using the RBF-QR method, we compute the differentiation matrices associated with different ε values and we analyse their properties. Our work consists of finding how the time-stepping error will be influenced by these properties. Indeed, we are looking for a similar pattern to the one illustrated in Figure C.11 for the 1-D case. We see that as $\varepsilon \to 0$, the eigenvalues become optimal and the highest SPH modes get resolved. However, as epsilon is larger, we lose the resolution of the highest modes. Thus, the larger the ε, the faster the error grows for long time integration and we can therefore expect a smaller accumulation of error when ε is small. The error for the short time integration therefore comes from the interpolation only, rather than from the differentiation matrix. Understanding this phenomenon provides us with a guide

on how to choose ε in different cases such as short versus long time integrations, Figure C.16.

4.2.6 Conclusions

In this section, we give a brief summary of the results and conclude.

4.3 Additional work

4.3.1 Routine for associated Legendre functions

Having a reliable routine that evaluates associated Legendre functions accurately is very important when we are working with SPH. The SPH expansions, on which the RBF-QR method is based, are sometimes only truncated after thousands of terms (e.g. when $\varepsilon \approx 1$). Thus, we need a routine which can evaluate the associated Legendre functions to machine precision, even for very large degrees μ. It came to our attention that *Matlab*'s *legendre*() routine was based on a three-term recursion relation which contains singularities at $x = \pm 1$. Around these points, an asymptotic formula is used, which adds complexity to the routine. The normalization used is only efficient for small degrees of the associated Legendre functions.

We present a method which is simpler than *Matlab*'s and which gives reliable results also for large degrees μ. This new routine can also be modified easily to give derivatives of the associated Legendre functions.

Consider the three-term recursion relation, which is the core of *Matlab*'s routine.

$$P_\mu^{\nu-1}(x) = \frac{-1}{(\mu+\nu)(\mu-\nu+1)} \left(P_\mu^{\nu+1}(x) + 2\nu \frac{x}{\sqrt{1-x^2}} P_\mu^\nu(x) \right)$$

By definition,

$$P_\mu^\nu(x) = (-1)^\nu (1-x^2)^{\nu/2} \frac{d^\nu}{dx^\nu} P_\mu(x)$$

Now, let $M_\mu^\nu(x) = (-1)^\nu \frac{d^\nu}{dx^\nu} P_\mu(x)$. Then, $P_\mu^\nu(x) = (1-x^2)^{\nu/2} M_\mu^\nu(x)$. Substituting

$(1-x^2)^{\nu/2}M_\mu^\nu(x)$ for $P_\mu^\nu(x)$ in the three-term recursion relation, we get this new three-term recursion relation, this time, for $M_\mu^\nu(x)$.

$$M_\mu^{\nu-1}(x) = \frac{-1}{(\mu+\nu)(\mu-\nu+1)}\left(M_\mu^{\nu+1}(x)(1-x^2) + 2\nu x M_\mu^\nu(x)\right)$$

This relation is singularity-free. It has been stated earlier [32], but apparently was never used as a means of more effective numerical computations. The method consists of first finding $M_\mu^\nu(x)$ values with the latter formula, and then finding $P_\mu^\nu(x) = (1-x^2)^{\nu/2}M_\mu^\nu(x)$. This routine suffers some ill-conditioning at the moment and requires some more work before being used efficiently.

4.3.2 Expansion coefficients for IQ, W2, W4, W6 and TPS

4.3.2.1 Hubbert and Baxter's methodology [26]

Restricting the formula to S^2, we obtain

$$\begin{aligned} ||\overrightarrow{\xi} - \overrightarrow{\eta}|| &= \sqrt{(x_\xi - x_\eta)^2 - (y_\xi - y_\eta)^2 - (z_\xi - z_\eta)^2} \\ &= \sqrt{(x_\xi^2 + y_\xi^2 + z_\xi^2) + (x_\eta^2 + y_\eta^2 + z_\eta^2) - 2x_\eta x_\xi - 2y_\eta y_\xi - 2z_\eta z_\xi} \\ &= \sqrt{2 - 2\,\overrightarrow{\xi}.\overrightarrow{\eta}} \end{aligned}$$

As usual, we denote our radial basis function as $\phi(r)$. Let $\psi(\overrightarrow{\xi}.\overrightarrow{\eta}) = \phi(\sqrt{2-2\,\overrightarrow{\xi}.\overrightarrow{\eta}})$. When $\phi(r)$ is conditionally positive definite $\psi(t)$ has the Legendre expansion

$$\psi(t) = \sum_{k=0}^{\infty} a_k P_k(t)$$

Now, because of the addition theorem

$$\sum_{l=-k}^{k} Y_k^l(\overrightarrow{\xi})Y_k^l(\overrightarrow{\eta}) = \frac{2k+1}{4\pi}P_k(\overrightarrow{\xi}.\overrightarrow{\eta})$$

we have

$$\psi(\overrightarrow{\xi}.\overrightarrow{\eta}) = \sum_{k=0}^{\infty}\sum_{l=-k}^{k} \text{`}c_k Y_k^l(\overrightarrow{\xi})Y_k^l(\overrightarrow{\eta})$$

where, using Rodrigues representation,

$$c_k = \frac{\pi}{2^{k-2}k!}\int_{-1}^{1}(1-t^2)^k\frac{d^k}{dt^k}\psi(t)dt. \tag{4.2}$$

With the development of the RBF-QR method, it has become necessary to find the expansion coefficients for the common radial basis functions. Baxter and Hubbert found the expansion coefficients for most of the most common radial functions (GA, TPS, IMQ and MQ), but not for certain others, such as IQ or the Wendland functions, which we will find, using their methodology.

4.3.2.2 IQ

We apply the method to the inverse quadratic radial basis function

$$\phi(r) = \frac{1}{1+\varepsilon^2 r^2}$$

Because IQ is strictly positive definite, we change notation $\psi(r) = \phi(r^{1/2})$ and then find that

$$\frac{d^k}{dt^k}\psi(t) = (2\varepsilon^2)^k k!(1+2\varepsilon^2-2\varepsilon^2 t)^{-k-1}$$

Therefore, using the identity

$$\int_0^1 (1-zu)^{-a}(1-u)^{c-b-1}u^{b-1}du = \frac{\Gamma(b)\Gamma(c-b)}{\Gamma(c)}\ {}_2F_1(a,b;c;z)$$

we get

$$\begin{aligned} c_k &= \frac{\pi}{2^{k-2}k!}\int_{-1}^{1}\frac{d^k}{dt^k}\psi(t)\ (1-t^2)^k dt \\ &= \frac{4\pi^{3/2}k!}{\Gamma(k+3/2)(1+4\varepsilon^2)^{k+1}}\ {}_2F_1(k+1,k+1;2k+2;\frac{4\varepsilon^2}{1+4\varepsilon^2})\varepsilon^{2k} \end{aligned}$$

4.3.2.3 Wendland

The SPH expansion coefficients for the Wendland functions W2 and the description of the method that is followed are included in the Appendix B of [19]. We also explain the modifications that should be made to the RBF-QR code in the case of such a piecewise function. We have also derived corresponding formulas for W4 and W6. They are algebraically very complex.

4.3.2.4 TPS

Consider the thin plate spline (TPS) radial function

$$\phi(r) = \varepsilon^2 r^2 \log(\varepsilon r)$$

We find its expansion in terms of SPH with Hubbert and Baxter's formula

$$\phi(\|\underline{x} - \underline{x}_i\|) = \sum_{\mu=0}^{\infty} \sum_{\nu=-\mu}^{\mu} {}'\{c_\mu \, Y_\mu{}^\nu(\underline{x}_i)\} \, Y_\mu{}^\nu(\underline{x})$$

where

$$c_\mu = \frac{\pi}{2^{\mu-2}\mu!} \int_{-1}^{1} \frac{d^\mu}{dt^\mu} \phi\left(\sqrt{2-2t}\right) (1-t^2)^\mu dt$$

We find that

$$\frac{d}{dt}\phi\left(\sqrt{2-2t}\right) = -\varepsilon^2(\log(2\varepsilon^2(1-t)) + 1) \tag{4.3}$$

$$\frac{d^\mu}{dt^\mu}\phi\left(\sqrt{2-2t}\right) = (\mu-2)!\varepsilon^2(1-t)^{-\mu+1}, \mu > 1 \tag{4.4}$$

Thus,

$$c_0 = 4\pi\varepsilon^2(-1 + 2\log(4\varepsilon^2)) \tag{4.5}$$

$$c_1 = -\frac{4\pi\varepsilon^2}{9}(1 + \log(4096) + 6\log(\varepsilon^2)) \tag{4.6}$$

$$c_\mu = \frac{\pi\varepsilon^2 2^4}{\mu(\mu^2-1)(\mu+2)}, \mu = 2, 3, ... \tag{4.7}$$

- For any shape parameter value, the series will converge with $O(1/\mu^4)$.

- The shape parameter appears as the factor ε^2 in all the coefficients. We can thus pull it out of the expansion nearly completely (the first two terms only will still contain ε). This presence of ε in the first two terms is thus the only ε-dependence of the method.

- We can most definitely adapt the RBF-QR method to this radial function. Actually, no QR factorization would even be necessary since we can remove the ε powers right away. However, the slow convergence will make it difficult to use the RBF-QR method at all. We would need about $(10^4)^2 = 10^8$ terms in the expansion to reach machine-precision.

4.3.3 Removal of the singularities at the poles when computing the spherical harmonics and their derivatives

Consider the test problem (4.1). We notice that using radial basis functions $u(\overrightarrow{x}) = \sum_{i=1}^{N} \lambda_i \phi(||\overrightarrow{x} - \overrightarrow{x}_i||)$, the singularity at the poles due to $\cos\theta$ on the denominator is removed, which leads to a singularity-free problem.

Removing the singularity at the poles when we use SPH expansions is a bit tricky. Indeed, not only do we have a problem with the $\cos\theta$ on the denominator of the first term, but we also have a singularity at the poles coming from the derivative of the associated Legendre polynomial in the second term. Recall that the SPH in spherical coordinates are given by

$$Y_\mu^{\ \nu}(\theta,\varphi) = \begin{cases} \sqrt{\frac{2\mu+1}{4\pi}}\sqrt{\frac{(\mu-\nu)!}{(\mu+\nu)!}} P_\mu^\nu(\sin\theta)\cos(\nu\varphi) & , \quad \nu = 0,1,\ldots,\mu \\ \sqrt{\frac{2\mu+1}{4\pi}}\sqrt{\frac{(\mu+\nu)!}{(\mu-\nu)!}} P_\mu^{-\nu}(\sin\theta)\sin(-\nu\varphi) & , \quad \nu = -\mu,\ldots,-1 \end{cases}$$

4.3.3.1 $\frac{\partial u}{\partial \theta}$-term

$$\frac{\partial}{\partial\theta} Y_\mu^{\ \nu}(\theta,\varphi) \tag{4.8}$$

$$= \begin{cases} \sqrt{\frac{2\mu+1}{4\pi}}\sqrt{\frac{(\mu-\nu)!}{(\mu+\nu)!}}\frac{\partial}{\partial\theta}(P_\mu^\nu(\sin\theta))\cos(\nu\varphi) & , \quad \nu = 0, 1, \ldots, \mu \\ \sqrt{\frac{2\mu+1}{4\pi}}\sqrt{\frac{(\mu+\nu)!}{(\mu-\nu)!}}\frac{\partial}{\partial\theta}(P_\mu^{-\nu}(\sin\theta))\sin(-\nu\varphi) & , \quad \nu = -\mu, \ldots, -1 \end{cases} . \tag{4.9}$$

$$= \begin{cases} \sqrt{\frac{2\mu+1}{4\pi}}\sqrt{\frac{(\mu-\nu)!}{(\mu+\nu)!}}\cos\theta\frac{\partial}{\partial x}(P_\mu^\nu(x))|_{x=\sin\theta}\cos(\nu\varphi) & , \quad \nu = 0, 1, \ldots, \mu \\ \sqrt{\frac{2\mu+1}{4\pi}}\sqrt{\frac{(\mu+\nu)!}{(\mu-\nu)!}}\cos\theta\frac{\partial}{\partial x}(P_\mu^{-\nu}(x))|_{x=\sin\theta}\sin(-\nu\varphi) & , \quad \nu = -\mu, \ldots, -1 \end{cases} \tag{4.10}$$

We combine identities from [2] to give us

$$\cos\theta\frac{d}{dx}(P_\mu^\nu(x))|_{x=\sin\theta} = \frac{(\mu+\nu)(\mu-\nu+1)P_\mu^{\nu-1}(\sin\theta) - P_\mu^{\nu+1}(\sin\theta)}{2}$$

which is singularity-free everywhere. Special consideration has to be given for the cases where $\nu = 0$ and $\nu = \mu$.

- $\nu = 0$

$$\cos\theta\frac{d}{dx}(P_\mu^0(x))|_{x=\sin\theta} = \frac{(\mu)(\mu+1)P_\mu^{-1}(\sin\theta) - P_\mu^1(\sin\theta)}{2} = -P_\mu^1(\sin\theta)$$

- $\nu = \mu$

$$\cos\theta\frac{d}{dx}(P_\mu^\mu(x))|_{x=\sin\theta} = \frac{2\mu P_\mu^{\mu-1}(\sin\theta) - P_\mu^{\mu+1}(\sin\theta)}{2} = \mu P_\mu^{\mu-1}(\sin\theta)$$

4.3.3.2 $\frac{\partial u}{\partial\varphi}$-term

Using the technique considered in Section 4.3.1 allows us to compute $\frac{P_\mu^\nu(\sin\theta)}{\cos\theta}$ safely.

Chapter 5

RBF method with spatially variable shape parameters applied to a convective type PDE on the surface of the sphere

5.1 Introduction

Through this document, we have identified the two ways in which the error can grow as the radial functions become flat. The first is the ill-conditioning linked to the direct implementation of the RBF algorithm, which we resolved using the RBF-QR method. The second is the Runge phenomenon. According to Fornberg and Zuev [22], the negative effects of this phenomenon can be reduced considerably when we refine nodes and introduce a spatially variable shape parameter in the RBF representation of the interpolant

$$s(\underline{x}) = \sum_{i=1}^{n} \lambda_i \ \phi_{\epsilon_i}(\|\underline{x} - \underline{x}_i\|), \tag{5.1}$$

In this chapter, we introduce the modified RBF-QR algorithm which allows us to compute the interpolant and the solution to PDEs for both small and spatially variable shape parameters. We also apply the spatially variable shape parameter algorithm to the purely convective equation on the circle and on the surface of the sphere.

This research project is still in progress. Although it connects with recent work by Natasha Flyer and Erik Lehto, it is being pursued by the author as the sole investigator.

5.1.1 RBF-QR for spatially variable ε

Following the development of the RBF-QR method in Chapter 3, we want to create the upper triangular matrix R out of B, with the least amount of information loss. To do so, it wil be necessary to combine the rows together, such that the orders of magnitude of the combined terms are similar. We order the rows from the ones associated with the smallest ε to the ones associated with the largest ε. We then perform the QR factorization block by block and normalize R (identical as extracting the E matrix containing the powers of ε, when ε is fixed.)

The new QR algorithm goes as follows: Let matrix B have the form

$$B = \begin{bmatrix} \cdots & \cdots & B_1 & \cdots & \cdots \\ & & B_2 & & \\ & & B_3 & & \\ & & \vdots & & \\ \cdots & \cdots & B_m & \cdots & \cdots \end{bmatrix}$$

with $B_1, B_2, ...$ being the composing blocks of matrix B.

- Step 1: Perform a QR factorization on the 1st block

$$B = \begin{bmatrix} Q_1 & & & & \\ & I & & & \\ & & I & & \\ & & & \ddots & \\ & & & & I \end{bmatrix} \begin{bmatrix} \cdots & \cdots & B_1 & \cdots & \cdots \\ & & B_2 & & \\ & & B_3 & & \\ & & \vdots & & \\ \cdots & \cdots & B_m & \cdots & \cdots \end{bmatrix}$$

- Step 2: Normalize R_1

- Step 3: zero out the elements of the 1st column below R_1. (Call that transfor-

mation L1)

$$B = \begin{bmatrix} Q_1 & & & & \\ & I & & & \\ & & I & & \\ & & & \ddots & \\ & & & & I \end{bmatrix} \begin{bmatrix} & & & \\ & & L_1 & \\ & & & \end{bmatrix} \left[\begin{array}{c|cccc} \ddots & \cdots & R_1 & \cdots & \cdots \\ \hline 0 & \cdots & B_2^1 & \cdots & \cdots \\ 0 & & B_3^1 & & \\ 0 & & \vdots & & \\ 0 & \cdots & B_m^1 & \cdots & \cdots \end{array}\right]$$

- Step 4: Normalize R_2
- Step 5: zero out the elements of the 2nd, 3rd and 4th columns below R_2.(call that transformation L2)

$$B = \begin{bmatrix} Q_1 & & & & \\ & I & & & \\ & & I & & \\ & & & \ddots & \\ & & & & I \end{bmatrix} \begin{bmatrix} & & & \\ & & L_1 & \\ & & & \end{bmatrix} \times$$

$$\times \begin{bmatrix} I & & & & \\ & Q_2 & & & \\ & & I & & \\ & & & \ddots & \\ & & & & I \end{bmatrix} \begin{bmatrix} & & & \\ & & L_2 & \\ & & & \end{bmatrix} \left[\begin{array}{ccc|cc} \ddots & \cdots & R_1 & \cdots & \cdots \\ 0 & \ddots & R_2 & \cdots & \cdots \\ \hline 0 & 0 & \cdots & B_3^2 & \cdots \\ 0 & 0 & & \vdots & \\ 0 & 0 & \cdots & B_m^2 & \cdots \end{array}\right]$$

- and so on.
- Finally we have $B = C.R$, where C is **not** a unitary matrix and holds the powers of ε, and where R is uppertriangular.

The RBF-QR method gives an opportunity to have an algorithm for solving stably the interpolation problem for spatially variable ε on the surface of a sphere. The key modifications to the algorithm for fixed ε is first the ordering of the rows in matrix B, such that they correspond to the smallest to the largest ε. It is secondly the block by block QR factorization of matrix B. Because in each block, the ε_i are in order and hopefully close to each other in magnitude, terms of dramatically different orders of magnitude won't be combined.

5.2 Solving a convective type PDE on the surface of a node refined sphere using the variable shape parameter RBF method.

5.2.1 Introduction

The goal is once again to solve a convective type PDE on the surface of the sphere. The reason for refining the nodes and to use the variable shape parameter is to get rid of, or at least to reduce the Runge phenomenon, more and more destructive as $\varepsilon \to 0$. Thus, we want the node distribution to contain a refined region. In order to deal with this node refinement, we let the shape parameter vary spatially. It was shown in [22] that the rule of the nearest neighbor gives nice results. We will adopt this rule and let the shape parameter associated with a specific node point be proportional to the inverse of the distance from this node to its nearest neighbor. We study the error of convecting a cosine bell around the sphere, going through the refined area. However, if the shape parameter varies spatially, the eigenvalues will not be purely imaginary anymore (the eigenvalues of a positive definite matrix with an antisymmetric matrix must be purely imaginary, [19]) and the ones with a large real part will raise the error exponentially. Thus we will either have an error caused by the Runge phenomenon (and not by the eigenvalues' real parts) or an error caused by the eigenvalues' real parts (and not by the Runge phenomenon.) The ultimate objective will be to understand the error enough to

find an appropriate filter.

5.2.2 Node distribution

In order to create a 'minimum energy'-type distribution with a node refinement, we allocate a charge to each node and allow them to repulse each other. In the case of the minimum energy node distribution, the charges associated with each node are identical. After letting each particle repel its neighbors, we end up with a balanced near-uniform node distribution. Now, letting the charges of the nodes in a certain area be smaller than the others will have the effect of attracting more nodes in this specific region, thus creating a refined node distribution.

5.2.3 The rule of the nearest neighbor

The nearest neighbor rule introduced by Fornberg & Zuev in [22] implies that the shape parameter associated with a particular node must be proportional to the distance to the node's nearest neighbor. This insures that the areas where the nodes are sparse and distant from one another will be covered by flat radial functions while the refined areas will have peaked and narrow radial functions, perfect to interpolate on denser node sets. We redefine the shape parameter as $\varepsilon_i = \varepsilon.\frac{\max(||x_j - x_k||)_{j,k=1,\ldots,Nj\neq i}}{\min(||x_j - x_i||)_{j=1,\ldots,Nj\neq i}}$when using the RBF-Direct method. Thus we have $\varepsilon_i = \varepsilon.\frac{d}{\min(||x_j - x_i||)_{j=1,\ldots,Nj\neq i}}$, with the scalar $d = \max(||x_j - x_k||)_{j,k=1,\ldots,Nj\neq i}$ being the normalizing factor that insures that the nearest neighbor inverse function has a minimum value of one, since using the direct method, it is important to control the **smallest** value of the shape parameter. We define $\varepsilon_i = \varepsilon.\frac{\min(||x_j - x_k||)_{j,k=1,\ldots,Nj\neq i}}{\min(||x_j - x_i||)_{j=1,\ldots,Nj\neq i}}$when using the RBF-QR method, because it is now the **largest** value of the shape parameter vector that has to be controled and thus is set to one.

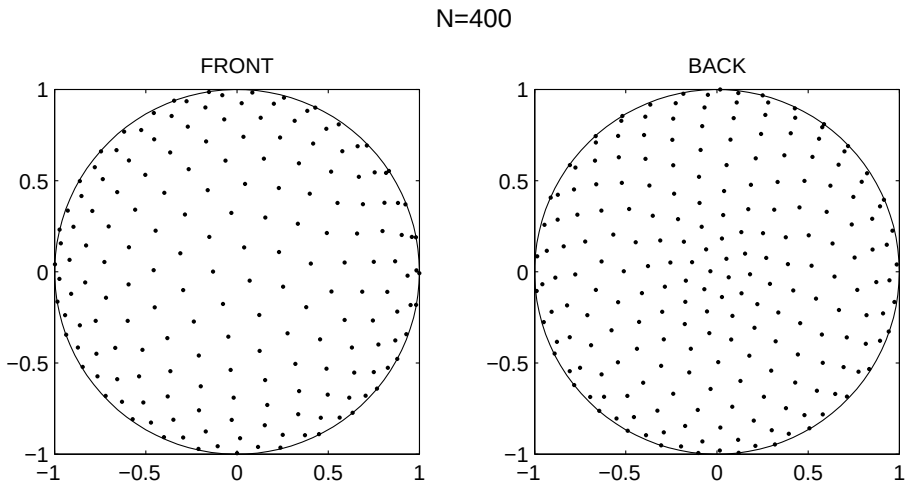

Figure 5.1: Node distribution on the surface of the sphere with a refined area.

5.2.4 Differentiation matrix

We choose to use the method of lines to solve this problem. Thus, we discretize in space (hence produce a differentiation matrix) and solve a system of ODEs in time. Analysing the error produced by discretizing the spatial operator will amount to studying the eigenvalues of the differentiation matrix, which we obtain using RBFs. Thus, as in Chapter 4, the method of lines representation of the problem is $u_t = D \cdot u$, which has the analytical solution $\overrightarrow{u}(t) = e^{D \cdot t} \cdot \overrightarrow{u}_0$. Assuming that the differentiation matrix D is not too far from being normal (meaning that it has orthogonal eigenvectors), by projecting the vector $\overrightarrow{u}_0$ onto the eigenspace of D, we get $\overrightarrow{u}_0 = \sum_{j=1}^{N} \alpha_j \overrightarrow{v}_j$, where $\overrightarrow{v}_j$ is the eigenvector associated with the eigenvalue λ_j.

By definition,

$$e^{D \cdot t} = \sum_{n=0}^{\infty} \frac{(D \cdot t)^n}{n!} \tag{5.2}$$

Consequently,

$$\begin{aligned} e^{D \cdot t} \cdot \overrightarrow{v}_j &= \sum_{n=0}^{\infty} \frac{(D \cdot t)^n}{n!} . \overrightarrow{v}_j \\ &= \sum_{n=0}^{\infty} \frac{t^n}{n!} . (D^n \cdot \overrightarrow{v}_j) \\ &= \sum_{n=0}^{\infty} \frac{t^n}{n!} . (\lambda_j^n \cdot \overrightarrow{v}_j) \\ &= e^{\lambda_j \cdot t} \cdot \overrightarrow{v}_j \end{aligned}$$

Thus,

$$\begin{aligned} \overrightarrow{u}(t) &= e^{D \cdot t} \cdot \overrightarrow{u}_0 \\ &= \sum_{j=1}^{N} \alpha_j (e^{D \cdot t} \cdot \overrightarrow{v}_j) \\ &= \sum_{j=1}^{N} \alpha_j (e^{\lambda_j \cdot t} \cdot \overrightarrow{v}_j) \end{aligned}$$

This representation of the solution allows us to see more clearly that the positive real parts of the eigenvalues will make the error grow exponentially in time, and that the

leading eigenvector will be the one associated with the largest positive real part of these eigenvalues.

5.2.5 Numerical results

Conceptually, we can think of the error as follows. The differentiation matrix that we obtain allows us to convect and resolve the bell, as accurately as the grid will allow. The fact that some region of the domain has been refined implies that higher modes will not be able to be resolved on the sparser areas (Figure 5.1 shows the node distribution used throughout this section). These high modes will be misrepresented as low modes and create errors. It seems that a filter, which will take into consideration the different regions will be necessary to solve this problem. We compute the differentiation matrix via the RBF-QR method and examine the error in function of the way in which we choose the shape parameter values.

5.2.5.1 Scaling of the shape parameters

- We define the shape parameter values as $\{\varepsilon_j = \varepsilon.f(\min ||x_j - x_i||)\}_{j=1}^{N}$, where the function f is the 'shape parameter scheme', such as the 'rule of the nearest neighbor' for example. As $\varepsilon \to 0$, the RBF interpolant tends towards the SPH interpolant. The proof is identical to the one presented in [18] for the case of fixed shape parameters.

  Thus, as $\varepsilon \to 0$

  * The eigenvalues become purely imaginary and all fall on integer values.
  * The Runge phenomenon appears, brought by the polynomial character of the SPH on a non-uniform distribution.
  * Thus, although the error is not produced by the dominance of the eigenvector associated with the eigenvalues' largest real part (because all the

eigenvalues are purely imaginary), it increases tremendously because of the Runge phenomenon. Thus, this $\varepsilon \to 0$ limit might be far from being the best choice.

- Notice that if we now define the shape parameter values as $\{\varepsilon_j = a + \varepsilon.f(\min ||x_j - x_i||)\}_{j=1}^{N}$, where a is real (thus a perturbation of order ε away from a), by letting $\varepsilon \to 0$

  * The eigenvalues become purely imaginary. This is because the shape parameter values become fixed. We showed that, in this case, the eigenvalues of a positive definite matrix with an antisymmetric matrix must be purely imaginary. We loose these criteria with the variable shape parameters [19].

  * The Runge phenomenon appears once again, brought by the non-uniform character of the distribution with a fixed shape parameter.

  * Figure 5.2 shows how we can 'control' the magnitude of the largest real part of the eigenvalues with the magnitude of ε. We see a clear dependence of the order of the perturbation ε, on the magnitude of the largest real parts of the eigenvalues.

5.2.5.2 Shape parameter schemes

The rule of the nearest neighbor is the scheme we have used so far to assign values to each node's shape parameter. As we will see, the error depends strongly on the scheme which we use to find the shape parameters, and on how we scale them. Earlier, we explained how the scaling affects the error. We now consider the error induced by the different schemes.

The rule of the nearest neighbor ($\varepsilon_j = \varepsilon.\frac{1}{\min ||x_j - x_i||}$) [22]

It consists in assigning small shape parameter values to the nodes that belong to 'sparse' areas and large values to the nodes that belong to the refined area. This

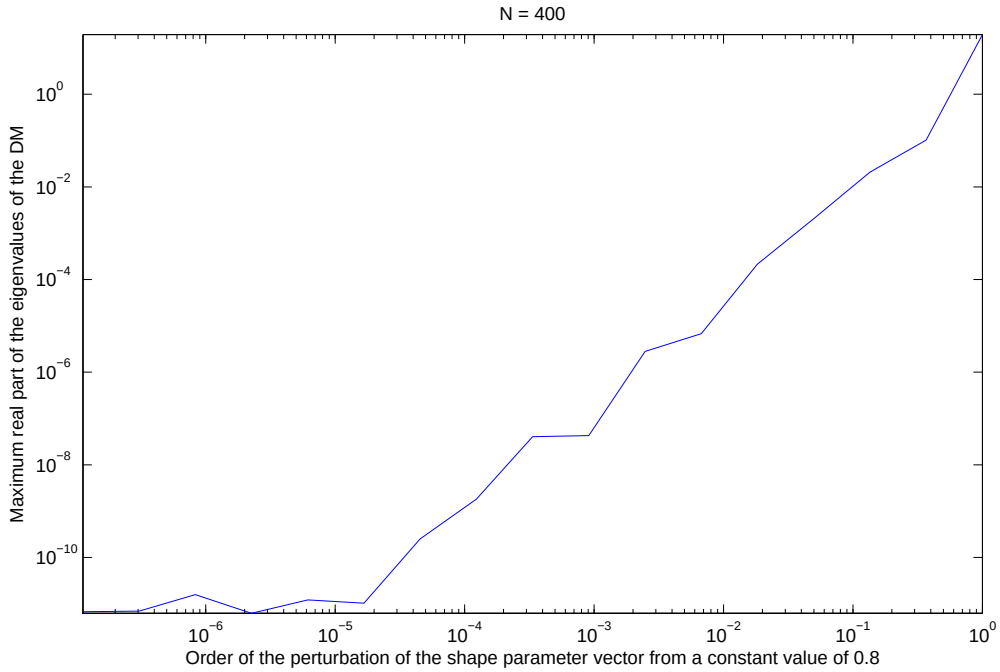

Figure 5.2: Dependence of ϵ on the magnitude of the eigenvalues largest real parts.

should allow the 'rougher' surfaces to be better represented since the radial functions are steeper in these (refined) regions.

This rule seems to be the least effective so far. The differentiation matrix that we obtain via this method has eigenvalues with large real parts. The eigenvectors (and their conjugates) associated with these eigenvalues become quickly dominate the other eigenvectors, destroying the solution.

$1rev/2\pi$	$t=0$	$t=2$	$t=4$	$t=6$	$t=8$	$t=10$	$t=12$	$t=14$
Error	0	0.042	0.059	0.167	0.408	0.972	1.532	4.464

In Figure 5.3 we show the 2-D Fourier transform of the solution (interpolated on a regular grid). Although taking the Fourier transform isn't really appropriate in a non-regular setting, it still gives us an idea of how the different modes evolve. We see that the low modes are quickly overpowered by a few eigenvectors. In Figure 5.4, we show the eigenvector associated with the largest eigenvalue real part ($4.628e-001$). We recognise it in Figure 5.3 as one of the dominating vectors.

The rule of the nearest neighbor, although very effective on the interpolation problem is not as effective when it comes to convecting around the sphere. Indeed, the differentiation matrix resulting from this method has quite large eigenvalue real parts, which we saw earlier, are harmful to the solution. If the eigenvectors associated with the eigenvalues having the largest real parts are high frequency modes, we can easily filter them out. However, if they are low modes, they are instrumental to representing the solution correctly, and cannot be filtered out. We illustrate their detrimental effect in Figure 5.3.

Fixed shape parameter ($\varepsilon_j = \varepsilon$)

We now 'control' the magnitude of the largest eigenvalue real part, using what we observed in Figure 5.2. In this example, we take $\varepsilon = 0.6$.

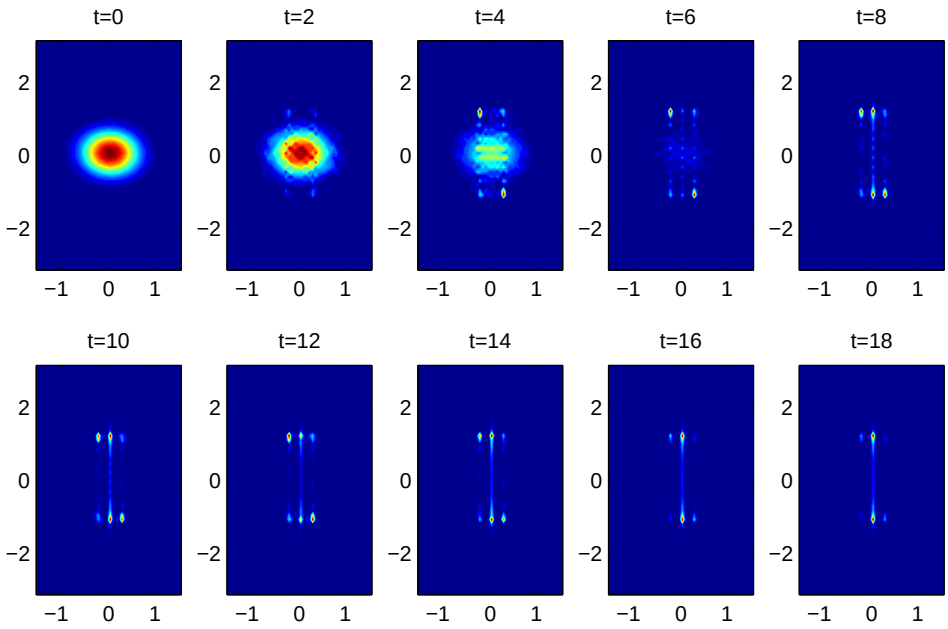

Figure 5.3: Evolution of the Cosine bell in the Fourier space (axes ω_1, ω_2). The rule of the nearest neighbor was used here with $\varepsilon = 0.6$. Notice that the non-zero frequencies are well inside the ω_1, ω_2 plane displayed since the bell was evaluated on a refined grid before the FFT was taken.

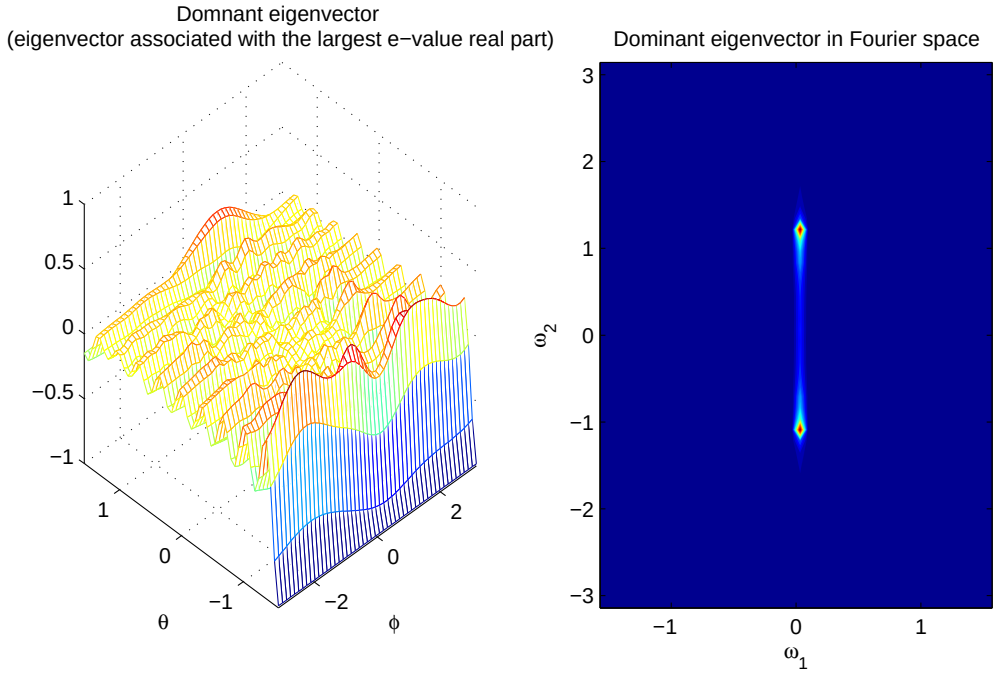

Figure 5.4: Dominant eigenvector

$1rev/2\pi$	$t=0$	$t=10$	$t=20$	$t=30$	$t=40$	$t=50$	$t=60$	$t=70$
Error	0	0.036	0.041	0.037	0.043	0.039	0.046	0.044

The error remains stable throughout the whole process (notice the much larger time steps.) The largest real part of the eigenvalues is now $3.59e{-}011$, which is harmless, and the solution mostly retains its character throughout the whole evolution (see Figure 5.5.) We do see the effect of the Runge phenomenon, growing as time goes on.

Modified rules of the nearest neighbor ($\varepsilon_j = a + \varepsilon \frac{1}{\min ||x_j - x_i||}$ or $\varepsilon_j = a + \varepsilon \cdot rand$, discussed in [22])

These methods often give nice results. They will have to be explored further though.

5.2.6 Conclusion

There seem to be two distinct types of error, depending on the scheme we choose to assign the shape parameter values:

- Error generated by the dominance of large eigenvalue real parts. We show the contour plots of the eigenvectors (using the RBF-QR method with variable shape parameters obeying the rule of the nearest neighbor and with a scaling factor of 0.6) associated with the most dominant eigenvalues in Figures 5.6, 5.7 and 5.8. It seems as if they are highly oscillatory enough that a filtering of high frequencies will probably suffice. When comparing the eigenfunctions against the scattered node locations, we recognize similarities to sawtooth-like modes - the very highest modes any node set can represent.

- Error generated by the Runge phenomenon. By essence, the Runge phenomenon takes the form of high frequency modes. It should therefore also be possible to filter it out.

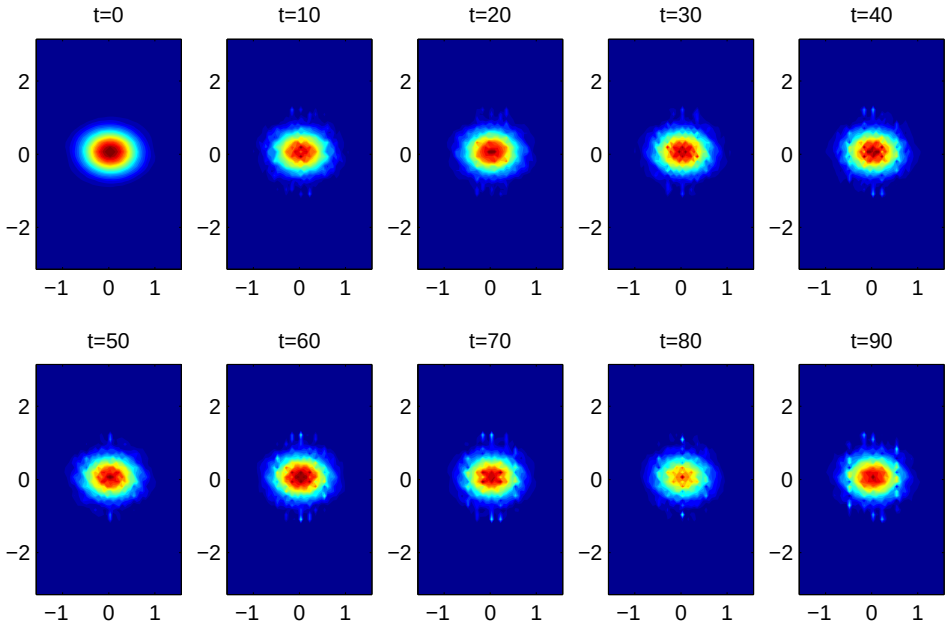

Figure 5.5: Evolution of the Cosine bell in Fourier space (axes ω_1, ω_2). We used a fixed shape parameter here with $\varepsilon = 0.6$

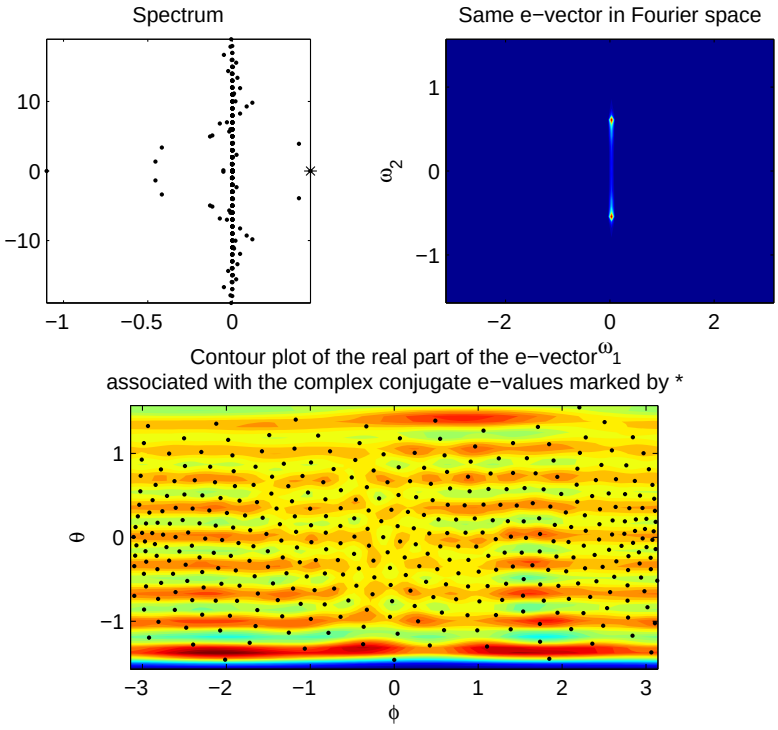

Figure 5.6: Plots of the eigenvectors associated with a few dominant eigenvalues

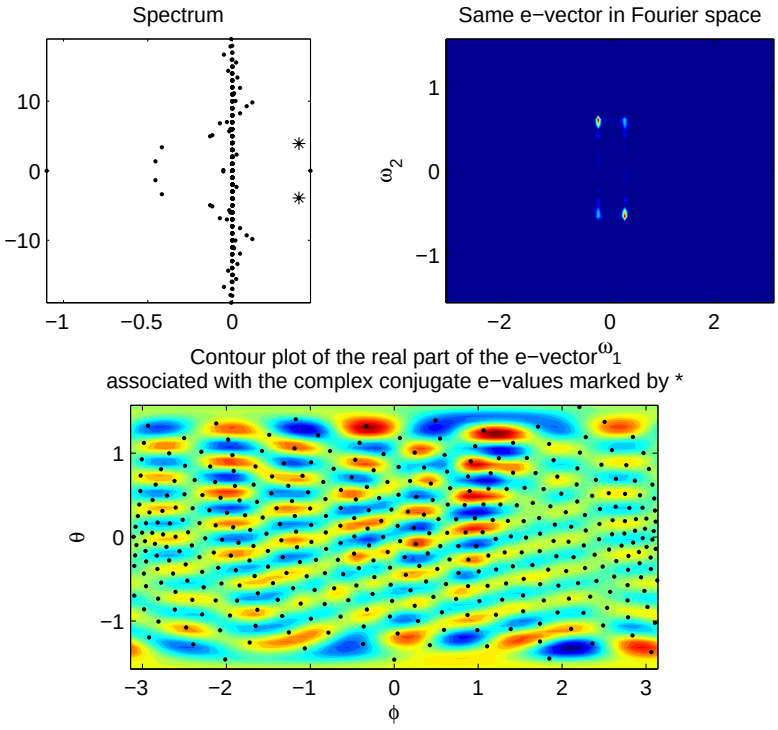

Figure 5.7: Plots of the eigenvectors associated with a few dominant eigenvalues

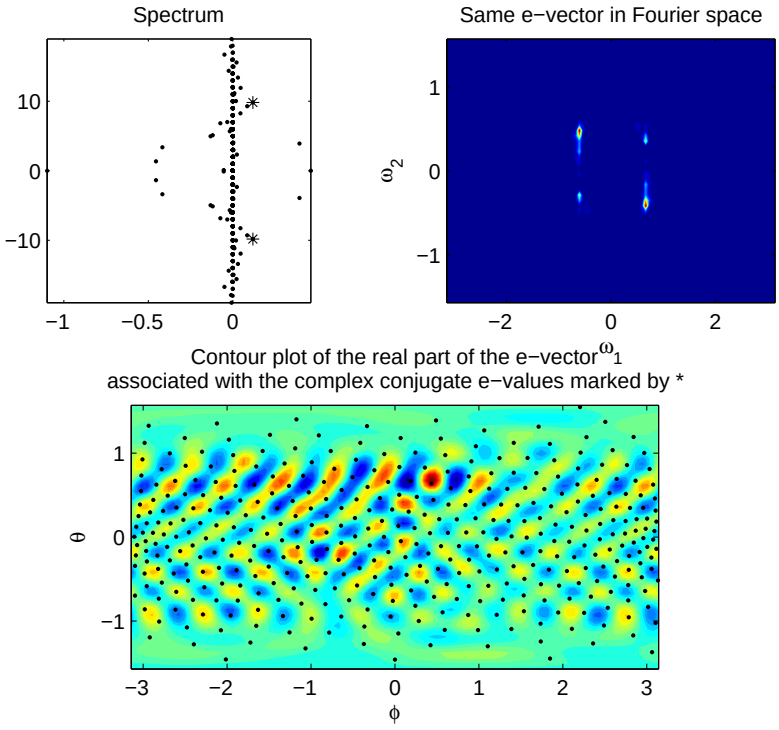

Figure 5.8: Plots of the eigenvectors associated with a few dominant eigenvalues

Chapter 6

Conclusion

6.1 Projects presented in this document

This dissertation contains analytical and numerical advances in radial basis functions. The analysis of the decay rates (Chapter 2) of cardinal coefficients will hopefully advance research towards a fast algorithm. The RBF-QR method opened new doors for accurate and stable interpolation (Chapter 3), solving PDEs on the surface of the sphere (Chapter 4) and for error analysis of the RBF method. Finally, the method applied to refined node distributions with variable shape parameters (Chapter 5) will hopefully prove possible to combine with new filtering techniques and thereby help to establish RBFs as an extremely practical tool for solving PDEs.

6.2 Parallel between RBFs and PS methods

In view of the different results from Chapters 3 and 4, we notice that the best results for interpolation happen away from the limit $\varepsilon \to 0$, while in the case of long time integration, it is exactly approaching this limit that will give us the best possible error. Figure 4.2-3 in [14], illustrates a similar case in 1D using finite differences, with the PS method as the limiting order finite difference. Both the Runge and the Gibbs phenomena play a role in this. Even so, a full theoretical answer to why this happens is still a partly open issue.

6.3 Future projects

- Finish the project developed in Chapter 5, "RBF method with spatially variable shape parameters applied to a convective type PDE on the surface of the sphere"
- Study the RBF PDE solver on arbitrary surfaces.
- Explore the possibility of finding algorithms that are both stable for small ε and at the same time faster than the RBF-Direct method.

Bibliography

[1] Ablowitz M.J.,Fokas A. S., Complex Variables: Introduction and Applications, Cambridge University Press, 1997

[2] Abramowitz, M., Stegun, I.A., Handbook of Mathematical Functions, Dover Publications (1981).

[3] Arfken G. B., Weber H. J. Mathematical Methods For Physicists. Harcourt/Academic Press, London, UK, 2001.

[4] Browning, G.L., Hack, P.N. and Swarztrauber, A comparison of three different numerical methods for solving differential euqations on the sphere, Mon. Wea. Rew. 117 (1989), 1058-1075.

[5] Buhmann, M. D., Multivariate interpolation with radial basis functions, Technical Report DAMPT 1988/NA8, University of Cambridge.

[6] Buhmann, M. D., Radial basis function interpolation on an infinite regular grid, in: Algorithms for Approximation II, eds. J. C. Mason and M. G. Cox, Chapman and Hall, 1990, pp.47-61.

[7] Buhmann, M. D., Radial Basis Functions, Cambridge University Press, 2003.

[8] Driscoll, T.A. and Fornberg, B., Interpolation in the limit of increasingly flat radial basis functions, Comp. Math. with Applications 43 (2002), 413-422.

[9] Duchon, J., Splines minimizing rotation invariant seminorms in sobolev spaces, constructive theory of functions of several variables. vol 1 (1976), pp 85-100.

[10] Fasshauer, G. E., Meshfree Approximation Methods with Matlab, Interdisciplinary Mathematical Sciences - Vol. 6, World Scientific Publishers, Singapore, 2007.

[11] Faul, A. C. and Powell, M. J. D., Krylov subspace methods for radial function interpolation, Numerical Analysis 1999, eds. D. F. Griffiths and G. A. Watson, Chapman and Hall, 2000, pp. 115-141.

[12] N. Flyer and G. Wright, Transport schemes on a sphere using radial basis functions, Journal of Computational Physics. 226 (2007), 1059-1084.

[13] Flyer, N. and Wright, G., Solving the nonlinear shallow water wave equations using radial basis functions, in progress.

[14] Fornberg, B., A Practical Guide to Pseudospectral Methods, Cambridge University Press, Cambridge (1996).

[15] Fornberg, B. and Flyer, N., Accuracy of radial basis function interpolation and derivative approximations on 1-D infinite grids, Advances in Computational Mathematics 23 (2005), 5-20.

[16] Fornberg, B., Flyer, N, Hovde, S. and Piret, C., Localization properties of RBF expansion coefficients for cardinal interpolants. I. Equispaced nodes, to appear in IMA Journal on Numerical Analysis.

[17] Fornberg, B. and Merrill, D., Comparison of finite difference and pseudospectral methods for convective flow over a sphere, Geophys. Res. Lett. 24 (1997), 3245-3248.

[18] Fornberg, B. and Piret, C., A stable algorithm for flat radial basis functions on a sphere, , SIAM J. Sci. Comp. 30 (2007), 60-80.

[19] Fornberg, B. and Piret, C., On choosing a radial basis function and a shape parameter when solving a convective PDE on a sphere, to appear in the J. of Comp. Phys.

[20] Fornberg, B. and Wright, G., Stable computation of multiquadric interpolants for all values of the shape parameter, Comp. Math. with Applications 48 (2004), 853-867.

[21] Fornberg, B. Wright, G. and Larsson, E., Some observations regarding interpolants in the limit of flat radial basis functions, Comp. Math. with Applications 47 (2004), 37-55.

[22] Fornberg, B. and Zuev, J., The Runge phenomenon and spatially variable shape parameters in RBF interpolation, Comp. Math. with Applications 54 (2007), 379-398.

[23] Franke, R., Scattered Data Interpolation: Tests of Some Methods, Math. Comp.,vol. 38, pp. 181-200, 1982.

[24] Freeden, W., Gervens, T. and Schreiner, M., Constructive Approximation on the Sphere with Applications to Geomathematics, Oxford University Press, Oxford (1998).

[25] Hardy, R.L., Multiquadric equations of topography and other irregular surfaces, J. Geophy. Res. 76 (1971), 1905-1915.

[26] Hubbert, S. and Baxter, B., Radial basis functions for the sphere, Progress in Multivariate Approximation, Volume 137 of the International Series of Numerical Mathematics, Birkhauser, (2001) 33-47.

[27] Kansa, E.J., Multiquadrics - A scattered data approximation scheme with applications to computational fluid-dynamics. I. Surface approximations and partial derivative estimates, Comput. Math. Appl. 19 (8/9) (1990), 127-145.

[28] Kansa, E.J., Multiquadrics - A scattered data approximation scheme with applications to computational fluid-dynamics. II. Solutions to parabolic, hyperbolic and elliptic partial differential equations, Comput. Math. Appl. 19 (8/9) (1990), 147-161.

[29] Larsson, E. and Fornberg, B., A numerical study of radial basis function based solution methods for elliptic PDEs, Comp. Math. with Applications 46 (2003), 891-902.

[30] Larsson, E. and Fornberg, B., Theoretical and computational aspects of multivariate interpolation with increasingly flat radial basis functions, Comp. Math. with Applications 49 (2005), 103-130.

[31] Larsson, E and Fornberg, B., A stable algorithm for flat radial basis functions, to be submitted.

[32] Lundberg, John B. and Schutz, Bob E., Recursion formulas of Legendre functions for use with nonsingular geopotential models, Journal of Guidance, Control, and Dynamics (ISSN 0731-5090), vol. 11, Jan.-Feb. 1988, p. 31-38.

[33] McLeod, J.Y. and Baart, M.L., Geometry and interpolation of curves and surfaces, Cambridge University Press, Cambridge (1998).

[34] Micchelli, C. A., Interpolation of scattered data: Distance matrices and conditionally positive definite finctions, Constr. Approx, 2:11-22, 1986.

[35] Mohlenkamp, M. J., A User's Guide to Spherical Harmonics, citeseer.ist.psu.edu/mohlenkamp00users.html

[36] Mohlenkamp, M., A fast transform for spherical harmonics, Journal of Fourier analysis and applications 5 (2/3) (1999), 159-184.

[37] Platte, R. and Driscoll, T.A., Eigenvalue stability of radial basis function discretizations for time-dependent problems, Comp. Math. with Applications 51 (2006), 1251-1268.

[38] Powell, M.J.D., Five Lectures on Radial Basis Functions, Informatics and Mathematical Modelling, Technical University of Denmark, DTU

[39] Schaback, R., Comparisons of radial basis function interpolants, in Multivariate Approximation: from CAGD to Wavelets, K. Jetter and F.I. Utreras (eds.), World Scientific, Singapore (1993), 293-305.

[40] Rokhlin, V. and Tygert, M., Fast algorithms for spherical harmonic expansions, SIAM J. Sci. Comp. 27 (2005), 1903-1928.

[41] Schoenberg I.J., Metric spaces and completely monotone functions, Ann. of Math. 39, No. 4 (1938), 811-841.

[42] Williamson, D.L., Drake, J.B., Hack, J.J., Jakob R. and Swarztrauber, P.N., A Standard Test Set for Numerical Approximations to the Shallow Water Equations in Spherical Geometry with Example Solutions, in Computer Hardware, Advanced

Mathematics and Model Physics, Department of Energy Report DOE/ER-0541T, 41-49. 1992.

[43] Wright, G., Radial Basis Function Interpolation: Numerical and Analytical Developments, Ph.D. thesis, 2003.

[44] Wright, G. and Fornberg, B., Scattered node compact finite difference-type formulas generated from radial basis functions, Journal of Computational Physics 212 (2006), 99-123.

Appendix A

Paper 1 Localization properties of RBF expansion coefficients for cardinal interpolants

IMA Journal of Numerical Analysis (2007) Page 1 of 25
doi: 10.1093/imanum/dri017

Locality properties of radial basis function expansion coefficients for equispaced interpolation

BENGT FORNBERG
Department of Applied Mathematics, University of Colorado
Boulder, CO 80309, USA (fornberg@colorado.edu)

NATASHA FLYER
Institute for Mathematics Applied to the Geosciences, National Center for Atmospheric Research
Boulder, CO 80307, USA (flyer@ucar.edu)

SUSAN HOVDE AND CÉCILE PIRET
Same address as first author, (hovde@colorado.edu), (piret@colorado.edu)

[Submitted on 14 September 2006; Revised April 25 2007]

Many types of radial basis functions (RBFs) are global, in terms of having large magnitude across the entire domain. Yet, in contrast, for example, with expansions in orthogonal polynomials, RBF expansions exhibit a strong property of locality with regard to their coefficients. That is, changing a single data value mainly affects the coefficients of the RBFs which are centered in the immediate vicinity of that data location. This locality feature can be advantageous in the development of fast and well conditioned iterative RBF algorithms. With this motivation, we employ here both analytical and numerical techniques to derive the decay rates of the expansion coefficients for cardinal data, in both 1-D and 2-D. Furthermore, we explore how these rates vary in the interesting high-accuracy limit of increasingly flat RBFs.

Keywords: Radial basis functions, RBF, cardinal interpolation

1. Introduction

Radial basis functions (RBF) provide a well established approach to the task of interpolating scattered data in multiple dimensions. With a *radial function* $\phi(r)$ and with data values f_k given at locations $\underline{x}_k$, $k = 1, 2, \ldots, n$, the function

$$s(\underline{x}) = \sum_{k=1}^{n} \lambda_k \, \phi(||\underline{x} - \underline{x}_k||), \tag{1.1}$$

where $\|\cdot\|$ denotes the standard Euclidean norm, interpolates the data if we choose the expansion coefficients λ_k in such a way that $s(\underline{x}_k) = f_k$, $k = 1, 2, \ldots, n$. During the last decade, it has become increasingly well recognized that interpolants of this form – when $\phi(r)$ is infinitely differentiable – provide a natural generalization, to arbitrary geometries, of pseudospectral (PS) methods (Driscoll & Fornberg (2002), Fornberg (1996), Fornberg et al. (2004)) for solving PDEs. These differentiable RBFs can be scaled by means of a *shape parameter*, in this paper denoted by ε, so that we frequently write $\phi(r;\varepsilon)$. It turns out that *every* classical PS method (Fourier, Chebyshev, etc.) arises as a special case of RBF interpolation Driscoll & Fornberg (2002), Fornberg et al. (2004) in the limit as $\phi(r;\varepsilon)$ becomes flat (i.e. as $\varepsilon \to 0$).

Successive basis functions in classical basis sets (such as Fourier and Chebyshev sets) are global

and increasingly oscillatory. Altering a single data value will change all expansion coefficients by roughly the same amount - i.e. there is no concept of 'locality' in the resulting expansion. The RBF basis is fundamentally different in a number of ways. In return for giving up the orthogonality of the basis functions, unconditional non-singularity is gained with scattered node locations for many cases of radial functions $\phi(r)$. Although the basis functions typically are global (e.g. the popular choice of $\phi(r) = \sqrt{1+(\varepsilon r)^2}$), the interpolant will nevertheless feature strong locality in the sense that changing the data at one point will mainly influence expansion coefficients of basis functions centered in its immediate vicinity. If the locality was perfect (only one coefficient being affected), the linear system to solve would be diagonal, i.e. perfectly conditioned. Since lack of locality can cause ill-conditioning, a study of locality will give insights into how different radial functions compare in this regard. The degree of locality enters also in the convergence rates of some iterative procedures for rapid computation of the expansion coefficients (Buhmann (2003) Chapter 7, Faul & Powell (2000)).

The concept of locality associated with RBF interpolation on equispaced lattices was first addressed by Buhmann (Buhmann (1988), Buhmann (1993), Buhmann & Powell (1990)), who studied the behavior of the RBF interpolant to cardinal data (a single data value being one and all others equal to zero) in the asymptotic limit as $||\underline{x}|| \to \infty$ along a coordinate axis. While our analysis also considers cardinal data, we instead concentrate on studying the behavior of the resulting RBF expansion coefficients, λ_k, for increasing $|k|$. It should be noted that there is a striking similarity between the integrals that describe the coefficients and those that represent the interpolant for cardinal data. This similarity is discussed and developed further in the context of exploring Gibbs phenomena for RBFs Fornberg & Flyer (in press). In cases where closed form expressions for the integrals that represent the coefficients are not possible (which is the usual circumstance), we present an asymptotic approach using contour integration that captures the behavior of λ_k for both small and large k, noting very different trends in each case. It is the former case (k small) that almost always determines the localization property of the RBF expansion (thin plate splines being the exception). Also not previously observed in the literature is that the decay rate of λ_k for 2-D interpolation is dependent not only on radial distance but also on the angle in coefficient space (and likewise in higher dimensions). In addition, our study also illuminates the dependence of the decay rate on the shape parameter ε for infinitely smooth RBFs.

RBFs are mainly of interest when the data locations are scattered. Since effective theoretical analysis for such cases does not appear to be practical, this study is focused on cases with node points on equispaced lattices (in one and more dimensions). In a follow-up studies, we will consider scattered nodes, in particular when distributed over the surface of a sphere. Preliminary numerical results show trends which qualitatively match those observed in the current paper.

The paper is organized as follows. Section 2 focuses on closed-form expressions for the RBF expansion coefficients in one or more dimensions using Fourier analysis. Explicit formulas are obtained for a few RBF cases, exhibiting a variety of decay behaviors for the expansion coefficients. However, such explicit expressions are rare even in 1-D, making it necessary to obtain asymptotic estimates. It is shown in Section 3 how contour integration offers a particularly effective way to estimate the size of the cardinal expansion coefficients in 1-D for both small and large k. These observations are summarized in Section 4, with a discussion of the situation in higher dimensions given in Section 5. Section 6, with a summary of observations, is followed by Appendix A proving non-singularity of a less commonly used type of radial function. Appendix B presents the asymptotic analysis for the generalized multiquadric RBF.

2. Closed form expressions for cardinal coefficients

2.1 *Basic formulas*

We consider first the situation in 1-D and base the analysis in this section on the assumption of a constant node spacing $h = 1$. The radial function $\phi(r)$ takes, at the lattice points $x_k = k \in Z$, the values $\phi(k)$. The cardinal expansion coefficients $\lambda_k,\ k \in Z$, will then satisfy

$$\sum_{k=-\infty}^{\infty} \lambda_k\, \phi(n-k) = \begin{cases} 1 & n = 0 \\ 0 & n \neq 0,\ n \in Z \end{cases} . \tag{2.1}$$

In terms of the 2π-periodic functions

$$\Lambda(\xi) = \sum_{k=-\infty}^{\infty} \lambda_k\, e^{ik\xi}$$

and

$$\Xi(\xi) = \sum_{k=-\infty}^{\infty} \phi(k)\, e^{ik\xi},$$

the convolution in (2.1) can be expressed as

$$\Lambda(\xi) \cdot \Xi(\xi) = 1.$$

We adhere to the convention of defining the Fourier transform through the relations $f(x) = \frac{1}{\sqrt{2\pi}} \int_{-\infty}^{\infty} \widehat{f}(\omega)\, e^{i\omega x} d\omega$, $\widehat{f}(\omega) = \frac{1}{\sqrt{2\pi}} \int_{-\infty}^{\infty} f(x)\, e^{-i\omega x} dx$. Furthermore, radial functions are symmetric, i.e. $\phi(r) = \phi(-r)$ implying $\lambda_k = \lambda_{-k}$. It follows then from the Poisson summation formula that

$$\Xi(\xi) = \sqrt{2\pi} \sum_{k=-\infty}^{\infty} \widehat{\phi}(\xi + 2\pi k), \tag{2.2}$$

and we obtain the cardinal expansion coefficients explicitly (as has been observed earlier, e.g. Buhmann & Powell (1990), Buhmann (2003)) as

$$\lambda_k = \frac{1}{(2\pi)^{3/2}} \int_0^{2\pi} \frac{e^{ik\xi}}{\sum\limits_{j=-\infty}^{\infty} \widehat{\phi}(|\xi + 2\pi j|)} d\xi. \tag{2.3}$$

In cases where the regular Fourier transform for $\phi(r)$ fails to exist, the generalized Fourier transform can be used (e.g. Arsac (1966), Jones (1966), Lighthill (1958)).

We can note that the expression for the interpolant becomes

$$s(x) = \frac{1}{2\pi} \int_{-\infty}^{\infty} \frac{\widehat{\phi}(\xi) e^{ix\xi}}{\sum\limits_{j=-\infty}^{\infty} \widehat{\phi}(|\xi + 2\pi j|)} d\xi. \tag{2.4}$$

This differs from (2.3) mainly in two ways: 1) the factor of $\widehat{\phi}(\xi)$ in the numerator and 2) the integral is taken over $(-\infty, \infty)$. As a result, there is a close relationship between the expansion coefficients, λ_k, and the interpolant, $s(x)$. Fuller exploration of this relationship will be postponed to a follow-up paper, as it would distract from our current theme.

For cardinal expansions in n-D, (2.3) generalizes to

$$\lambda_{k_1,\ldots,k_n} = \frac{1}{(2\pi)^{(3n)/2}} \int_0^{2\pi} \cdots \int_0^{2\pi} \frac{e^{i\underline{k}\cdot\underline{\xi}}}{\sum\limits_{j_1=-\infty}^{\infty} \cdots \sum\limits_{j_n=-\infty}^{\infty} \widehat{\phi}(\|\underline{\xi}+2\pi\underline{j}\|)} d\underline{\xi}. \tag{2.5}$$

Table 1 lists some examples of radial functions $\phi(r)$ and their (generalized) Fourier transforms. Non-singularity of the RBF interpolant in the SH case (for scattered data in n dimensions) was first shown in Gneiting (1997). A new shorter proof is furnished in Appendix A.

The multidimensional Fourier transforms in Table 1 are most easily carried out by means of the Hankel relation

$$\begin{aligned} \widehat{\phi}(\|\underline{\xi}\|) &= (2\pi)^{-n/2} \int_{-\infty}^{\infty} \cdots \int_{-\infty}^{\infty} \phi(\|\underline{x}\|)\, e^{-i\underline{\xi}\cdot\underline{x}} d\underline{x} \\ &= \frac{1}{\rho^{(n-2)/2}} \int_0^{\infty} \phi(r)\, r^{n/2}\, J_{(n-2)/2}(r\rho) dr, \end{aligned} \tag{2.6}$$

where $\rho^2 = \xi_1^2 + \xi_2^2 + \ldots + \xi_n^2$ and $r^2 = x_1^2 + x_2^2 + \ldots + x_n^2$.

With the use of some Bessel function identities, (2.6) can alternatively be expressed as follows:
$n = 2m+1$ odd:

$$\widehat{\phi}(\rho) = (-2)^m \sqrt{\frac{2}{\pi}} \frac{d^m}{d(\rho^2)^m} \int_0^{\infty} \phi(r) \cos(\rho r) dr \tag{2.7}$$

$n = 2m+2$ even:

$$\widehat{\phi}(\rho) = (-2)^m \frac{d^m}{d(\rho^2)^m} \int_0^{\infty} \phi(r)\, r\, J_0(\rho r) dr. \tag{2.8}$$

2.2 *Some 1-D special cases with simple explicit formulas*

In rare cases, both the infinite sum and the integral in (2.3) can be obtained in closed form. However, these examples are exceptions rather than the rule. They highlight the need for a more general approach that can provide approximations on how the coefficients decay away from $k = 0$ as $|k|$ increases for arbitrary radial functions.

2.2.1 *Cubics* For cubics $\phi(r) = |r|^3$, we obtain (as was noted in Fornberg et al. (2002))

$$\lambda_0 = -4 + 3\sqrt{3}, \;\; \lambda_1 = \frac{19}{2} - 6\sqrt{3} \;\text{ and }\; \lambda_k = \frac{(-1)^k 3\sqrt{3}}{(2+\sqrt{3})^k},\; k \geqslant 2. \tag{2.9}$$

(recalling that $\lambda_{-k} = \lambda_k$).

2.2.2 *IQ* In this case, the sum (but not the integral) can be evaluated in closed form. As was also noted in Fornberg et al. (2002), we then get

$$\lambda_k = \frac{(-1)^k \varepsilon\, \sinh(\frac{\pi}{\varepsilon})}{\pi^2} \int_0^{\pi} \frac{\cos k\xi}{\cosh(\xi/\varepsilon)} d\xi, \;\; k \in Z. \tag{2.10}$$

Type of radial function			**Fourier transform** $\widehat{\phi}(\rho)$ in n-D
Piecewise smooth			
MN	monomial	$\lvert r\rvert^{2j+1}$	$\frac{(-1)^{j+1}2^{2j+\frac{n}{2}+1}(j+\frac{1}{2})\Gamma\left(j+\frac{1}{2}\right)\Gamma\left(j+\frac{n+1}{2}\right)}{\pi}\frac{1}{\lvert\rho\rvert^{2j+n+1}}$
TPS	thin plate spline	$\lvert r\rvert^{2j}\ln\lvert r\rvert$	$(-1)^{j+1}2^{2j+\frac{n}{2}-1}j!\,\Gamma\left(j+\frac{n}{2}\right)\frac{1}{\lvert\rho\rvert^{2j+n}}$
Infinitely smooth			
GMQ	generalized MQ	$(1+(\varepsilon r)^2)^{\beta}$	$\frac{2^{\beta+1}}{\Gamma(-\beta)\varepsilon^{n/2-\beta}}\frac{K_{n/2+\beta}\left(\frac{\lvert\rho\rvert}{\varepsilon}\right)}{\lvert\rho\rvert^{n/2+\beta}}$
	MQ	$\sqrt{1+(\varepsilon r)^2}$	$-\frac{\sqrt{2}}{\sqrt{\pi}\,\varepsilon^{\frac{n-1}{2}}}\frac{K_{\frac{n+1}{2}}\left(\frac{\lvert\rho\rvert}{\varepsilon}\right)}{\lvert\rho\rvert^{\frac{n+1}{2}}}$
	IMQ	$\frac{1}{\sqrt{1+(\varepsilon r)^2}}$	$\frac{\sqrt{2}}{\sqrt{\pi}\,\varepsilon^{\frac{n+1}{2}}}\frac{K_{\frac{n-1}{2}}\left(\frac{\lvert\rho\rvert}{\varepsilon}\right)}{\lvert\rho\rvert^{\frac{n-1}{2}}}$
	IQ	$\frac{1}{1+(\varepsilon r)^2}$	$\frac{1}{\varepsilon^{\frac{n}{2}+1}}\frac{K_{\frac{n}{2}-1}\left(\frac{\lvert\rho\rvert}{\varepsilon}\right)}{\lvert\rho\rvert^{\frac{n}{2}-1}}$
GA	Gaussian	$e^{-(\varepsilon r)^2}$	$\frac{e^{-\rho^2/(4\varepsilon^2)}}{(\sqrt{2}\varepsilon)^n}$
SH	sech	$\operatorname{sech}\varepsilon r$	$\frac{\pi^{\frac{n}{2}}}{(2\rho)^{\frac{n}{2}-1}\varepsilon^{\frac{n}{2}+1}}\sum_{k=0}^{\infty}(-1)^k(2k+1)^{\frac{n}{2}}K_{1-\frac{n}{2}}\left(\frac{\pi\rho}{2\varepsilon}\left(k+\frac{1}{2}\right)\right)$
BSL	Bessel	$\frac{J_{\frac{d}{2}-1}(\varepsilon r)}{(\varepsilon r)^{\frac{d}{2}-1}}$	$\begin{cases}\frac{\left(1-\frac{\lvert\rho\rvert^2}{\varepsilon^2}\right)^{\frac{d-n}{2}-1}}{\varepsilon^n 2^{\frac{d}{2}-1}\Gamma\left(\frac{d-n}{2}\right)\pi^{\frac{n}{2}}}, & \text{if } \lvert\rho\rvert\leqslant\varepsilon\\ 0, & \text{if } \lvert\rho\rvert>\varepsilon\end{cases}$

Table 1. Regular or generalized Fourier transforms for some cases of radial functions

2.2.3 *GA* The exact result can be written as a ratio of two sums

$$\lambda_k = \frac{e^{(\varepsilon k)^2}}{2} \cdot \frac{\sum_{j=k}^{\infty} (-1)^j \, e^{-\varepsilon^2 (j+\frac{1}{2})^2}}{\sum_{j=0}^{\infty} (-1)^j (j+\frac{1}{2}) \, e^{-\varepsilon^2 (j+\frac{1}{2})^2}}, \;\; k \in Z. \tag{2.11}$$

This is most easily verified by substituting (2.11) into (2.1), noting that the denominator in (2.11) does not depend on k, and switching the order in the resulting double sum. A way to arrive at (2.11) (and also (2.12) below) is outlined in Section 3.4.

2.2.4 *SH* The result becomes particularly simple in this case. We find

$$\lambda_k = \frac{1}{\sum_{j=-\infty}^{\infty} (-1)^j \mathrm{sech}^2(\varepsilon j)} (-1)^k \mathrm{sech}(\varepsilon k), \;\; k \in Z. \tag{2.12}$$

In the case that ε is small, the sum can be evaluated very fast by means of either of the identities

$$\begin{aligned} \sum_{j=-\infty}^{\infty} (-1)^j \mathrm{sech}^2(\varepsilon j) &= \frac{4\pi^2}{\varepsilon^2} \sum_{j=0}^{\infty} (j+\tfrac{1}{2}) \mathrm{csch}\left(\tfrac{\pi^2}{\varepsilon} (j+\tfrac{1}{2}) \right) \\ &= \frac{2\pi^2}{\varepsilon^2} \sum_{j=0}^{\infty} \frac{\coth\left(\tfrac{\pi^2}{\varepsilon} (j+\tfrac{1}{2}) \right)}{\sinh\left(\tfrac{\pi^2}{\varepsilon} (j+\tfrac{1}{2}) \right)} \end{aligned}$$

3. Asymptotic analysis in 1-D by means of contour integration

We describe this approach first in the case of MQ and apply then the same methodology to other cases of radial functions.

3.1 *MQ*

The radial function is in this case $\phi(r) = \sqrt{1+(\varepsilon r)^2}$. For algebraic simplicity, we assume $\varepsilon = 1$ (but comment on other choices below). From (2.3) follows

$$\lambda_k = -\frac{1}{4\pi} \int_0^{2\pi} h(\xi) \, e^{ik\xi} d\xi$$

where

$$h(\xi) = \frac{1}{\sum_{j=-\infty}^{\infty} \frac{K_1(|2\pi j + \xi|)}{|2\pi j + \xi|}} \, .$$

The function $h(\xi)$ is 2π-periodic and can, over $[0, 2\pi]$, be written (without taking magnitudes) as

$$h(\xi) = \frac{1}{\sum_{j=0}^{\infty} \frac{K_1(2\pi j + \xi)}{2\pi j + \xi} + \sum_{j=1}^{\infty} \frac{K_1(2\pi j - \xi)}{2\pi j - \xi}}. \tag{3.1}$$

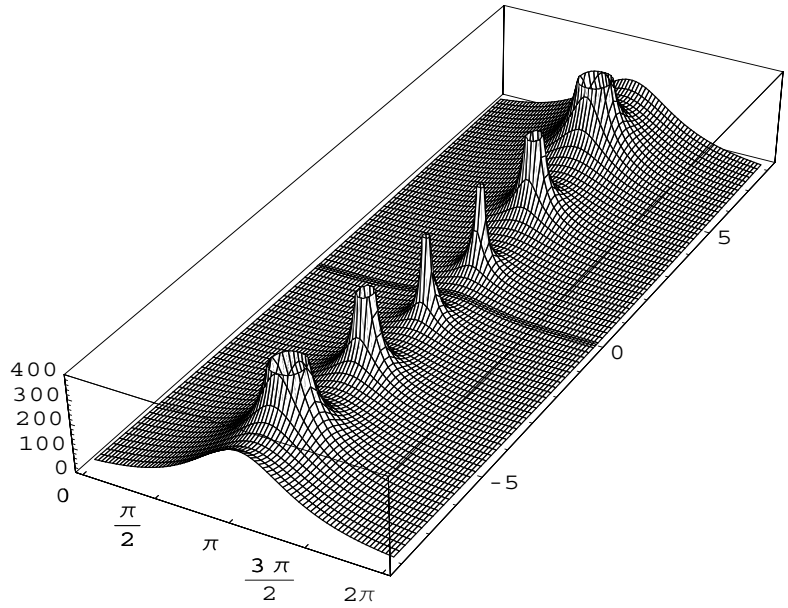

FIG. 1. Magnitude of $h(\xi)$, as given by (3.1), over the domain $0 \leqslant \mathrm{Re}\,\xi \leqslant 2\pi$, $-8 \leqslant \mathrm{Im}\,\xi \leqslant 8$.

In this form, $h(\xi)$ can be extended as a single-valued analytic function throughout the strip $0 \leqslant \mathrm{Re}\,\xi \leqslant 2\pi$. Figure 1 illustrates the magnitude of this function, and Figure 2 shows its schematic character.

We change the integration path, as is indicated in Figure 2, and note that the two leading contributions to the integral as k increases will come from (i) the first pole only and (ii) from the non-cancelling contributions in the vicinity of the branch points at $\xi = 0$ and $\xi = 2\pi$. Each type of singularity contributes a different type of decay behavior to the asymptotic approximation of λ_k for increasing k, as noted below.

- Contribution from the pole singularity

  Along the line $\xi = \pi + i\,t$, the function $h(\xi)$ is purely real and $1/h(\xi)$ features decaying oscillations whose roots mark the pole locations. The first pole appears near $\pi + 1.04\,i$ and has a residue of approximately -34.6, contributing a term of $17.3\,(-1)^{k+1}\,e^{-1.04\,k}$ to λ_k. The second pole at $t \approx 3.42$ would give a contribution of $O(e^{-3.42\,k})$, negligible compared to that of the first pole with further poles giving even smaller contributions.

- Contribution from the branch points

  The singularity of $h(\xi)$ around the origin comes from one term only in the denominator of (3.1), that is $\frac{\xi}{K_1(\xi)} = \xi^2 + (\frac{1}{4} - \frac{\gamma}{2} + \frac{\ln 2}{2} - \frac{\ln \xi}{2})\xi^4 + \ldots$ The branch singularity is of the form $-\frac{1}{2}\xi^4 \ln \xi =$

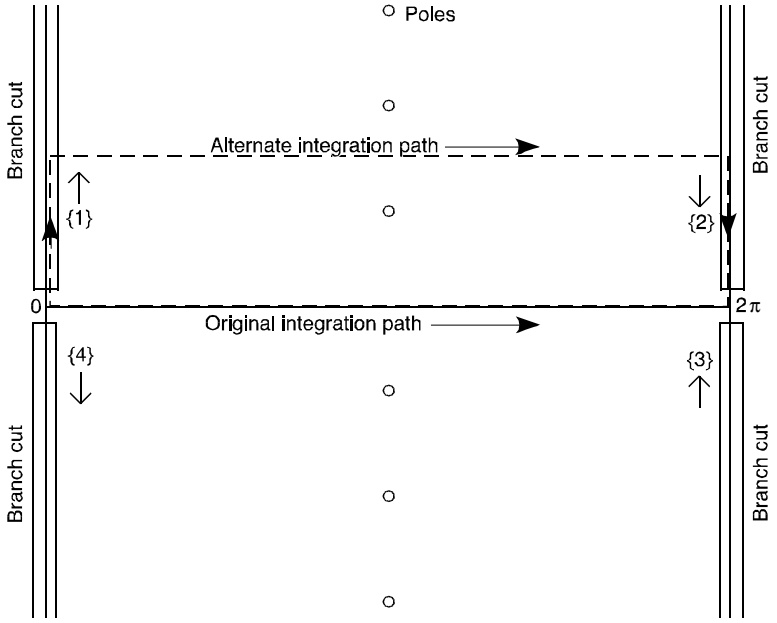

FIG. 2. Character of the function $h(\xi)$ in the complex plane. The original and the modified integration paths are shown. The additional paths marked $\{1\}$, $\{2\}$, $\{3\}$, and $\{4\}$ enter in the discussion in Appendix B.

$-\frac{1}{2}\xi^4(\ln|\xi|+i\arg\xi)$ (and similarly around $\xi=2\pi$). What does not cancel between the two sides but instead adds up (hence an extra factor of 2) amounts to $2(-\frac{1}{4\pi})\int_0^{i\cdot\{\text{some }\delta>0\}}(-\frac{1}{2})\xi^4 i\,\frac{\pi}{2}e^{-ik\xi}\,d\xi$. Letting $\xi=it$ and noting that, as $k\to\infty$, we can change the upper integration limit to infinity, this simplifies to $-\frac{1}{8}\int_0^\infty t^4e^{-kt}dt=-\frac{3}{k^5}$.

Combing these contributions gives the asymptotic approximation to λ_k for increasing k:

$$\lambda_k \quad \approx \underbrace{(-1)^{k+1}\,17.3\,e^{-1.04\,k}+\ldots}_{\text{exponential part}} \quad \underbrace{-\frac{3}{k^5}+\ldots}_{\text{algebraic part}} \tag{3.2}$$

Figure 3 compares, using log-linear and log-log scales, the true values for $|\lambda_k|$ (as calculated with an accurate direct numerical approach) with the 2-term approximation in (3.2). The agreement is seen to be near-perfect. The same procedure can be carried through for any value of the shape parameter ε. Corresponding results for $\varepsilon=0.1$ and in the limit as $\varepsilon\to 0$ are included in Table 2.

We describe next, in more abbreviated form, the remaining cases of smooth radial functions.

3.2 *IQ*

Proceeding in a manner analogous to the MQ case, we find that, for general ε,

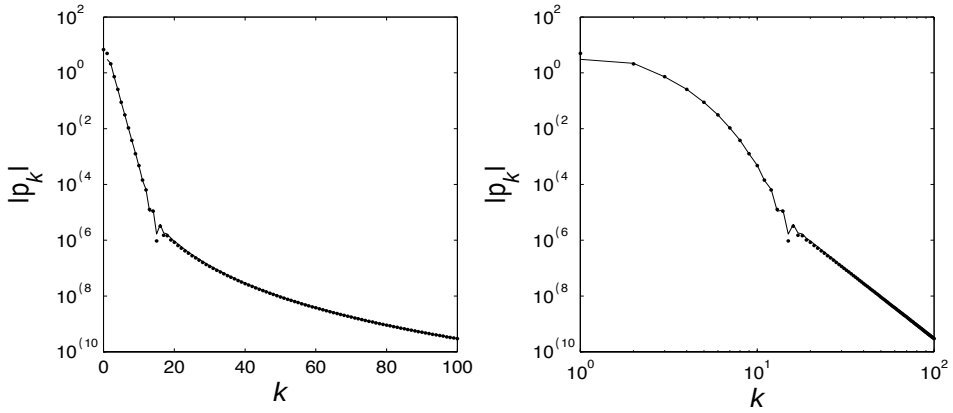

FIG. 3. Comparison between correct values of $|\lambda_k|$ for MQ in 1-D, $\varepsilon = 1$ (dots) and the 2-term asymptotic formula (3.2) (solid line). The subplot to the left is log-linear and the one to the right is log-log.

$$\lambda_k \approx \frac{(-1)^k \varepsilon^2 \sinh(\frac{\pi}{\varepsilon})}{2\pi \cosh(\frac{k\pi\varepsilon}{2})} - \frac{\tanh(\frac{\pi}{\varepsilon})^2}{\pi^2} \frac{1}{k^2}. \tag{3.3}$$

Figure 3.4 compares this approximation with an explicit computation of the λ_k. Panels (a) and (b) depict, respectively, as a function of both k and ε, the exponential and algebraic decay surfaces corresponding to the first and second terms of (3.3). Panel (c) shows the union of these surfaces, which compares favorably with (d), the actual expansion coefficients when computed directly.

3.3 *GMQ*

The generalized multiquadric RBF is $\phi(r) = (1 + (\varepsilon r)^2)^\beta$. Since the analysis is very similar to the MQ case, it is given in Appendix B . Figure 5 shows, for $\varepsilon = 1$, $\log|\lambda_k|$ as a function of β and k. Note the sharp dips in the algebraic decay regime at positive half integer values of β. There are no analogous features in the exponential decay regime. In both regimes the expansion coefficients approach infinity at nonnegative integer values of β.

The exponential decay of the GMQ RBF is given by the single equation (B.2), while a collection of equations, (B.5), (B.6), (B.7), (B.8), and (B.9), is needed to describe the algebraic decay, each equation corresponding to a different set of β values. Positive half-integer values of β are optimal in that they result in logarithmic branch points rather than algebraic, leading to much more rapid decay than achieved by other positive values (Figure 5). Indeed, judging from equation (B.5), it would seem that larger positive half-integer values would be better than smaller ones. However, in practice, to generate an interpolant to a finite number of scattered data points, a linear system is solved in order to determine the expansion coefficients λ_k, and this system becomes markedly more ill-conditioned as β increases, in spite of the enhanced locality. That is, there is a trade-off between locality and conditioning. In this regard, $\beta = \frac{1}{2}$ is a good compromise, consistent with the reputation of the MQ RBF as being particularly useful.

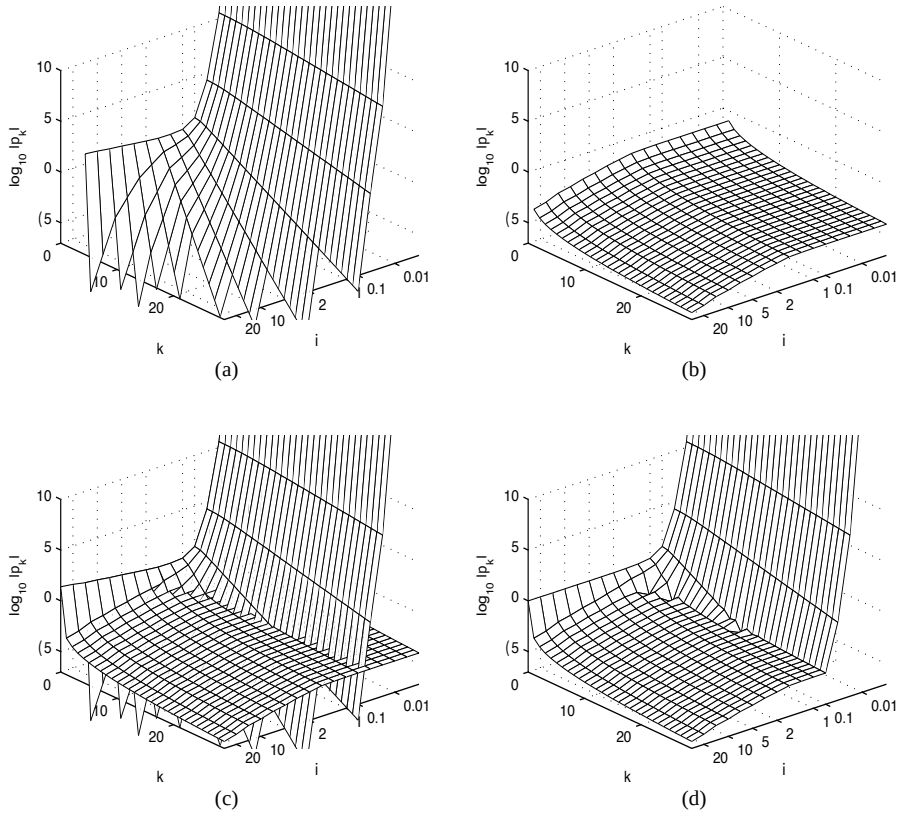

FIG. 4. Comparison of approximate and actual surfaces illustrating the decay of IQ expansion coefficients for 1-D equispaced, cardinal data. (a), the exponential decay (first term of (3.3)). (b), the algebraic decay (second term of (3.3)). (c), combination of (a) and (b). (d), actual expansion coefficients, computed explicitly. Note how well (c) approximates (d).

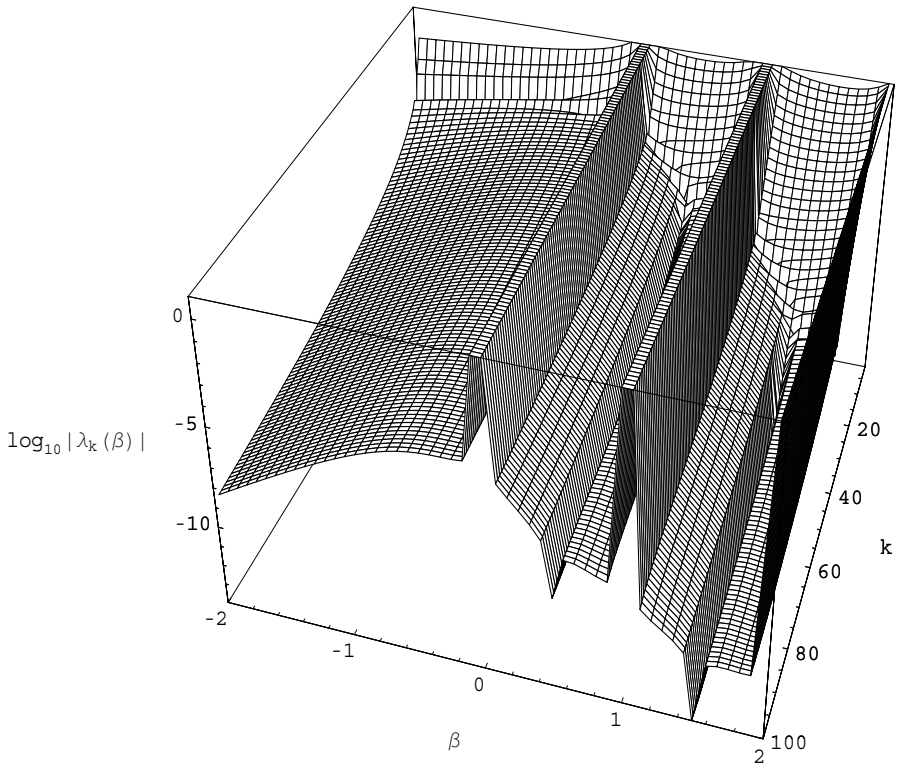

FIG. 5. Plot of log of the absolute expansion coefficients as a function of β and k and unit shape parameter. The values tend to infinity at nonnegative integers and exhibit pronounced dips in the algebraic decay at positive half-integers.

3.4 *GA and SH*

In these cases, there are no branch cuts, and both the locations and residues of the poles of $h(\xi)$ can be written down explicitly. The first pole provides the leading asymptotic term. The steps in arriving at (2.11) and (2.12) include moving the integration path increasingly high up in the complex plane. In the case of (2.11), the result can be further simplified by means of the relation

$$\xi(x) = \frac{1}{x^{3/2}}\,\xi(\frac{1}{x}). \tag{3.4}$$

for the function

$$\xi(x) = \sum_{j=0}^{\infty}(-1)^j(j+\tfrac{1}{2})\,e^{-\pi(j+\frac{1}{2})^2 x}. \tag{3.5}$$

3.5 *BSL*

The oscillatory Bessel RBF, $\phi(r) = J_{\frac{d}{2}-1}(\varepsilon r)/(\varepsilon r)^{\frac{d}{2}-1}$, gives non-singular interpolants if $d \geqslant n$, where d is an integer and n is the dimension of the space Fornberg et al. (2006). These are included in this study mainly to illustrate the unusual locality properties of their expansion coefficients λ_k. The BSL RBFs are different from other RBFs in that their Fourier transforms have compact support, being non-zero only on the interval $[-\varepsilon,\varepsilon]$ in 1-D (see Flyer (2006)). This implies that for $\varepsilon < \pi$, the Poisson sum $\Xi(\xi)$ in equation (2.2) will be zero over a portion of the interval $[-\pi,\pi]$, resulting in a divergent integral for λ_k in (2.3). In such a case the coefficients λ_k become extremely large and essentially lack locality (as seen in the top left diagram of Figure 6).

On the other hand, if $\varepsilon > \pi$ the Poisson sum (2.2) is everywhere positive. Equation (2.3) applies and the coefficients λ_k exhibit locality. For these values of ε, $\Xi(\xi)$ (and therefore $1/\Xi(\xi)$) will always have two discontinuities in some derivative on the interval $[-\pi,\pi]$ due to the character of the Fourier transform and the 2π periodicity of the Poisson sum. This will lead to an algebraic decay rate for λ_k of the type $O(1/k^{(d-1)/2})$. The preceding schematic discussion is illustrated in Figure 6.

4. Summary of asymptotic observations in 1-D

The general picture that has emerged is that, for the main types of radial functions considered here, there is always an exponential decay for the leading coefficients. In the RBF cases for which $h(\xi)$ has branch points at $\xi = 0$ and $\xi = 2\pi$ (which also includes TPS), there will also be algebraic terms, which then will come to dominate for high values of k. Table 2 summarizes the different rates that arise for the types of radial functions introduced in Table 1.

The algebraic trend, if present at all, is noticeable only after the coefficients have decreased by several orders of magnitude. Furthermore, for decreasing ε, it gets progressively more insignificant in view of the rapid growth of the coefficient for the leading exponential term. From a computational point of view, the rapid growth of all the coefficients poses less of a problem than one might fear. Because of the nature of floating point arithmetic, uniform scalings will not generally lead to any loss of computational accuracy. The exponential rate for MN and TPS becomes less favorable when j increases. This forces for these radial functions a trade-off with accuracy, which generally gets better with increasing j.

The cases when $\phi(r)$ is an entire function (GA and BSL) become particularly bad when $\varepsilon \to 0$. For GA, the decay is of the form $O(e^{-\varepsilon^2 k})$ as opposed to $O(e^{-const\cdot\,\varepsilon k})$, and it is essentially lost altogether for BSL when $\varepsilon < \pi$.

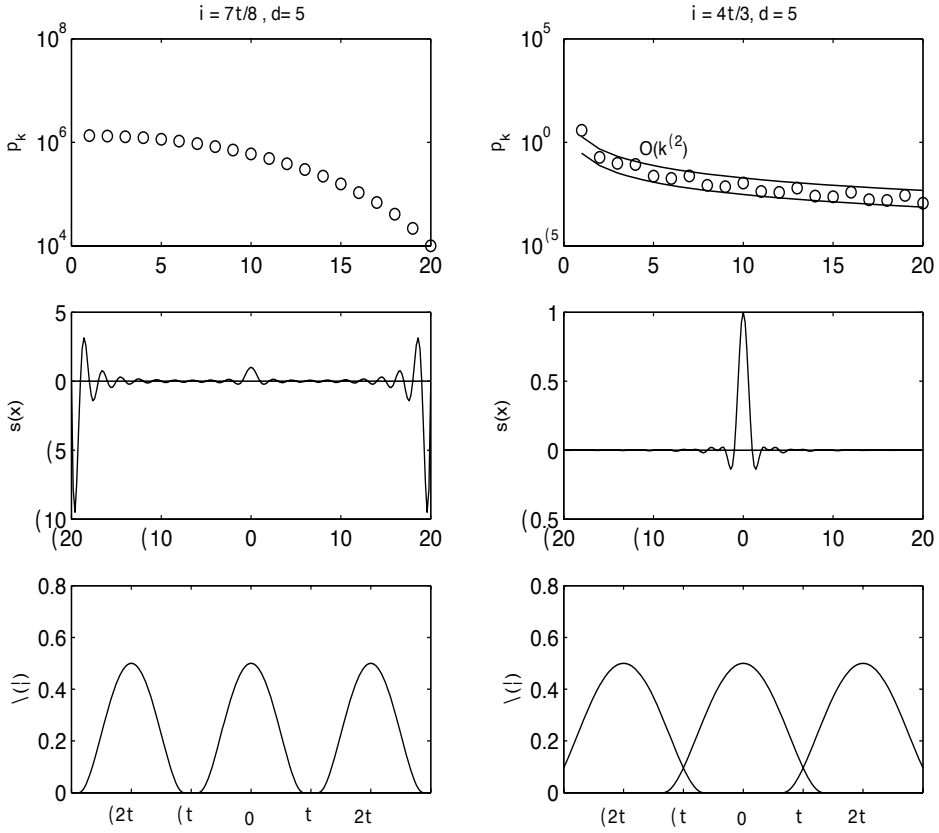

FIG. 6. First row: decay of λ_k. Notice the difference in vertical scale between the left and right figures. Second row: the interpolant $s(x)$. Third row: the $j = 0, \pm$ terms of the Poisson sum for the indicated value of ε and d. Left column: $\varepsilon = \frac{7}{8}\pi < \pi$; right column: $\varepsilon = \frac{4}{3}\pi > \pi$.

Type of radial function		Exponential rate	Algebraic rate
Piecewise smooth			
MN	$j=1$	$(-1)^k\,5.20\,e^{-1.32k}$	N/A
	$j=2$	$(-1)^{k+1}\,1.38\,e^{-0.843k}$	N/A
	$j=3$	$(-1)^k\,0.224\,e^{-0.625k}$	N/A
	$j=4$	$(-1)^{k+1}\,0.0235\,e^{-0.498k}$	N/A
TPS	$j=1$	$(-1)^k\,5.30\,e^{-1.81k}$	$\frac{3}{\pi^2k^4}$
	$j=2$	$(-1)^{k+1}\,1.81\,e^{-1.02k}$	$\frac{5}{\pi^2k^6}$
	$j=3$	$(-1)^k\,0.377\,e^{-0.717k}$	$\frac{7}{\pi^2k^8}$
	$j=4$	$(-1)^{k+1}\,0.0486\,e^{-0.554k}$	$\frac{9}{\pi^2k^{10}}$
Infinitely smooth			
MQ	$\varepsilon=1$	$(-1)^{k+1}\,17.3\,e^{-1.04k}$	$-\frac{3}{k^5}$
	$\varepsilon=\frac{1}{10}$	$(-1)^{k+1}\,1.46\times10^{13}\,e^{-0.150k}$	$-\frac{3000}{k^5}$
	$\varepsilon\to0$	$(-1)^{k+1}\,\frac{\pi\sqrt{\varepsilon}}{2^{3/2}}\,e^{\frac{\pi}{\varepsilon}}\,e^{-\frac{\pi}{2}\varepsilon k}$	$-\frac{3}{\varepsilon^3k^5}$
IQ	$\varepsilon=1$	$(-1)^{k+1}\,3.68\,e^{-1.57k}$	$-\frac{1}{\pi^2k^2}$
	$\varepsilon\to0$	$(-1)^{k+1}\,\frac{\varepsilon^2}{2\pi}\,e^{\frac{\pi}{\varepsilon}}\,e^{-\frac{\pi}{2}\varepsilon k}$	$-\frac{1}{\pi^2k^2}$
IMQ	$\varepsilon=1$	$(-1)^{k+1}7.82e^{-1.38k}$	$\frac{-0.922}{4k(\log k)^2+0.927k\log k+9.92k}$
GA	$\varepsilon^2k>>1$	$(-1)^k\,\frac{\varepsilon^3}{\pi^{3/2}}\,e^{\frac{\pi^2}{4\varepsilon^2}}\,e^{-\varepsilon^2k}$	N/A
SH	$\varepsilon k>>1$	$(-1)^k\,\frac{\varepsilon^2}{2\pi}\,e^{\frac{\pi^2}{2\varepsilon}}\,e^{-\varepsilon k}$	N/A

Table 2. Leading order exponential and algebraic cardinal coefficient decay rates in 1-D for some different radial functions

5. Analysis and observations in 2-D and higher

In the case of GA, we can again find a closed form solution for the cardinal expansion coefficients in any number of dimensions. For the other RBFs, we limit ourselves to 2-D and relate the numerically observed decay rates to characteristics of the 2-D Fourier transform.

5.1 *GA*

With λ_k chosen according to (2.11), it holds that

$$\sum_{k=-\infty}^{\infty} \lambda_k e^{-\varepsilon^2(k-m)^2} = \begin{cases} 1, & \text{if } m = 0; \\ 0, & \text{if } m = 1. \end{cases}$$

Therefore, in n dimensions,

$$\begin{aligned} &\sum_{k_1=\infty}^{\infty} \cdots \sum_{k_n=-\infty}^{\infty} (\lambda_{k_1} \cdot \ldots \cdot \lambda_{k_n}) e^{-\varepsilon^2[(k_1-m_1)^2+\ldots+(k_n-m_n)^2]} \\ &\qquad = \left(\sum_{k_1=-\infty}^{\infty} \lambda_{k_1} e^{-\varepsilon^2(k_1-m_1)^2} \right) \cdot \ldots \cdot \left(\sum_{k_n=-\infty}^{\infty} \lambda_{k_n} e^{-\varepsilon^2(k_n-m_n)^2} \right) \\ &\qquad = \begin{cases} 1, & \text{if } m_1 = m_2 = \cdots = m_n = 0; \\ 0, & \text{otherwise,} \end{cases} \end{aligned}$$

and we have obtained $\lambda_{k_1,k_2,\ldots,k_n} = \lambda_{k_1} \cdot \lambda_{k_2} \cdot \ldots \cdot \lambda_{k_n}$. This is an exact formula for the RBF coefficients in n-D. Notice that they are simply a product of the 1-D coefficients along each of the n dimensions, immediately confirming the pyramid shaped angular dependence seen later on in the GA case of Figure 10. The lack of a simple generalization of Cauchy's Theorem to functions of several complex variables makes the type of analysis we used in 1-D difficult to carry over. However, numerical computation of the cardinal coefficients is again straightforward (noting that the integrals in (2.5) can be rapidly approximated by FFTs).

We will return to the GA RBF in Section 5.3.

5.2 *Cubic RBF*

Figure 7 shows numerically computed values for $\log|\lambda_{k_1,k_2}|$ near the origin in the k_1,k_2-plane.
The coefficients decay exponentially fast for small k, with different rates depending on the direction in the k_1,k_2-plane, as shown in Figure 8.

Each of the subplots in Figure 8 is similar to the 1-D case in the left subplot of Figure 3 in that there are two decay regimes. While we have not been able to find any closed form analytic expressions for the direction dependent exponential decay regime, the algebraic decay regime that dominates for large k, is shown below to be

$$\lambda_{k_1,k_2} \approx -\left(\frac{5}{2\pi}\right)^2 \frac{1}{k^7} \tag{5.1}$$

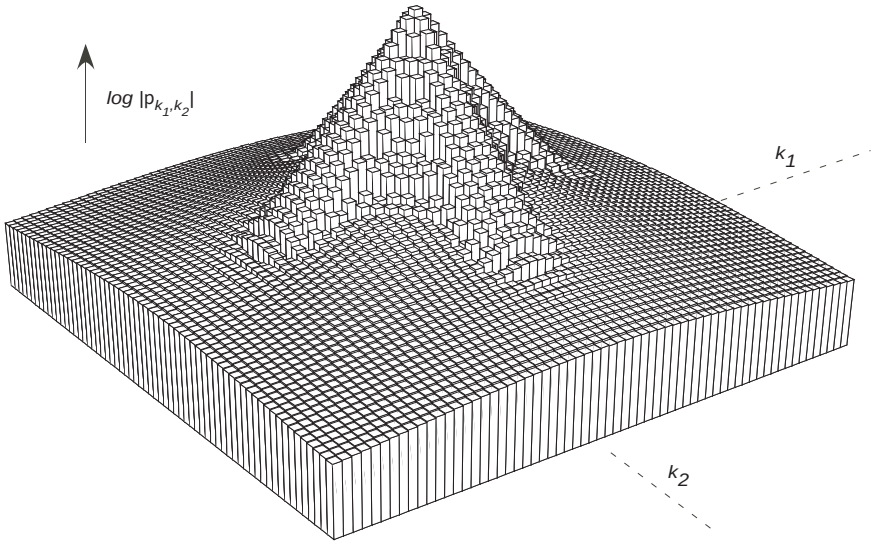

FIG. 7. Display of $\log|\lambda_{k_1,k_2}|$ for cubic RBFs in 2-D centered at $(k_1,k_2)=(0,0)$.

where $k=\sqrt{k_1^2+k_2^2}$. Figure 9 shows the six subplots from Figure 8 superposed on each other, together with (dashed) the curve corresponding to (5.1). The agreement is excellent. A different method of arriving at the algebraic decay rates (by repeated integration-by-parts) is given in Section 4.2.4 of Buhmann (2003).

5.2.1 *Proof of (5.1)* The generalized 2-D Fourier transform for cubics is $\widehat{\phi}(\rho)=\frac{9}{\rho^5}$ (cf. Table 1). The denominator $g(\xi_1,\xi_2)=\sum_{j_1=-\infty}^{\infty}\sum_{j_2=-\infty}^{\infty}\widehat{\phi}(\|\underline{\xi}+2\pi\underline{j}\|)$ in (2.5) will therefore go to infinity in this manner at the origin and at each 2π-periodic repetition of the origin. The function $h(\xi_1,\xi_2)=\frac{1}{g(\xi_1,\xi_2)}$ will, at the origin (and at its periodic repetitions), take the form

$$h(\xi_1,\xi_2)=\frac{1}{9}(\xi_1^2+\xi_2^2)^{5/2}+\ \{\text{a smooth function}\}. \tag{5.2}$$

We note that the cardinal expansion coefficients are proportional to the Fourier series coefficients of the doubly 2π-periodic function $h(\xi_1,\xi_2)$. To see what effect these irregularities have on the coefficient decay rate, we consider also:

Poisson's summation formula in 2-D: If a function $f(\xi_1,\xi_2)$ has the Fourier transform $\widehat{f}(\omega_1,\omega_2)$, then the doubly periodic function

$$\sum_{j_1=-\infty}^{\infty}\sum_{j_2=-\infty}^{\infty} f(\xi_1+2\pi j_1,\xi_2+2\pi j_2)$$

has the Fourier series

$$\frac{1}{2\pi}\sum_{k_1=-\infty}^{\infty}\sum_{k_2=-\infty}^{\infty}\widehat{f}(k_1,k_2)\,e^{i(k_1\xi_1+k_2\xi_2)}.$$

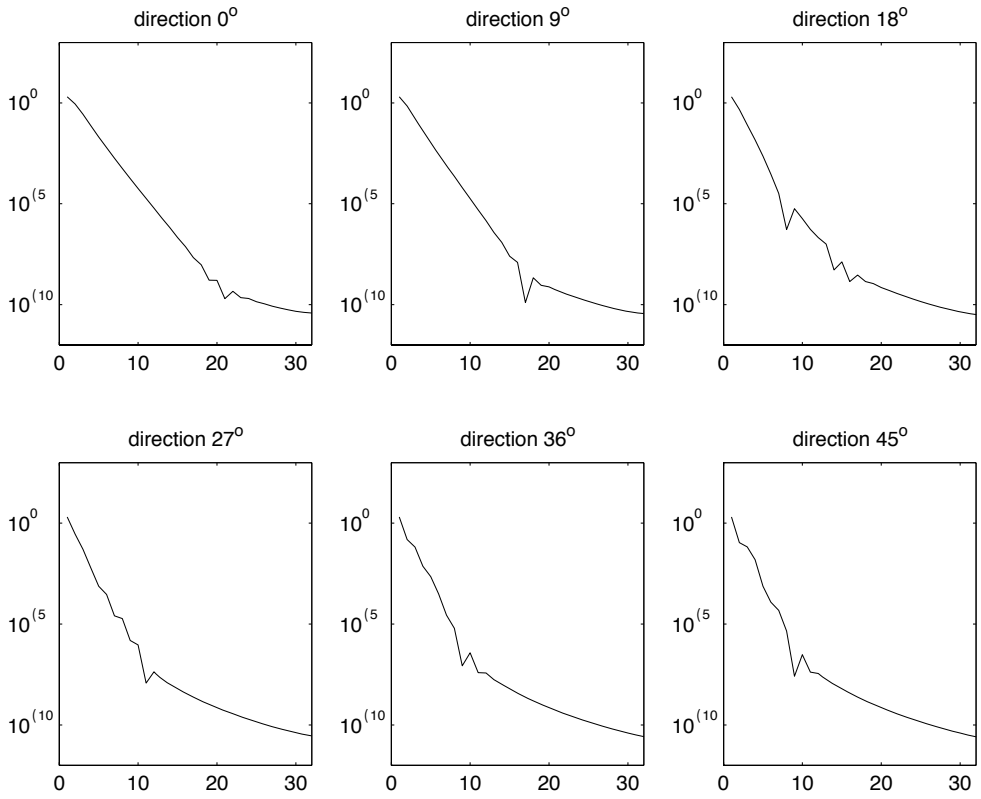

FIG. 8. Log-linear plots of the decay rates of the expansion coefficients in different directions in the k_1, k_2-plane. Vertical direction shows $\log|\lambda_{k_1,k_2}|$, horizontal $\sqrt{k_1^2+k_2^2}$.

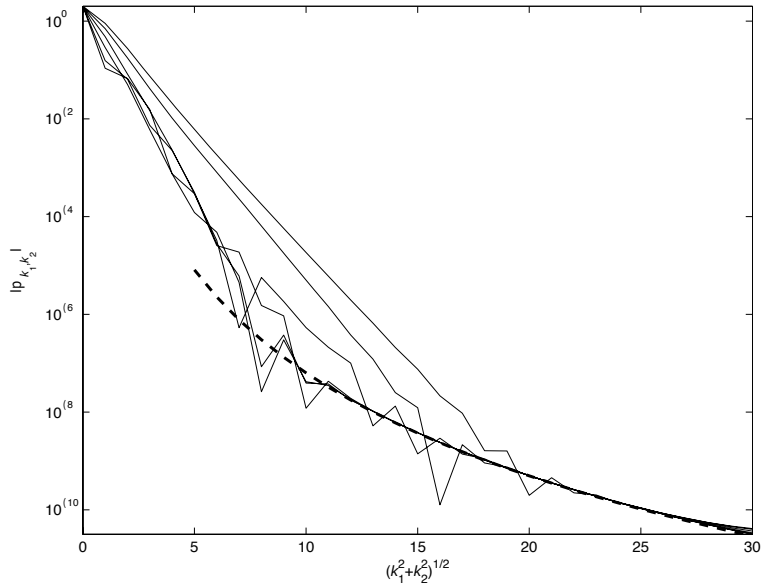

FIG. 9. Decay rates of $|\lambda_{k_1,k_2}|$ in different directions in the k_1,k_2-plane, with the result from (5.1) superimposed as a dashed curve.

To use this result effectively, we first apply the Laplacian operator $\Delta = \frac{\partial^2}{\partial\xi_1^2} + \frac{\partial^2}{\partial\xi_2^2}$ several times (e.g. four times; the exact number does not influence the result) to $h(\xi_1,\xi_2)$, leading to a function which is dominated by the singularities:

$$\Delta^4 h(\xi_1,\xi_2) = 25(\xi_1^2+\xi_2^2)^{-3/2} + \{\text{a smooth function}\}.$$

Its Fourier transform at the integer lattice points, $-25(k_1^2+k_2^2)^{1/2}$, should equal the Fourier coefficients of the function $h(\xi_1,\xi_2)$, with the Laplacian applied four times, i.e. $(k_1^2+k_2^2)^4\lambda_{k_1,k_2}$. This gives (5.1).

5.3 *TPS, GA, AND SH*

In contrast with the situation for the cubic RBF (Section 5.2.1), the functions $g(\xi_1,\xi_2)$ for the TPS, GA, and SH RBFs are infinitely smooth at the origin and at their 2π-periodic repetitions (cf. Table 1). Therefore the decay of the coefficients never becomes algebraic, as can be seen in Figure 10. It should be noted that the type of angular symmetry observed in the GA case is directly due to the grid layout, e.g. a rectalinear (Cartesian) grid layout produces four fold symmetry, a hexagonal grid layout will produce six fold symmetry.

5.4 *MQ, IMQ, and IQ*

The situation in these cases is analogous to that of the cubic RBF since the 2-D generalized Fourier transforms of these RBFs each go to infinity as the origin ($\rho = 0$), but do this in such a way that their inverses are non-smooth across $\rho = 0$ (cf. Table 1). That is, we expect the decay of the coefficients to become algebraic after an initial exponential decay regime. Figure 10 shows that this is indeed the case.

Following a procedure similar to that described in Section 5.2.1, it has been found that the algebraic decay for MQ goes to leading order as $\left(\frac{3}{2\pi}\right)^2 \frac{1}{k^5}$, and for IMQ as $\left(\frac{1}{2\pi}\right)^2 \frac{1}{k^3}$. The decay for IQ is more complicated, involving logarithmic components.

6. Summary of observations for RBF cardinal coefficient decay

Previous literature on the topic has left many questions unanswered: To what extent are the RBF cardinal coefficients, λ_k, localized? If there is a localization attribute to the coefficients, what is the behavior of the coefficients as $|k| = \sqrt{k_1^2 + k_2^2}$ increases from small to large? What happens in higher dimensions? Is the decay rate of λ_k only dependent on radial distances or do angular dependencies come in? In this study, we have addressed these and other questions through both analytical (primarily contour integration in the complex plane) and numerical techniques. In addition, we have also introduced a seldom (if ever) used radial function $\mathrm{sech}(\varepsilon r)$, giving a proof of the non-singularity of its interpolation matrix in n dimensions for scattered data. The observations that have emerged for the RBFs considered in this paper are summarized below.

1. For all RBFs in 1-D and 2-D, except Bessel RBFs (for which the Poisson sum can be zero due to the compactness of its Fourier transform), the leading order behavior of the expansion coefficients for small $|k|$ is exponential decay.

2. However, the leading order behavior of the coefficients can change from exponential decay (as noted in (1)) to algebraic decay as $|k|$ increases, exhibiting two different decay regimes in this limit. In particular, this will occur when $1/\widehat{\phi}(\rho)$ is non-smooth across the origin. Such cases include MN in even dimensions, TPS in odd dimensions, MQ, IMQ, and IQ.

3. For those RBFs that do exhibit two different decay regimes for increasing k and do not grow rapidly far out, which would exclude TPS, the exponential decay behavior of the coefficients for small k determines the localization property of the RBF interpolant. When the leading order behavior becomes algebraically decaying, λ_k has typically decreased by many orders of magnitude (e.g. for MQ in 1-D, with $\varepsilon = 1$, $\lambda_k \approx O(10^{-6})$, contributing less than 1% to the value of the interpolant at the cardinal point.

4. For 2-D, in the regime of exponential decay, (i.e. for small $|k|$, $|k| = \sqrt{k_1^2 + k_2^2}$), the behavior of the coefficients always has an angular dependence in the k_1, k_2 plane. If algebraic decay comes to dominate the leading order behavior as k increases, the dependence will then become purely radial.

It may also be convenient to have available some heuristic guidelines with regard to RBFs in general that allow for quick assessment of the cardinal coefficient decay rate. Hence, we note the following in 1-D:

1. If $\phi(r)$ decays exponentially fast to zero for increasing r (e.g. GA and SH), $\widehat{\phi}(\xi)$ will be analytic in a strip around the ξ-axis, implying that the decay of λ_k will be of exponential form for all k (i.e. will not be overtaken by any slower algebraic rate for large k).

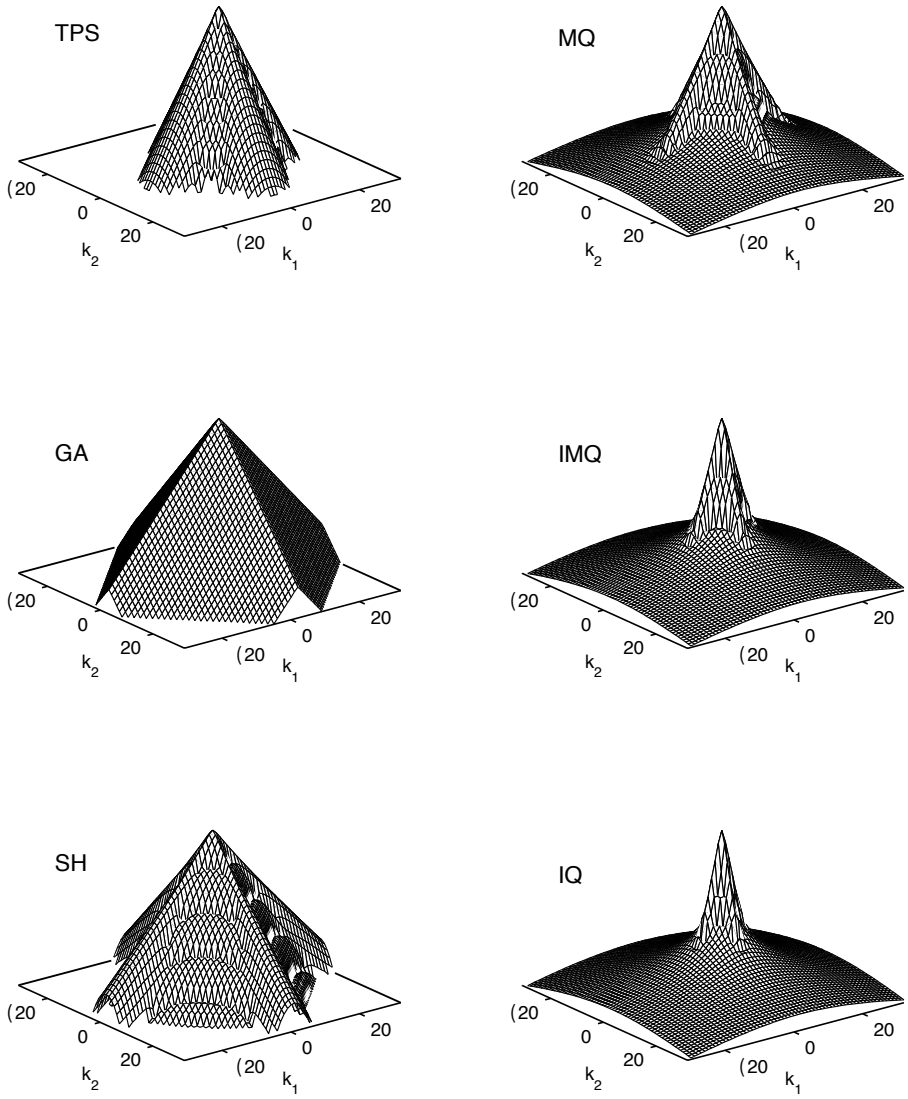

FIG. 10. Decay of expansion coefficients for 2D cardinal data for the TPS, MQ, GA, IMQ, SH, and IQ RBFs displayed in the same log-linear format used in Figure 7. Note that the TPS, GA, and SH RBFs manifest an exponential decay regime only.

2. If $\phi(r)$ is of the form $\phi(r) = |r|^{2j+1}$, $j = 0, 1, \ldots$ (MN, or a linear combination of such), the decay will again be purely exponential.

3. If $\phi(r)$ is analytic and grows for increasing r like $|r|^{\alpha}$ (e.g. GMQ), there will be an algebraic decay rate present, which is particularly small whenever α is an odd positive integer (e.g. MQ).

4. If $\phi(r)$ is analytic in a finite width strip $|\mathrm{Im}\, r| \leqslant a(\varepsilon)$ around the real axis, the exponential part of the decay will typically (e.g. GMQ, SH) be of the form $O\left(e^{-k\pi/(2a(\varepsilon))}\right)$ when $\varepsilon \to 0$.

Acknowledgement The National Center for Atmospheric Research is sponsored by the National Science Foundation. Dr. Bengt Fornberg would like to acknowledge the support of NSF grants DMS-0309803 and DMS-0611681. Dr. Natasha Flyer would like to acknowledge the support of NSF grant ATM-0620100. Ms. Cécile Piret was supported under NSF grant DMS-0309803.

A. Non-singularity of the RBF interpolant (in n dimensions, scattered data) in the SH case ($\phi(r) =$ **sech**(εr))

By the Schoenberg interpolation theorem (Cheney & Light (2000), p. 101), the result follows if we can show that $\mathrm{sech}(\sqrt{x})$ is a completely monotone function. By the Bernstein-Widder theorem (Cheney & Light (2000), p. 95) this will be the case if and only if the inverse Laplace transform $\gamma(s)$ of $\mathrm{sech}(\sqrt{x})$ is non-negative for $0 < s < \infty$. From the expansion $\mathrm{sech}(\sqrt{x}) = 2(e^{-\sqrt{x}} - e^{-3\sqrt{x}} + e^{-5\sqrt{x}} - + \ldots)$ follows

$$\gamma(s) = \frac{1}{\sqrt{\pi} s^{3/2}} \left(e^{-\frac{1}{4s}} - 3e^{-\frac{9}{4s}} + 5e^{-\frac{25}{4s}} - 7e^{-\frac{49}{4s}} + - \ldots \right).$$

This can be written as $\gamma(s) = \frac{1}{\sqrt{\pi} s^{3/2}} \xi\left(\frac{1}{4\pi s}\right)$ using the ξ-function defined in (3.5) It remains only to show that $\xi(s) > 0$ for $0 < s < \infty$. This result is trivial for $s \geqslant 1$ (since the positive terms in (3.5) for $j = 0$ and $j = -1$ then dominate all remaining terms), and it then holds also for $0 < s \leqslant 1$ because of (3.4).

B. Asymptotic analysis for GMQ in 1-D

The generalized multiquadric RBF has the form $\phi(r; \beta, \varepsilon) = (1 + \varepsilon^2 r^2)^{\beta}$. Its Fourier transform is given by

$$\widehat{\phi}(\rho; \beta, \varepsilon) = \frac{2^{\beta+1}}{\Gamma(-\beta)\varepsilon} \left(\frac{K_{\beta+1/2}(\frac{|\rho|}{\varepsilon})}{(\frac{|\rho|}{\varepsilon})^{\beta+\frac{1}{2}}} \right).$$

Note that $\widehat{\phi}$ for nonnegative integer values of β is singular, as also indicated by Figure 5. By equation (2.3),

$$\lambda_k = \frac{\varepsilon \Gamma(-\beta)}{2^{\beta+\frac{5}{2}} \pi^{\frac{3}{2}}} \int_0^{2\pi} \frac{e^{ik\xi} d\xi}{\sum\limits_{j=-\infty}^{\infty} \frac{K_{\beta+1/2}(\frac{|\xi+2\pi j|}{\varepsilon})}{(\frac{|\xi+2\pi j|}{\varepsilon})^{\beta+\frac{1}{2}}}}. \tag{B.1}$$

We find the analog of (3.1) to be

$$h(\xi;\beta,\varepsilon) = \frac{1}{\sum\limits_{j=0}^{\infty} \frac{K_{\beta+1/2}(\frac{2\pi j+\xi}{\varepsilon})}{(\frac{2\pi j+\xi}{\varepsilon})^{\beta+\frac{1}{2}}} + \sum\limits_{j=1}^{\infty} \frac{K_{\beta+1/2}(\frac{2\pi j-\xi}{\varepsilon})}{(\frac{2\pi j-\xi}{\varepsilon})^{\beta+\frac{1}{2}}}}.$$

B.1 *Exponential decay*

The poles of $h(\xi;\beta,\varepsilon)$ are located on the line $\xi = \pi + it$. On this line, the value of $h(\xi;\beta,\varepsilon)$ is purely real. In order to find their contribution to the integral, it is necessary to find the locations of the poles as well as the residues associated with them. Because we are looking for the leading terms, it is sufficient to find the location of the first pole of $h(\xi;\beta,\varepsilon)$ only. We then look for the first zero of $g(\xi;\beta,\varepsilon) = \frac{1}{h(\xi;\beta,\varepsilon)}$ on $\xi = \pi + it$. Due to the rapid decay of the K Bessel function, it is sufficient to use only the center term of the sum in $h(\xi;\beta,\varepsilon)$. For small enough ε, the K Bessel function can be approximated by formula 9.7.2 of Abramowitz & Stegun (1981). For $|\beta| < \frac{5}{2}$ the first two terms are adequate: $K_\nu(z) \approx \sqrt{\frac{\pi}{2z}}\, e^{-z}\left(1 + \frac{4\nu^2-1}{8z}\right)$. We get

$$\begin{aligned} g(\pi+it;\beta,\varepsilon) &\approx \frac{K_{\beta+1/2}(\frac{\pi+it}{\varepsilon})}{(\frac{\pi+it}{\varepsilon})^{\beta+\frac{1}{2}}} \\ &\approx \frac{e^{-\frac{\pi+it}{\varepsilon}}\sqrt{\frac{\pi}{2}}\left(\frac{\pi+it}{\varepsilon}\right)^{-\beta}\varepsilon(2\pi+2it+\beta(1+\beta)\varepsilon)}{2(\pi+it)^2} \end{aligned}$$

The zero of $g(\pi+it;\beta,\varepsilon)$ can therefore be found by solving

$$(\beta+2)\tan^{-1}\left(\frac{t}{\pi}\right) + \frac{t}{\varepsilon} + \tan^{-1}\left(\frac{-2t}{2\pi+\beta(1+\beta)\varepsilon}\right) = \frac{\pi}{2} + \pi\sigma,$$

where σ is an integer. Setting $\sigma = 0$ and approximating $\tan^{-1}(z) \approx z$, we get $t_{pole} \approx \frac{\pi}{2\left(\frac{2+\beta}{\pi} + \frac{1}{\varepsilon} - \frac{2}{2\pi+\beta(1+\beta)\varepsilon}\right)}$.

Therefore, λ_k, for relatively small values of k, can be approximated as

$$\begin{aligned} \lambda_k &\approx \frac{\varepsilon\,\Gamma(-\beta)}{2^{\beta+\frac{5}{2}}\pi^{\frac{3}{2}}}(2\pi i \,\mathrm{Res}(h(z)e^{ikz}, z = \pi + it_{pole})) \\ &= (-1)^{k+1}\frac{\varepsilon\,\Gamma(-\beta)}{2^{\beta+\frac{3}{2}}\sqrt{\pi}}\,\frac{1}{\frac{d}{dt}g(\pi+it)_{t=t_{pole}}}\,e^{-kt_{pole}}. \end{aligned} \tag{B.2}$$

B.2 *Algebraic decay*

We again approximate $h(\xi;\beta,\varepsilon)$ by means of just one term of the Poisson sum:

$$h(\xi;\beta,\varepsilon) \approx f(\xi;\beta,\varepsilon) \equiv \frac{\left(\frac{\xi}{\varepsilon}\right)^{\beta+\frac{1}{2}}}{K_{\beta+\frac{1}{2}}\left(\frac{\xi}{\varepsilon}\right)} \tag{B.3}$$

B.2.1 *Positive β*

β A HALF-INTEGER When $\beta = \mu + 1/2$, with μ a non-negative integer, the leading singularity looks like $\frac{(-1)^{\mu+1}(\frac{\xi}{\varepsilon})^{4\mu+4}\log(\frac{\xi}{\varepsilon})}{(\mu!)^2(\mu+1)!2^{3\mu+1}}$. To compute the contribution of the branch point singularity to the integral in (B.1), we start by noting that $h(\xi;\beta,\varepsilon)$ is purely real along both of the straight lines $\operatorname{Im}\xi = 0$ and $\operatorname{Re}\xi = \pi$. Then, by the Schwarz reflection principle, the contour integral, which should be taken along sections $\{1\}$ and $\{2\}$ in Figure 2 (and also along a connection path high up), can just as well be taken along sections $\{1\}$ and $\{4\}$, leading to a simple treatment of the branch issue. We therefore get

$$\lambda_k \approx \frac{\varepsilon\Gamma(-\mu-1/2)}{(2\pi)^{3/2}2^{\mu+3/2}}\frac{(-1)^{\mu+1}i\pi}{(\mu!)^2(\mu+1)!2^{3\mu+1}}\int_0^{i\infty}\left(\frac{\xi}{\varepsilon}\right)^{4\mu+4}e^{ik\xi}d\xi. \tag{B.4}$$

Setting $\xi = it$ and integrating leads to

$$\lambda_k = \frac{\Gamma(-\beta)(4\beta+2)!}{2^{4\beta+2}\sqrt{\pi}\left((\beta-\frac{1}{2})!\right)^2(\beta+\frac{1}{2})!\,\varepsilon^{4\beta+1}}\;\frac{1}{k^{4\beta+3}}. \tag{B.5}$$

β NOT A HALF-INTEGER In this case the branch point at the origin is algebraic (instead of logarithmic):

$$f(\xi;\beta,\varepsilon) \approx \frac{\xi^{1+2\beta}\cos(\pi\beta)\Gamma(\frac{1}{2}-\beta)}{2^{\beta-\frac{1}{2}}\pi\,\varepsilon^{2\beta+1}}$$

Computing the contour integral along sections $\{1\}$ and $\{4\}$ in Figure 2 leads to

$$\lambda_k \approx \frac{(2\beta+1)\cot(\pi\beta)}{2\pi\,\varepsilon^{2\beta}}\,\frac{1}{k^{2(\beta+1)}} \tag{B.6}$$

B.2.2 *Negative β*

$\beta > -1$ Referring to equation (B.3), we make the approximation that, for small ξ,

$$K_{\frac{1}{2}+\beta}\left(\frac{\xi}{\varepsilon}\right) \approx -\gamma - \log\left(\frac{\xi}{2\varepsilon}\right).$$

This yields

$$f(\xi;\beta,\varepsilon) \approx -\frac{\Gamma(-\beta)\varepsilon^{\frac{1}{2}-\beta}\xi^{\frac{1}{2}+\beta}}{2^{\beta+1}\left[\gamma+\log\left(\frac{\xi}{2\varepsilon}\right)\right]}.$$

Now the equivalent of equation (B.4) will contain logarithms. We make the change of variables $z = \log\xi$ and then apply Laplace's method for integrals with movable maxima as described in Ablowitz & Fokas (2003) and Bender & Orszag (1999). The result is that

$$\lambda_k \approx -\frac{(3+2\beta)\varepsilon^{\frac{1}{2}-\beta}\Gamma(-\beta)\left[\pi\cos\left(\frac{\pi}{4}(1+2\beta)\right)-2\left(\gamma+\log\left(\frac{3+2\beta}{4k\varepsilon}\right)\right)\sin\left(\frac{\pi}{4}(1+2\beta)\right)\right]}{2^{1+\beta}e^{\frac{3}{2}+\beta}\left(\frac{3}{2}+\beta\right)^{-\beta}\pi\left(4\gamma^2+\pi^2+8\gamma\log\left(\frac{3+2\beta}{4k\varepsilon}\right)+4\log^2\left(\frac{3+2\beta}{4k\varepsilon}\right)\right)}\frac{1}{k^{\frac{3}{2}+\beta}}. \tag{B.7}$$

This approximation works well for values of β near $-\frac{1}{2}$. Degradation of the approximation near the ends of the interval $(-1,0)$ is due to the lack of β dependence in the approximation for the Bessel K function. Adding more terms to the Bessel K approximation solves this problem at the cost of a much more complicated expression for λ_k.

$\beta = -1$ In this case we have

$$\widehat{\phi}(\rho;\varepsilon) = \frac{\sqrt{\pi}}{\sqrt{2}\,\varepsilon}\, e^{-\frac{|\rho|}{\varepsilon}}$$

and

$$f(\xi;\varepsilon) = \frac{\sqrt{2}\,\varepsilon}{\sqrt{\pi}} e^{\frac{\rho}{\varepsilon}}.$$

Integrating as before yields

$$\lambda_k \approx -\frac{1}{\pi^2 k^2}. \tag{B.8}$$

Numerical tests have confirmed that the leading algebraic decay does not depend on ε.

$\beta < -1$ We note now that $K_{-\nu}(z) = K_\nu(z)$. Then, when $\beta < 0$, it must be true that $K_{\beta+1/2}(z) = K_{1/2+(-1-\beta)}(z)$. Let $\hat{\beta} = -1-\beta > -1$. Then,

$$\begin{aligned} \frac{(\frac{\xi}{\varepsilon})^{\beta+1/2}}{K_{\beta+1/2}(\frac{\xi}{\varepsilon})} &= \left(\frac{\xi}{\varepsilon}\right)^{1+2\beta} \frac{(\frac{\xi}{\varepsilon})^{\hat{\beta}+1/2}}{K_{\hat{\beta}+1/2}(\frac{\xi}{\varepsilon})} \\ &= \left(\frac{\xi}{\varepsilon}\right)^{1+2\beta} f(\xi;\hat{\beta},\varepsilon) \end{aligned}$$

where $f(\xi;\hat{\beta},\varepsilon)$ is the approximation of $h(\xi;\hat{\beta},\varepsilon)$, defined for $\hat{\beta} = -1-\beta > -1$. Taking the two-term approximation

$$f(\xi;\hat{\beta},\varepsilon) \approx \frac{\cos(\pi\beta)\Gamma(\frac{1}{2}-\hat{\beta})}{2^{3\hat{\beta}+\frac{1}{2}}\pi\,\Gamma(\frac{3}{2}+\hat{\beta})} \left(\frac{\xi}{\varepsilon}\right)^{1+2\hat{\beta}} \left(\left(\frac{\xi}{\varepsilon}\right)^{1+2\hat{\beta}} \Gamma(\tfrac{1}{2}-\hat{\beta}) + 2^{1+2\hat{\beta}}\,\Gamma(\tfrac{3}{2}+\hat{\beta}) \right)$$

and computing the contour integral as before gives

$$\lambda_k \approx \frac{(\cos(\pi\beta)\Gamma(-\beta)\Gamma(\frac{3}{2}+\beta))^2}{\pi^3\,\varepsilon^{-2\beta-2}}\,\frac{1}{k^{-2\beta}}. \tag{B.9}$$

REFERENCES

ABLOWITZ, M.J. & FOKAS, A.S. (2003) *Complex Variables, 2nd Ed.*, Cambridge University Press, Chapter 6.
ABRAMOWITZ, M. & STEGUN, I.A., (1981) *Handbook of Mathematical Functions*, Dover Publications.
ARSAC, J. (1966) *Fourier Transforms and the Theory of Distributions*, Prentice Hall, 1966.

BENDER, C.M. AND ORSZAG, S.A. (1999) *Advanced Mathematical Methods for Scientists and Engineers*, Springer-Verlag, Chapter 6.

BUHMANN, M. D. (1988) *Multivariate interpolation with radial basis functions*, Technical Report DAMPT 1988/NA8, University of Cambridge.

BUHMANN, M. D. (1993) On quasi-interpolation with radial basis functions, *J. Approx. Theo.,* **72**, 103–230.

BUHMANN, M. D. (2003) *Radial Basis Functions*, Cambridge University Press.

BUHMANN, M. D. & POWELL, M.J.D. (1990) Radial basis function interpolation on an infinite regular grid, In: J. C. MASON AND M. G. COX, eds. *Algorithms for Approximation II*, Chapman and Hall, 146–169.

CHENEY, W. & LIGHT, W. (2000) *A Course in Approximation Theory*, Brooks/Cole Publishing Company.

DRISCOLL, T.A. & FORNBERG, B. (2002) Interpolation in the limit of increasingly flat radial basis functions, *Comp. Math. Appl.,* **43**, 413–422.

FAUL, A.C. & POWELL, M. J. D. (2000) Krylov subspace methods for radial function interpolation, In: D. F. GRIFFITHS & G. A. WATSON, eds. *Numerical Analysis 1999*, Chapman and Hall, 115–141.

FLYER, N. (2006) Exact polynomial reproduction for oscillatory radial basis functions on infinite lattices, *Comp. Math. Appl.* **51**, 1199–1208.

FORNBERG, B. (1996) *A Practical Guide to Pseudospectral Methods*, Cambridge University Press, 1996.

FORNBERG, B., DRISCOLL, T.A., WRIGHT, G. AND CHARLES, R.(2002) Observations on the behavior of radial basis functions near boundaries, *Comp. Math. Appl.* **43**, 473–490.

FORNBERG, B. & FLYER, N. The Gibbs Phenomenon for Radial Basis Functions, In: A. JERRI, ed.*The Gibbs Phenomenon in Various Representations and Applications*, Sampling Publishing, Potsdam, NY, in press.

FORNBERG, B., LARSSON, E. AND WRIGHT, G. (2006) A new class of oscillatory radial basis functions, *Comp. Math. Appl.*, 1209–1222.

FORNBERG, B. & WRIGHT, G., Stable computation of multiquadric interpolants for all values of the shape parameter, *Comp. Math. Appl.,* **48**, 853–867.

FORNBERG, B., WRIGHT, G., & LARSSON, E. (2004) Some observations regarding interpolants in the limit of flat radial basis functions, *Comp. Math. Appl.,* **47**, 37–55.

GNEITING, T. (1997) Normal scale mixtures and dual probability densities, *J. Stat. Comp. Simul.,* **59**, 375–384.

JONES, D.S. (1966) *Generalized Functions*, McGraw-Hill.

LIGHTHILL, M.J. (1958) *Fourier Analysis and Generalized Functions*, Cambridge University Press.

Appendix B

Paper 2 A stable algorithm for flat radial basis functions on a sphere

SIAM J. SCI. COMPUT.
Vol. 30, No. 1, pp. 60–80

A STABLE ALGORITHM FOR FLAT RADIAL BASIS FUNCTIONS ON A SPHERE*

BENGT FORNBERG† AND CÉCILE PIRET†

Abstract. When radial basis functions (RBFs) are made increasingly flat, the interpolation error typically decreases steadily until some point when Runge-type oscillations either halt or reverse this trend. Because the most obvious method to calculate an RBF interpolant becomes a numerically unstable algorithm for a stable problem in the case of near-flat basis functions, there will typically also be a separate point at which disastrous ill-conditioning enters. We introduce here a new method, RBF-QR, which entirely eliminates such ill-conditioning, and we apply it in the special case when the data points are distributed over the surface of a sphere. This algorithm works even for thousands of node points, and it allows the RBF shape parameter to be optimized without the limitations imposed by stability concerns. Since interpolation in the flat RBF limit on a sphere is found to coincide with spherical harmonics interpolation, new insights are gained as to why the RBF approach (with nonflat basis functions) often is the more accurate of the two methods.

Key words. radial basis functions, RBF, shape parameter, sphere, spherical harmonics

AMS subject classifications. 65D15, 65F22

DOI. 10.1137/060671991

1. Introduction.

Numerical computations in spherical geometries are ubiquitous in many application areas, such as geophysics (including weather and climate modeling), astrophysics, and quantum mechanics. The apparent simplicity of such geometries can be very deceptive. The impossibility to place more than 20 nodes in a completely uniform pattern on a spherical surface severely complicates most high-order numerical methods, which usually rely on highly regular lattice-type node layouts. Although double Fourier methods [12], [29], [30], [39], spherical harmonics methods [2], [18], [40], [42], and spectral element methods [17], [41], [43] all can achieve spectral accuracy (meaning that errors decay faster than algebraically with an increasing number of node points), all of these approaches suffer from different computational limitations, as noted in [7].

Radial basis functions (RBFs), when used as a basis for spectral methods in general geometries or on curved surfaces, feature a striking algebraic simplicity. They have recently been used very successfully by Flyer and Wright for purely convection-type problems on a spherical surface [7], with an implementation for the shallow water equations forthcoming [8]. However, challenges include numerical conditioning and computational speed. The purpose of the present study is to introduce a new computational algorithm, which successfully addresses the first of these two issues. Our presentation of this RBF-QR algorithm does not imply that we always recommend the use of very flat basis functions. It will depend entirely on the application whether the best value of the shape parameter falls inside or outside the range that was already previously available. What the RBF-QR algorithm achieves is that it makes also the flat basis function range fully available for exploration (and, if appropriate, for

*Received by the editors October 10, 2006; accepted for publication (in revised form) June 21, 2007; published electronically November 7, 2007.
http://www.siam.org/journals/sisc/30-1/67199.html

†University of Colorado, Department of Applied Mathematics, 526 UCB, Boulder, CO 80309 (fornberg@colorado.edu, Cecile.Piret@colorado.edu). The work of the first author was supported by NSF grants DMS-0309803, DMS-0611681, and ATM-0620068. The work of the second author was supported by NSF grants DMS-0309803 and DMS-0611681.

exploitation). For the convection-type test problem just mentioned, this has already been investigated [13].

The essential concept behind the RBF-QR algorithm is that a finite set of near-flat RBFs, although forming a terrible base, nevertheless span an excellent approximation space. The RBF-QR algorithm creates a completely different and very well conditioned base within exactly this same space. Using instead this new base will thus lead to identical results for interpolation, etc., apart from the fact that all ill-conditioning now has been eliminated. In order to carry out this base change in a stable way, the RBFs are first reexpressed as certain truncated infinite sums, after which it transpires that the ill-conditioning can be eliminated *analytically*, before any actual numerics is performed. The latter includes, among other steps, a QR factorization.

This paper starts with a very brief introduction to RBF interpolation, and we then quote some relevant results from the literature, such as the potential significance of the flat basis function limit. The subsequent sections include an introduction to the RBF-QR method, a discussion of computational issues related to it, and numerical test results. The ability to compute stably for all values of the shape parameter leads to novel comparisons between RBFs and spherical harmonics (SPH) interpolations (since the latter are found to arise in the limit of flat RBF). The main observations are summarized in a concluding section.

2. RBF methodology. In order to explain and to motivate the RBF-QR algorithm, we first give a brief introduction to RBFs and then note how they can be used for solving PDEs.

2.1. The form of an RBF interpolant. In the case of interpolating data values f_i at scattered distinct node locations $\underline{x}_i$, $i = 1, 2, \ldots n$, in d dimensions, the basic RBF interpolant takes the form

$$s(\underline{x}) = \sum_{i=1}^{n} \lambda_i \, \phi(\|\underline{x} - \underline{x}_i\|), \tag{2.1}$$

where $||\cdot||$ denotes the Euclidean norm. The expansion coefficients λ_i are determined by the interpolation conditions $s(\underline{x}_i) = f_i$; i.e., they can be obtained by solving a linear system $A\,\underline{\lambda} = \underline{f}$. Written out in more detail:

$$\begin{bmatrix} \phi(\|\underline{x}_1 - \underline{x}_1\|) & \phi(\|\underline{x}_1 - \underline{x}_2\|) & \cdots & \phi(\|\underline{x}_1 - \underline{x}_n\|) \\ \phi(\|\underline{x}_2 - \underline{x}_1\|) & \phi(\|\underline{x}_2 - \underline{x}_2\|) & \cdots & \phi(\|\underline{x}_2 - \underline{x}_n\|) \\ \vdots & \vdots & & \vdots \\ \phi(\|\underline{x}_n - \underline{x}_1\|) & \phi(\|\underline{x}_n - \underline{x}_2\|) & \cdots & \phi(\|\underline{x}_n - \underline{x}_n\|) \end{bmatrix} \begin{bmatrix} \lambda_1 \\ \lambda_2 \\ \vdots \\ \lambda_n \end{bmatrix} = \begin{bmatrix} f_1 \\ f_2 \\ \vdots \\ f_n \end{bmatrix}. \tag{2.2}$$

In this study, we will limit our attention to the radial functions $\phi(r)$ listed in Table 2.1. The parameter ε is known as the *shape parameter*. As $\varepsilon \to 0$, the basis functions become increasingly flat.

On domains with boundaries, polynomial terms are sometimes added to (2.1), together with some constraints on the coefficients [33]. On a spherical surface, the most natural counterpart is to include some low-order SPH [20]. We will not explore such variations here.

2.2. RBFs for interpolation and for solving PDEs. For about two decades following the introduction of RBFs by Hardy in 1971 [19], they were mainly used for multivariate data interpolation in a rapidly expanding range of applications. In 1990,

TABLE 2.1
Definitions of some infinitely differentiable radial functions. The shape parameter ε controls their "flatness."

Name of RBF	Abbreviation	Definition
Multiquadric	MQ	$\sqrt{1+(\varepsilon r)^2}$
Inverse multiquadric	IMQ	$\dfrac{1}{\sqrt{1+(\varepsilon r)^2}}$
Inverse quadratic	IQ	$\dfrac{1}{1+(\varepsilon r)^2}$
Gaussian	GA	$e^{-(\varepsilon r)^2}$

Kansa introduced a meshless collocation method to solve PDEs using RBF interpolants [21], [22]. In this method, a smooth RBF interpolant to the scattered data is differentiated analytically in order to approximate partial derivatives. Kansa used this approach to solve parabolic, elliptic, and viscously damped hyperbolic PDEs. This approach is typically spectrally accurate (when boundary conditions are implemented appropriately). Another notable advantage lies in the fact that it does not require any kind of a mesh, as opposed to the case with most other types of PDE solvers, such as finite difference, finite element, and finite volume methods. Creating a suitable mesh over an irregular domain in several dimensions can be highly challenging.

The flat basis function limit $\varepsilon \to 0$ would appear to be severely ill-conditioned, since all of the basis functions then become constant, and thus linearly dependent. The expansion coefficients λ_i will then diverge to plus or minus infinity, causing large numbers of cancellations to arise both when solving (2.2) and when evaluating (2.1). The first indication that the limit nevertheless could be of some interest arose in connection with analysis of interpolants on infinite equispaced lattices, as summarized in [3, Chapter 4]. However, especially after the apparent ill-conditioning was expressed in 1993 as a fundamental "uncertainty principle" [37], the limit was not considered seriously for numerical use for almost a decade. This started to change in 2002 when Driscoll and Fornberg [6] proved that, in this flat basis function limit, a one-dimensional (1-D) RBF interpolant in general reduces to Lagrange's interpolation polynomial. For extensions of this result to more dimensions, see [26], [38]. Already the 1-D result led to the realization that the complete task, going from data to interpolant, is well-conditioned even though the separate steps of going from data to RBF expansion coefficients and then from RBF expansion coefficients to interpolant both can be ill-conditioned. Interpolation with near-flat RBFs has in much of the RBF literature been mistaken as an ill-conditioned problem partly because the most obvious numerical method then is unstable.

As noted further in [15], and used to great advantage for solving elliptic PDEs in [24], the polynomial limit results imply that the RBF approach for PDEs can be viewed as a generalization (to irregular domains and scattered nodes) of the pseudospectral (PS) method [1], [10], [44].

Another apparent contradiction is the following: Why would we ever consider nearly (or totally) flat basis functions when solving convective-type PDEs, for which the solutions might not be smooth at all—maybe even discontinuous? The RBF-QR algorithm shows that, as $\varepsilon \to 0$, the flat basis functions span exactly the same space as do the (distinctly nonflat, but still very smooth) SPH. We can then draw a parallel to the very successful Fourier-PS methods which, for long-time integration, perform excellently even in cases of nonsmooth solutions ([10, section 4.2]).

Closed form expressions for RBF interpolation and differentiation errors in 1-D periodic settings are given in [11]. The errors for smooth data are found to not only decrease exponentially fast with an increasing number of nodes but also decrease rapidly in this $\varepsilon \to 0$ limit (unless potentially adverse effects due to the Runge phenomenon are present, as discussed in [16]). These observations all agree very well both with theoretical analysis [27], [47] and with computational experience in multidimensional settings with irregular node layouts [24].

The contour-Padé method [14], based on contour integration in a complex ε-plane, confirmed that RBF interpolants $s(\underline{x})$ can be computed in a stable way, using standard precision arithmetic, even in the limit of $\varepsilon \to 0$. Although this algorithm formed a very successful tool for discovering and further exploring several key features of RBF approximations [15], [24], [46], it was limited to a relatively low number of data points ($n \lesssim 200$ in 2-D). This algorithm demonstrated explicitly that there is no fundamental barrier against stable computation in the flat basis function limit. It thus confirmed that use of (2.2) followed by (2.1) can be viewed merely as a potentially ill-conditioned approach for computing something that is intrinsically well-conditioned.

Spherical geometries are of particular interest in many geophysical and astrophysical applications. As noted in the introduction, Flyer and Wright [7] were the first to use RBFs to solve purely convective (i.e., nondissipative) PDEs over a spherical surface. Their implementation followed what we here denote by "RBF-Direct," i.e., direct use of (2.2) followed by (2.1).

The comments above set the context which motivates the present work. We introduce here a new computational algorithm RBF-QR, which, for RBF computations on a sphere, eliminates the ill-conditioning of RBF-Direct for small values of ε (at least for up to several thousands of points). However, it will still depend on the application whether the low ε regime, now made computationally available, is advantageous or not.

3. The RBF-QR method. Compared to the contour-Padé method, the RBF-QR method is faster and algorithmically simpler and it can be used for much larger numbers of points. Although we introduce it here only for the special case of nodes located on the surface of a sphere, it is being developed also for general domains in a parallel research effort [25]. In this present case with nodes on a sphere, we measure all distances that appear in (2.1) and in (2.2) as is customary between points in a 3-D space and not geodesically along great circle arcs.

3.1. The concept of an equivalent basis. The key idea behind the RBF-QR method is to replace, in the case of small ε, the extremely ill-conditioned RBF basis with a well-conditioned one that spans exactly the same space. It turns out to be possible to do this in a way that does not at any stage involve numerical cancellations. The concept of the base change is somewhat reminiscent of how $\{1, x, x^2, \ldots, x^n\}$ forms a very ill-conditioned basis over $[-1, 1]$, whereas the Chebyshev basis $\{T_0(x), T_1(x), T_2(x), \ldots, T_n(x)\}$ is much better conditioned. Since the spaces spanned by the two bases are identical, the results of interpolation using the two bases will also be identical, except for the fact that computations with the latter are vastly more stable with respect to the influence of truncation and rounding errors.

In the present case of RBF-QR applied on the surface of a sphere, the new equivalent bases that we introduce will be seen to converge to the spherical harmonics basis as $\varepsilon \to 0$. We therefore next give a brief introduction to spherical harmonics.

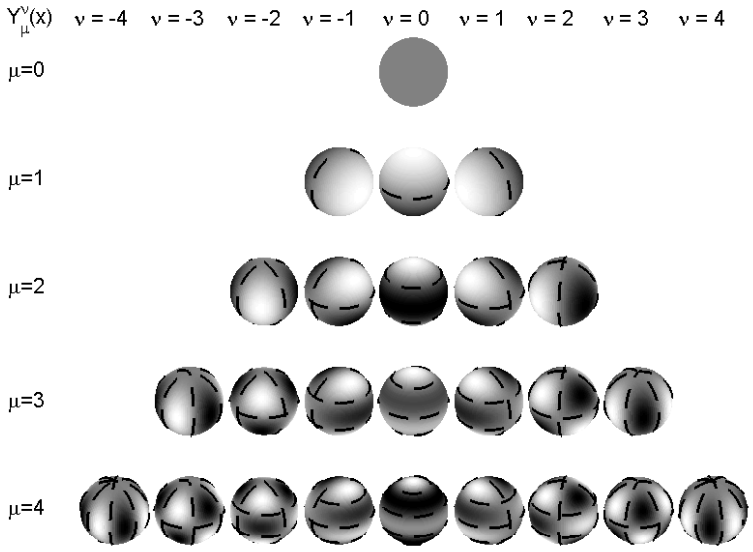

FIG. 3.1. *Spherical harmonics basis functions of the first five orders (cf. the functional forms for the first three orders, given in Table* 3.1*). The shades of gray reflect numerical values; dashed lines mark zero contours.*

3.2. SPH. These functions are the counterparts on the surface of the unit sphere S^2 (defined by $x^2+y^2+z^2 = 1$) to Fourier modes around the periphery of the unit circle S^1 (defined by $x^2 + y^2 = 1$). Although both of these function sets form orthonormal bases, they differ significantly when used numerically, especially when it is needed to switch between spectral coefficients and node values. A Fourier expansion with n coefficients corresponds naturally to node values at n equispaced points. In numerical SPH calculations, it is most common to use in physical space latitude-longitude–type node sets involving about three times as many nodes as there are SPH coefficients and then rely on least squares when transferring data from node values to coefficients. Although no direct counterpart to the FFT algorithm is available, several relatively fast algorithms for large numbers of modes have been proposed, e.g., [5], [31], [32], [34].

Closed form expressions for the SPH basis functions tend to be fairly complicated. The definition that we adhere to here agrees for $(x, y, z) \in S^2$ with

(3.1)
$$Y_\mu^{\ \nu}(x,y,z) = \begin{cases} \sqrt{\frac{2\mu+1}{4\pi}}\sqrt{\frac{(\mu-\nu)!}{(\mu+\nu)!}}P_\mu^\nu(z)\cos(\nu\tan^{-1}(\frac{y}{x})), & \nu = 0,1,\ldots,\mu, \\ \sqrt{\frac{2\mu+1}{4\pi}}\sqrt{\frac{(\mu+\nu)!}{(\mu-\nu)!}}P_\mu^{-\nu}(z)\sin(-\nu\tan^{-1}(\frac{y}{x})), & \nu = -\mu,\ldots,-1. \end{cases}$$

Here $P_\mu^\nu(z)$ are the associated Legendre functions. The functions $Y_\mu^\nu(\underline{x})$ corresponding to $\mu = 0, 1, \ldots, 4$ are illustrated in Figure 3.1.

As indicated in Table 3.1, the SPH can alternatively be viewed as simple polynomials restricted to $(x, y, z) \in S^2$. For each value of μ, the μ^2 SPH of that and lower orders span the space of all independent polynomials in (x, y, z) of degree μ (after the dependence $x^2 + y^2 + z^2 = 1$ has been accounted for).

TABLE 3.1

SPH basis functions of the first few orders, expressed as low degree polynomials in x, y, z, which are then evaluated over the unit sphere $(x, y, z) \in S^2$, i.e., $x^2 + y^2 + z^2 = 1$.

${Y_\mu}^\nu(\underline{x})$	$\nu = -2$	$\nu = -1$	$\nu = 0$	$\nu = 1$	$\nu = 2$
$\mu = 0$			$\frac{1}{2\sqrt{\pi}}$		
$\mu = 1$		$-\frac{1}{2}\sqrt{\frac{3}{2\pi}}y$	$\frac{1}{2}\sqrt{\frac{3}{\pi}}z$	$-\frac{1}{2}\sqrt{\frac{3}{2\pi}}x$	
$\mu = 2$	$\frac{1}{2}\sqrt{\frac{15}{2\pi}}xy$	$-\frac{1}{2}\sqrt{\frac{15}{2\pi}}zy$	$\frac{1}{4}\sqrt{\frac{5}{\pi}}(3z^2-1)$	$-\frac{1}{2}\sqrt{\frac{15}{2\pi}}zx$	$\frac{1}{4}\sqrt{\frac{15}{2\pi}}(x^2-y^2)$

TABLE 3.2

SPH expansion coefficients corresponding to different choices of smooth RBFs.

Radial function	Expansion coefficients $c_{\mu,\varepsilon}$
MQ	$\frac{-2\pi(2\varepsilon^2+1+(\mu+1/2)\sqrt{1+4\varepsilon^2})}{(\mu+3/2)(\mu+1/2)(\mu-1/2)}\left(\frac{2}{1+\sqrt{4\varepsilon^2+1}}\right)^{2\mu+1}$
IMQ	$\frac{4\pi}{(\mu+1/2)}\left(\frac{2}{1+\sqrt{4\varepsilon^2+1}}\right)^{2\mu+1}$
IQ	$\frac{4\ \pi^{3/2}\mu!}{\Gamma(\mu+\frac{3}{2})(1+4\varepsilon^2)^{\mu+1}}\ {}_2F_1(\mu+1,\mu+1;2\mu+2;\frac{4\varepsilon^2}{1+4\varepsilon^2})$
GA	$\frac{4\pi^{3/2}}{\varepsilon^{2\mu+1}}e^{-2\varepsilon^2}I_{\mu+1/2}(2\varepsilon^2)$

A SPH expansion of a function defined over the unit sphere takes the form

$$s(x,y,z) = \sum_{\mu=0}^{\infty}\sum_{\nu=-\mu}^{\mu} c_{\mu,\nu}\ {Y_\mu}^\nu(x,y,z). \tag{3.2}$$

Truncated SPH expansions ($\mu \le \mu_{\max}$) feature a completely uniform resolution over the surface of the sphere. As was noted in the introduction, truncated SPH expansions provide one of the main approaches for reaching spectral accuracy when numerically solving PDEs on a sphere [2], [18], [40], [42]; see especially [7] for a comparison between this and other methodologies (including RBFs).

3.3. Expansion formulas for RBFs in terms of SPH. We next quote some formulas that can be used to transform a basis made up of RBFs to one based on SPH. Hubbert and Baxter [20] give expressions for the coefficients $c_{\mu,\varepsilon}$ in expansions of the form

$$\phi(\|\underline{x}-\underline{x}_i\|) = {\sum_{\mu=0}^{\infty}\sum_{\nu=-\mu}^{\mu}}' \{c_{\mu,\varepsilon}\ \varepsilon^{2\mu}\ {Y_\mu}^\nu(\underline{x}_i)\}\ {Y_\mu}^\nu(\underline{x}), \tag{3.3}$$

where the symbol $\sum'$ implies halving the $\nu = 0$ term of the sum. The results for the radial functions in Table 2.1 are shown in Table 3.2 (including IQ, not given in [20]). A key feature of these formulas is that, even for vanishingly small ε, all coefficients can be calculated without any loss of significant digits caused by numerical cancellations. Below are some notes on these expansions:

- In the formula for IQ, ${}_2F_1(\dots)$ denotes the (Gauss) hypergeometric function.
- In the formula for GA, $I_{\mu+1/2}$ denotes a Bessel function of the second kind. It follows from the identity $\frac{I_{\mu+1/2}(2\varepsilon^2)}{\varepsilon^{2\mu+1}} = \frac{1}{\Gamma(\mu+1)\sqrt{\pi}}\int_{-1}^{1} e^{2\varepsilon^2 t}(1-t^2)^k dt$ that the apparent singularity of $c_{\mu,\varepsilon}$ at $\varepsilon = 0$ is a removable one.

TABLE 3.3
Expansion coefficients for two cases of piecewise smooth radial functions.

Radial function	Definition	Expansion coefficients c_μ
Cubic	$\lvert r\rvert^3$	$\frac{36\pi}{(\mu+\frac{5}{2})(\mu+\frac{3}{2})(\mu+\frac{1}{2})(\mu-\frac{1}{2})(\mu-\frac{3}{2})}$
Thin plate splines (TPS)	$r^2\log\lvert r\rvert$	$\frac{16\pi}{(\mu+2)(\mu+1)\mu(\mu-1)}$

- In practice, we truncate the infinite outer sum in (3.3) after a finite number of terms. This process is explained in more detail in section 3.5.2.
- The shape parameter ε appears in (3.3) both in the factors $\varepsilon^{2\mu}$ and also inside the expansion coefficients $c_{\mu,\varepsilon}$. Because the matrix algebra in the RBF-QR algorithm requires numerical values of $c_{\mu,\varepsilon}$, we need to give a numerical value to ε at the beginning of our algorithm. However, to eliminate any danger of numerical underflow, we wait until the very end to introduce the $\varepsilon^{2\mu}$ factors seen in (3.3) (at which point they can be factored out and discarded).
- Expansions are possible also for piecewise smooth RBFs. The expansions then take the form

$$\phi(\|\underline{x}-\underline{x}_i\|)=\sum_{\mu=0}^{\infty}{\sum_{\nu=-\mu}^{\mu}}'\{c_\mu\ {Y_\mu}^\nu(\underline{x}_i)\}\ {Y_\mu}^\nu(\underline{x}),$$

with some examples of expansion coefficients given in Table 3.3. Since such RBFs do not give spectral accuracy, and also have no ε dependence (and therefore no flat limit), these cases are of less interest in the present context.

3.4. Matrix representation and QR factorization.

3.4.1. Change of basis. Following (3.3), we rewrite the original ill-conditioned basis as expansions in terms of successive SPH as

(3.4)

$$\begin{cases}
\phi(\|\underline{x}-\underline{x}_1\|)= & \frac{c_{0,\varepsilon}}{2}Y_0^0(\underline{x}_1)Y_0^0(\underline{x}) \\
& +\varepsilon^2 c_{1,\varepsilon}\{Y_1^{-1}(\underline{x}_1)Y_1^{-1}(\underline{x})+\frac{1}{2}Y_1^0(\underline{x}_1)Y_1^0(\underline{x})+Y_1^1(\underline{x}_1)Y_1^1(\underline{x})\} \\
& +\varepsilon^4 c_{2,\varepsilon}\{.....\}+\varepsilon^6 c_{3,\varepsilon}\{.....\}+\varepsilon^8 c_{4,\varepsilon}\{.....\}+\cdots, \\
\phi(\|\underline{x}-\underline{x}_2\|)= & \frac{c_{0,\varepsilon}}{2}Y_0^0(\underline{x}_2)Y_0^0(\underline{x}) \\
& +\varepsilon^2 c_{1,\varepsilon}\{Y_1^{-1}(\underline{x}_2)Y_1^{-1}(\underline{x})+\frac{1}{2}Y_1^0(\underline{x}_2)Y_1^0(\underline{x})+Y_1^1(\underline{x}_2)Y_1^1(\underline{x})\} \\
& +\varepsilon^4 c_{2,\varepsilon}\{.....\}+\varepsilon^6 c_{3,\varepsilon}\{.....\}+\varepsilon^8 c_{4,\varepsilon}\{.....\}+\cdots, \\
\vdots & \vdots \\
\phi(\|\underline{x}-\underline{x}_n\|)= & \frac{c_{0,\varepsilon}}{2}Y_0^0(\underline{x}_n)Y_0^0(\underline{x}) \\
& +\varepsilon^2 c_{1,\varepsilon}\{Y_1^{-1}(\underline{x}_n)Y_1^{-1}(\underline{x})+\frac{1}{2}Y_1^0(\underline{x}_n)Y_1^0(\underline{x})+Y_1^1(\underline{x}_n)Y_1^1(\underline{x})\} \\
& +\varepsilon^4 c_{2,\varepsilon}\{.....\}+\varepsilon^6 c_{3,\varepsilon}\{.....\}+\varepsilon^8 c_{4,\varepsilon}\{.....\}+\cdots.
\end{cases}$$

This can be rewritten in matrix×vector form as follows:

$$\begin{bmatrix} \phi(\|\underline{x}-\underline{x}_1\|) \\ \phi(\|\underline{x}-\underline{x}_2\|) \\ \vdots \\ \phi(\|\underline{x}-\underline{x}_n\|) \end{bmatrix}$$

(3.5)

$$= \begin{bmatrix} \frac{c_{0,\varepsilon}}{2}Y_0^0(\underline{x}_1) & \frac{\varepsilon^2 c_{1,\varepsilon}}{1}Y_1^{-1}(\underline{x}_1) & \frac{\varepsilon^2 c_{1,\varepsilon}}{2}Y_1^0(\underline{x}_1) & \frac{\varepsilon^2 c_{1,\varepsilon}}{1}Y_1^1(\underline{x}_1) & \cdots \\ \frac{c_{0,\varepsilon}}{2}Y_0^0(\underline{x}_2) & \frac{\varepsilon^2 c_{1,\varepsilon}}{1}Y_1^{-1}(\underline{x}_2) & \frac{\varepsilon^2 c_{1,\varepsilon}}{2}Y_1^0(\underline{x}_2) & \frac{\varepsilon^2 c_{1,\varepsilon}}{1}Y_1^1(\underline{x}_2) & \cdots \\ \cdots & \cdots & \cdots & \cdots & \cdots \\ \frac{c_{0,\varepsilon}}{2}Y_0^0(\underline{x}_n) & \frac{\varepsilon^2 c_{1,\varepsilon}}{1}Y_1^{-1}(\underline{x}_n) & \frac{\varepsilon^2 c_{1,\varepsilon}}{2}Y_1^0(\underline{x}_n) & \frac{\varepsilon^2 c_{1,\varepsilon}}{1}Y_1^1(\underline{x}_n) & \cdots \end{bmatrix} \begin{bmatrix} Y_0^0(\underline{x}) \\ Y_1^{-1}(\underline{x}) \\ Y_1^0(\underline{x}) \\ Y_1^1(\underline{x}) \\ Y_2^{-2}(\underline{x}) \\ Y_2^{-1}(\underline{x}) \\ Y_2^0(\underline{x}) \\ Y_2^1(\underline{x}) \\ Y_2^2(\underline{x}) \\ \vdots \end{bmatrix}$$

$$= B \cdot Y(\underline{x}).$$

The key observation in what follows is that, if we multiply both sides of (3.5) with any nonsingular matrix from the left, the effect will be that we have formed new linear combinations of existing basis functions; i.e., the space that the functions span has not changed.

A QR factorization of B creates in the upper triangular matrix new linear combinations of the rows of B. In this process, elements in different columns are never combined with each other. Powers of ε will appear in the same pattern in the resulting upper triangular matrix as they did in the B-matrix, and no mixing of large and small elements will occur, no matter the value of ε. We thus factor B into a product $B = Q \cdot E \cdot R$, where Q is unitary, E is diagonal, and R is upper triangular. From the observations above, $B \cdot Y(\underline{x})$ and $R \cdot Y(\underline{x})$ will then span the same space. We will do this factorization in such a way that the ill-conditioning issue becomes entirely confined to the E-matrix and thus has disappeared from the numerical problem when using $R \cdot Y(\underline{x})$ in place of the original basis $B \cdot Y(\underline{x})$. The essential point that makes the RBF-QR algorithm work is that the ill-conditioning of the original base given in the left-hand side of (3.5) and (3.6) has become entirely confined to the E-matrix. This matrix both enters and disappears from the calculation *analytically*; i.e., it never enters into the numerical calculation of the $R \cdot Y(\underline{x})$.

Written in equation form:

$$\begin{bmatrix} \phi(\|\underline{x}-\underline{x}_1\|) \\ \phi(\|\underline{x}-\underline{x}_2\|) \\ \phi(\|\underline{x}-\underline{x}_3\|) \\ \phi(\|\underline{x}-\underline{x}_4\|) \\ \vdots \\ \phi(\|\underline{x}-\underline{x}_n\|) \end{bmatrix} = \begin{bmatrix} & & \\ & Q & \\ & & \end{bmatrix} \begin{bmatrix} 1 & & & & & \\ & \varepsilon^2 & & & & \\ & & \varepsilon^2 & & & \\ & & & \varepsilon^2 & & \\ & & & & \varepsilon^4 & \\ & & & & & \ddots \end{bmatrix}$$

$$
\begin{aligned}
(3.6)\qquad & \times \begin{bmatrix}
* & . & . & . & . & . & . & . & . & . & \cdots \\
 & * & * & * & . & . & . & . & . & . & \cdots \\
 & & * & * & . & . & . & . & . & . & \cdots \\
 & & & * & . & . & . & . & . & . & \cdots \\
 & & & & * & * & * & * & * & . & \cdots \\
 & & & & & * & * & * & * & . & \cdots \\
 & & & & & & \ddots & \cdots & \cdots & . & \cdots
\end{bmatrix}
\begin{bmatrix}
Y_0^0(\underline{x}) \\
Y_1^{-1}(\underline{x}) \\
Y_1^0(\underline{x}) \\
Y_1^1(\underline{x}) \\
Y_2^{-2}(\underline{x}) \\
Y_2^{-1}(\underline{x}) \\
Y_2^0(\underline{x}) \\
Y_2^1(\underline{x}) \\
Y_2^2(\underline{x}) \\
\vdots
\end{bmatrix} \\
& = (Q \cdot E \cdot R) \cdot Y(\underline{x}),
\end{aligned}
$$

where Q is a unitary $n \times n$ matrix, E is a $n \times n$ diagonal matrix, and R is an upper triangular $n \times m$ matrix (where the value for m will be discussed shortly in section 3.5.2). The entries marked as "$*$" in the matrix R are of size ε^0. These appear only in upper triangular square blocks along the main diagonal, of sizes 1×1, 3×3, 5×5, etc. All of the other nonzero entries of R, marked as "$\cdot$", contain a higher-order leading power of the form ε^{2k}, $k = 1, 2, \ldots$; i.e., they vanish in significance when $\varepsilon \to 0$. As noted already, the entries in the matrix×vector product $R \cdot Y(\underline{x})$ form a basis which spans exactly the same space as the original (as $\varepsilon \to 0$, extremely ill-conditioned) RBF basis.

Another way to arrive at the same $R \cdot Y(\underline{x})$ representation is described next. Noting the structure of B from (3.5), we can factor it

$$
B = \begin{bmatrix}
Y_0^0(\underline{x}_1) & Y_1^{-1}(\underline{x}_1) & \cdots \\
Y_0^0(\underline{x}_2) & Y_1^{-1}(\underline{x}_2) & \cdots \\
\cdots & \cdots & \cdots
\end{bmatrix}
\begin{bmatrix}
\varepsilon^0 & & \\
 & \varepsilon^2 & \\
 & & \ddots
\end{bmatrix}
\begin{bmatrix}
\frac{c_{0,\varepsilon}}{2} & & \\
 & c_{1,\varepsilon} & \\
 & & \ddots
\end{bmatrix}.
$$

After QR decomposing the first factor

$$
\begin{bmatrix}
Y_0^0(\underline{x}_1) & Y_1^{-1}(\underline{x}_1) & \cdots \\
Y_0^0(\underline{x}_2) & Y_1^{-1}(\underline{x}_2) & \cdots \\
\cdots & \cdots & \cdots
\end{bmatrix}
= \begin{bmatrix} & Q & \end{bmatrix}
\begin{bmatrix}
r_{11} & r_{12} & \cdots \\
 & r_{22} & \cdots \\
 & & \ddots
\end{bmatrix},
$$

we have

$$
\begin{bmatrix} \\ B \\ \\ \end{bmatrix}
= \begin{bmatrix} & Q & \end{bmatrix}
\begin{bmatrix}
r_{11} & r_{12} & \cdots \\
 & r_{22} & \cdots \\
 & & \ddots
\end{bmatrix}
\begin{bmatrix}
\varepsilon^0 & & \\
 & \varepsilon^2 & \\
 & & \ddots
\end{bmatrix}
\begin{bmatrix}
\frac{c_{0,\varepsilon}}{2} & & \\
 & c_{1,\varepsilon} & \\
 & & \ddots
\end{bmatrix}.
$$

Transferring the diagonal matrix with powers of ε from the right-hand side to the left-hand side of the upper triangular matrix gives exactly the same result as shown in (3.6). An advantage of this second description (followed in the code in the appendix) is that it more clearly conveys that the QR decomposition can be carried out in a way that is completely independent of the choice of RBF (and of the value of ε).

In the computational algorithm, we make a minor additional base modification. The matrix R can be represented as $[R_1|R_2]$, where R_1 is a square upper triangular matrix. Therefore, assuming that the diagonal entries in R are nonzero, we can further

factor $R = R_1[\ I\ |(R_1)^{-1}R_2]$. This produces the new basis $[\ I\ |(R_1)^{-1}R_2] \cdot Y$, which we will be using:

(3.7)

$$[\ I\ |(R_1)^{-1}R_2]\cdot Y = \begin{bmatrix} 1 & & & & & & & & & . & \dots \\ & 1 & & & & & & & & . & \dots \\ & & 1 & & & & & & & . & \dots \\ & & & 1 & & & & & & . & \dots \\ & & & & 1 & & & & & . & \dots \\ & & & & & 1 & & & & . & \dots \\ & & & & & & 1 & & & . & \dots \\ & & & & & & & 1 & & . & \dots \\ & & & & & & & & 1 & . & \dots \\ & & & & & & & & & \ddots & . & \dots \end{bmatrix} \begin{bmatrix} Y_0^0(\underline{x}) \\ Y_1^{-1}(\underline{x}) \\ Y_1^0(\underline{x}) \\ Y_1^1(\underline{x}) \\ Y_2^{-2}(\underline{x}) \\ Y_2^{-1}(\underline{x}) \\ Y_2^0(\underline{x}) \\ Y_2^1(\underline{x}) \\ Y_2^2(\underline{x}) \\ \vdots \\ \vdots \end{bmatrix}.$$

Each new basis function is now a SPH, with a perturbation. These perturbations fade away as $\varepsilon \to 0$ because all of the entries denoted with "$\cdot$" are of size $O(\varepsilon^2)$ or smaller. With the previous assumption that the diagonal entries of R are nonzero, this shows that, as $\varepsilon \to 0$, the terms of the new basis converge to the successive SPH. If the number of nodes (i.e., the number of rows and columns in the collocation matrix A) is a perfect square $n = \mu_0^2$, then the RBF interpolants converge to a unique SPH expansion (3.2) with $\mu < \mu_0$. The computational procedure of using the new (but mathematically equivalent) basis remains stable as $\varepsilon \to 0$ on the further assumption that the nodes are distributed in such a way that SPH interpolation is nonsingular. Although this is very likely in any practical case, it follows from a simple argument that no node-independent basis functions can exist in more than 1-D such that nonsingularity is assured for all distinct node locations [28].

3.5. Computational considerations. In this section, we discuss the two issues of code complexity and the truncation strategy for the infinite expansions in (3.7).

3.5.1. Code complexity. A Matlab code for the RBF-QR algorithm is presented in the appendix. The cost is dominated by the QR factorization, and it will therefore have an $O(n^3)$ operation count, just as the RBF-Direct method (for which the work is dominated by one matrix inversion). Figure 3.2 displays the computational times of both methods versus the number of nodes n. The trends appear as slightly more favorable than $O(n^3)$, since Matlab's data handling becomes more efficient as matrices become larger. The figure also shows that the computational time diminishes with ε. This is due to the fact that a smaller ε allows for earlier truncation in the expansions (3.4) and fewer columns need to be retained, at first in R and then in $R_1^{-1}R_2$. This truncation procedure is described in more detail below.

3.5.2. Truncation. The matrix B in (3.5) features from the left 1 column with elements of size $O(\varepsilon^0)$, 3 columns of size $O(\varepsilon^2)$, 5 columns of size $O(\varepsilon^4)$, etc., corresponding to $\mu = 0, 1, 2, \dots$, respectively, in (3.3). With n data points, the matrix B will have n rows. We construct this matrix B as $\{B_0, B_1, B_2, \dots\}$ where the matrix block B_μ is of size $n \times (2\mu + 1)$. To ensure that all of the new basis functions are obtained to machine precision (16 significant digits), we include enough blocks that the max norm of the last included one is less than 10^{-16} of the max norm of the block that contains the nth column of B.

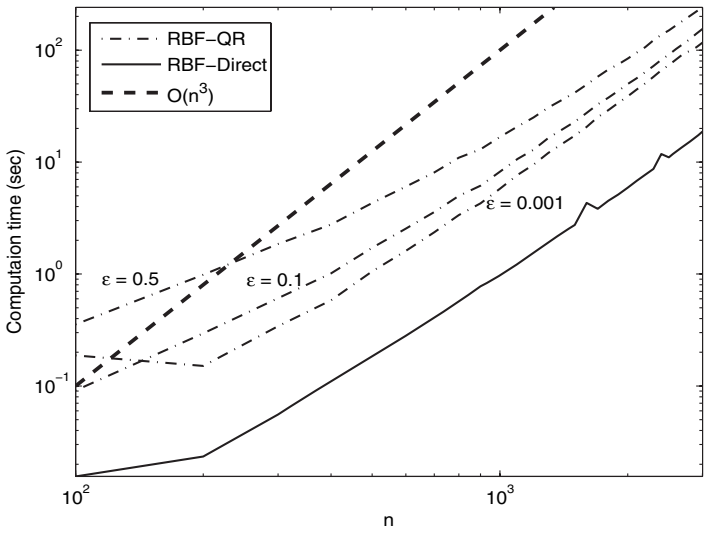

FIG. 3.2. *Plot of the computational time for the RBF-QR method versus the number of nodes for* $\varepsilon = 0.5, 0.1,$ *and* 0.001. *These are compared against the times for RBF-Direct and with a line showing the slope corresponding to* $O(n^3)$. *The times are given for a Matlab implementation running under Windows on a* 1.86 *GHz PC.*

4. Numerical tests for interpolation on a sphere. We initially consider two different node distributions, both containing $n = 1849$ nodes: (a) near-uniform distribution, obtained as the solution to a minimum energy problem—as would arise from the equilibrium of freely moving and mutually repelling equal electric charges [45] and (b) uniformly random distribution, as generated, for example, by the Matlab statements

```
n = 1849
z = 2*rand(1,n)-1;
r = sqrt(1-z.^2);
theta = 2*pi*rand(1,n);
x = r.*cos(theta);
y = r.*sin(theta);
```

(the number $n = 1849 = 43^2$ gives the same number of nodes as there are coefficients in a SPH expansion that is truncated to $\mu \leq 42$, as commonly used in SPH tests, and then denoted "T42" [41]). The two types of node distributions are shown in Figure 4.1. We consider the following two test functions:

$$
\begin{array}{lll}
\text{Gaussian bell:} & g(x,y,z) & = e^{-(\frac{2.25}{R}\arccos x)^2}, \\
\text{Cosine bell:} & c(x,y,z) & = \begin{cases} \frac{1}{2}(1+\cos(\frac{\pi}{R}\arccos x)) & x > \cos R, \\ 0 & x \leq \cos R, \end{cases}
\end{array}
\tag{4.1}
$$

of smoothness C_∞ and C_1, respectively. R is here a parameter which controls how peaked the bells are, going from spikelike at $R = 0$ to flat for increasing R. The cosine bell features a jump in the second derivative at the edge of its region of support. An equivalent way to describe the two bells is to replace $\arccos x$ by ω, where ω is the angle, as seen from the center of the sphere, between a point on the sphere and the

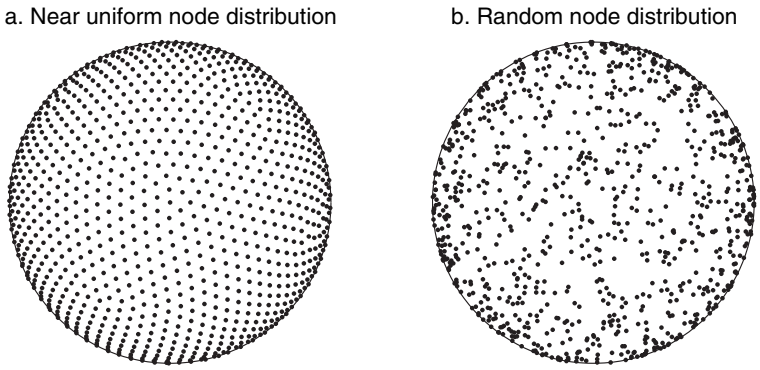

FIG. 4.1. *Different point distributions for* $n = 1849$ *node points on the unit sphere* S^2.

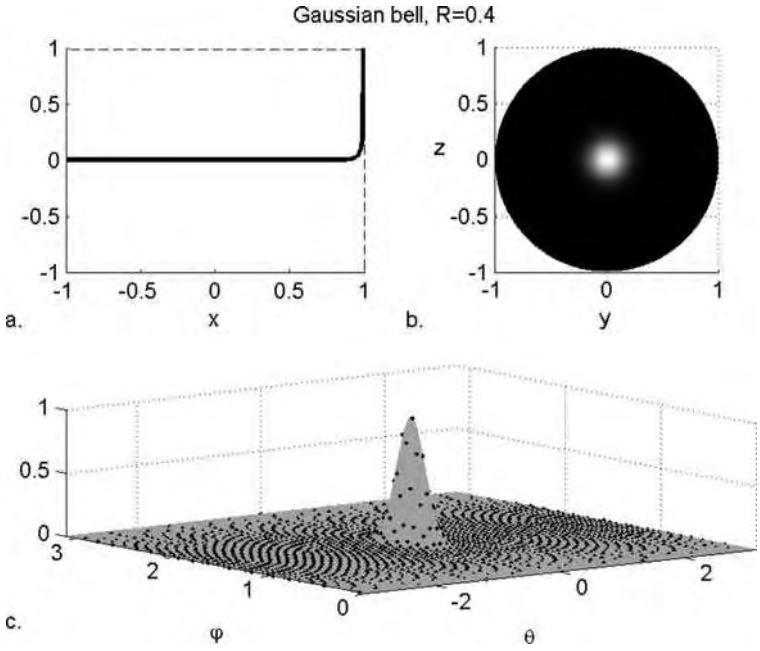

FIG. 4.2. *Three illustrations of the Gaussian bell* (a) *as a function of* x, *according to* (4.1), (b) *gray scale on a sphere surface, viewed from the positive* x*-direction, and* (c) *unrolled on a spherical coordinate* φ, θ*-plane (with the* $n = 1849$ *near-uniform node locations also marked).*

center of the respective bell. The support of the cosine bell is then given by $\omega < R$. Figures 4.2 and 4.3 show each of these two test functions in three different ways. In parts (c) of these figures, as well as in the rest of this paper, we adhere to the standard definition of spherical coordinates

$$\begin{cases} x &= \rho \sin\varphi \cos\theta, \\ y &= \rho \sin\varphi \sin\theta, \\ z &= \rho \cos\varphi \end{cases}$$

and restrict this to $\rho = 1$ for the unit sphere. The angle φ is the colatitude and is measured from the z-axis.

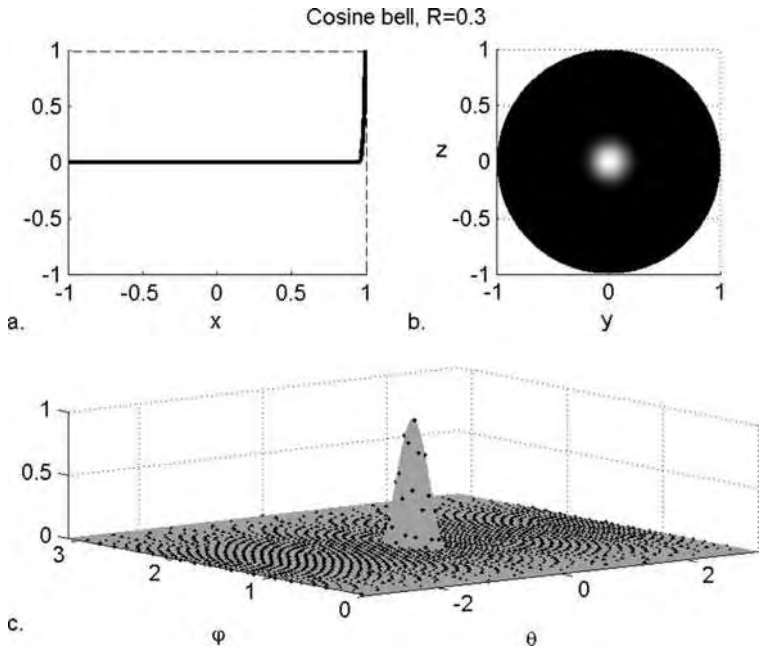

FIG. 4.3. *Cosine bell, displayed in the same manner as the Gaussian bell in Figure* 4.2.

The test functions are sampled over the two node sets, and the max norm errors of the MQ RBF interpolants are then evaluated (by dense sampling over the sphere) for different values of ε, using both RBF-Direct (based on (2.2) and (2.1)) and the new RBF-QR method.

4.1. Results for the Gaussian bell. Figure 4.4 shows the interpolation errors as functions of ε. Near-uniform node distributions are seen to give 2–3 orders of magnitude higher accuracy than random node distributions. Even with ill-conditioning issues eliminated, it is still detrimental to the overall accuracy that some small areas, purely by chance, have become much less resolved than others. We will thus not consider the random node case any further in this study.

When ε is decreased, RBF-Direct fails around $\varepsilon = 1$, whereas the RBF-QR method can be used for the remaining interval $0 \le \varepsilon \le 1$. The rapid improvement in accuracy as ε is lowered from 10^2 to 10^0 is similar to what is described analytically (in a simplified setting) in [11]. This improvement trend ceases around $\varepsilon = 1$. In the case of the wide bell ($R = 0.6$), this is due to the limited precision available in 64-bit floating point. In the case of the narrower bell ($R = 0.4$), the machine rounding level is not reached. The errors increase slightly as ε approaches the SPH case of $\varepsilon = 0$. Figure 4.5 displays in more detail how the interpolation error over the sphere varies with both ε and R. We have here run RBF-Direct to as low ε-values as possible before it breaks down due to ill-conditioning and used RBF-QR for the remaining ε-range. The large flat region for large R and small ε is a direct consequence of the 10^{-16} precision of standard floating point. The lower ε-limit for RBF-Direct is imposed by ill-conditioning. There is no equally sharp upper limit for RBF-QR, but the convergence in (3.4) degrades severely when ε increases above one. In the present case of $n = 1849$, both methods work well in a narrow overlap region for ε slightly larger than one. For lower values of n, the overlap becomes wider, whereas it may vanish for

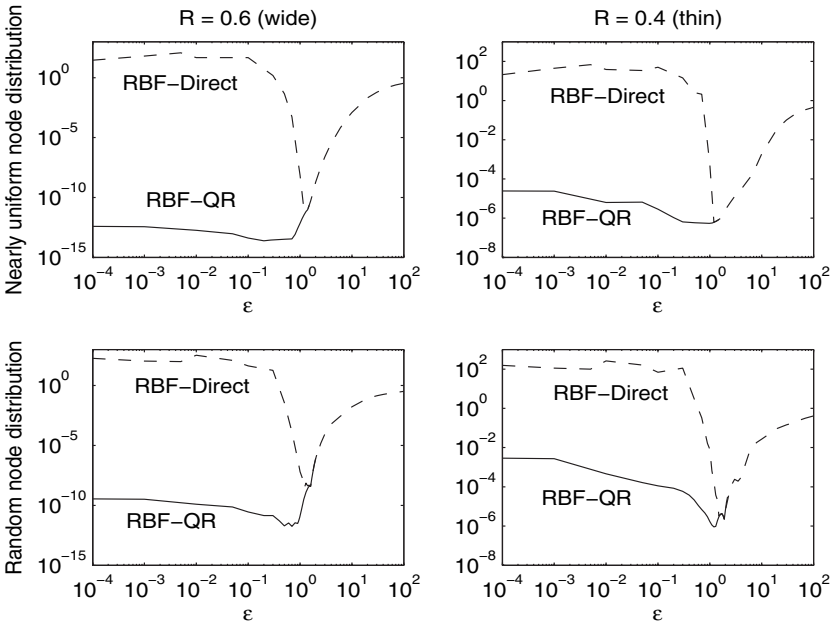

FIG. 4.4. *Log-log plots of the max norm error vs. values of ε for the Gaussian bells of two different widths. The subplots in the top row show the results with nearly uniform nodes and the bottom row with random nodes. In both cases, the number of nodes was $n = 1849$. Note that the vertical scales are different between the $R = 0.6$ and $R = 0.4$ plots.*

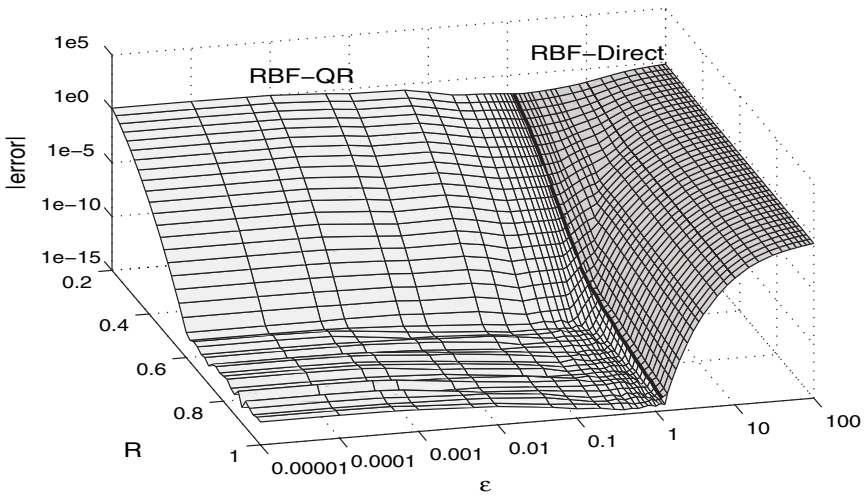

FIG. 4.5. *Gaussian bell interpolation error for different values of the bell width R and MQ shape parameter ε, in the case of $n = 1849$ near-uniform nodes. The dark line at an ε-value slightly larger than one marks where we changed the algorithm in the calculation.*

higher values of n (leaving some gap in the ε-range in which neither of the methods will be practical unless the arithmetic precision is increased beyond standard double precision).

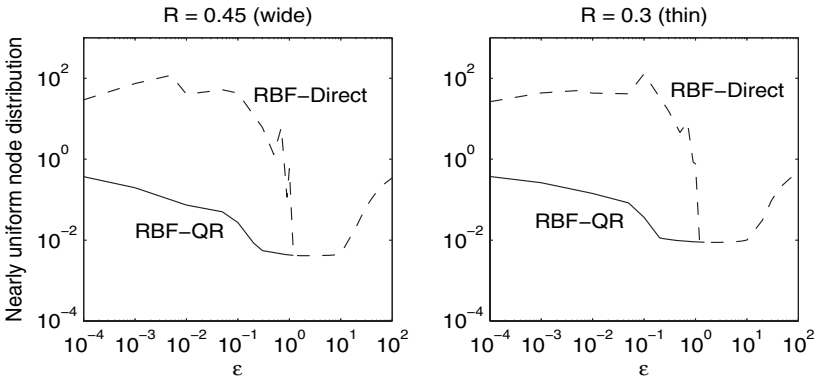

FIG. 4.6. *Log-log plot of the max norm errors in the cosine bell test case, using MQ, with* $n = 1849$ *nodes.*

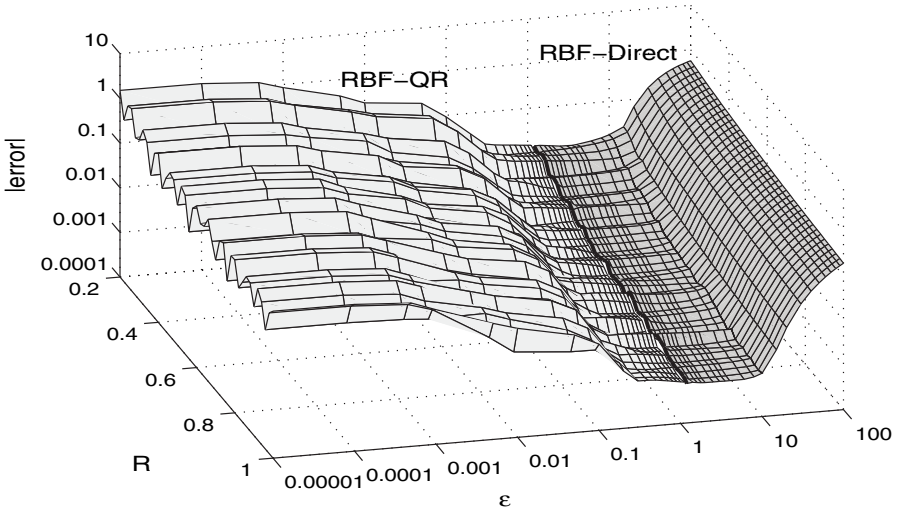

FIG. 4.7. *Cosine bell interpolation error for different values of the bell width* R *and MQ shape parameter* ε*, in the case of* $n = 1849$ *near-uniform nodes.*

4.2. Results for the cosine bell. Figure 4.6 shows that the lack of smoothness of the cosine bell (featuring a discontinuous second derivative around its edge) somehow causes much larger errors than in the Gaussian bell case, with especially large errors arising as $\varepsilon \to 0$ (the SPH case). Figure 4.7 displays, in the same style as used earlier in the Gaussian bell case, the interpolation error as a function of ε and R. In the Gaussian bell case, errors decrease very rapidly with increasing R (note the different vertical scales in the two columns of subplots in Figure 4.4). The cosine bell case is fundamentally different in that errors drop only weakly with increasing R and also grow significantly as $\varepsilon \to 0$. A more detailed discussion of this seemingly less favorable situation (and two remedies that greatly improve the accuracy at small ε) can be found in [13].

5. Some comments on the choice of "optimal" ε. By using RBF-Direct for large ε and RBF-QR for small ε, we have the capability to compute RBF interpolants (and also to solve PDEs) over a sphere for all values of ε (at least for up to a few

thousands of nodes when using standard double precision). This offers new opportunities for exploring issues such as determining an "optimal" ε and assessing whether truncated SPH expansions (i.e., RBF in the $\varepsilon \to 0$ limit) provide a "best possible" representation of functions on a sphere.

As Figures 4.4 and 4.6 illustrated (and which has been seen in many earlier calculations, e.g., [4], [9], [23], [35], [36]), the interpolation error when using RBF-Direct often decreases monotonically with decreasing ε until some point $\varepsilon = \varepsilon_{ic}$ when disastrous ill-conditioning kicks in. This has frequently raised the question of whether still much better accuracy would be attained if the ill-conditioning somehow could be eliminated. Previous results using the contour-Padé algorithm [14], [24] have shown that this sometimes can be the case. With RBF-QR, we can now extend such tests to much larger numbers of nodes. What the results in Figures 4.4 and 4.6 show is that the trend of accuracy improvement (with decreasing ε) can get broken even without ill-conditioning playing a role, although typically in a less abrupt way. There will often be a quite well defined error minimum at some location ε_{opt}. In the presently chosen test cases for interpolation, it so happened that $\varepsilon_{ic} \approx \varepsilon_{opt}$, whereas in other contexts, e.g., solving elliptic equations [24] or generating scattered-node finite-difference-type stencils [46], it often happened that $\varepsilon_{ic} > \varepsilon_{opt}$. Major improvements were then achieved by computing well into a regime that was not reachable with RBF-Direct.

6. Conclusions. The recent work by Flyer and Wright [7] clearly demonstrated the strengths of RBF methods for solving convective-type PDEs over spherical geometries (computationally, the most difficult type of PDEs since they are dissipation-free; also the most important case for many geophysical applications). The best accuracy was then obtained when the basis functions were so flat (condition number for the RBF-Direct approach often around or above 10^8) that the possibility of adverse effects from ill-conditioning could not be ignored.

We have here presented a new computational algorithm RBF-QR that can overcome this ill-conditioning even in the $\varepsilon \to 0$ limit, thereby allowing a more extensive study of how the choice of this shape parameter will affect computational accuracy. The present test cases for interpolation have been followed up by tests for both short- and long-time integration of a convective PDE [13]. While RBF-QR is the second algorithm (following contour-Padé [14]) that allows stable computations when $\varepsilon \to 0$, it is the first one which is practical in the case of thousands of data points on the surface of the sphere.

It follows from the RBF-QR algorithm that $\varepsilon \to 0$ leads to the same results as when using SPH basis functions. One might therefore ask why not just use SPH as a computational basis on the sphere. There are several reasons for not doing that:

- The limit of $\varepsilon \to 0$ is often not the best parameter choice.
- RBF can combine spectral accuracy with local refinement wherever this is needed (cf. discussion on RBF Runge phenomenon in [16]); SPH offers no such opportunities.
- Nonsingularity is guaranteed whenever $\varepsilon > 0$ but not for all node sets if $\varepsilon = 0$.

7. Appendix: A Matlab code for the RBF-QR algorithm. The test code below computes and then plots the RBF interpolant to n data points. These data are obtained from evaluating a test function at n random locations, marked as black dots in Figure 7.1. The test function and the error (difference between it and the interpolant) are also plotted. The shape parameter ε, the radial function, the number of data points to interpolate, the resolution of the grid, and the test function can all be easily modified in the initial driver part of the code. In the code listings below, the

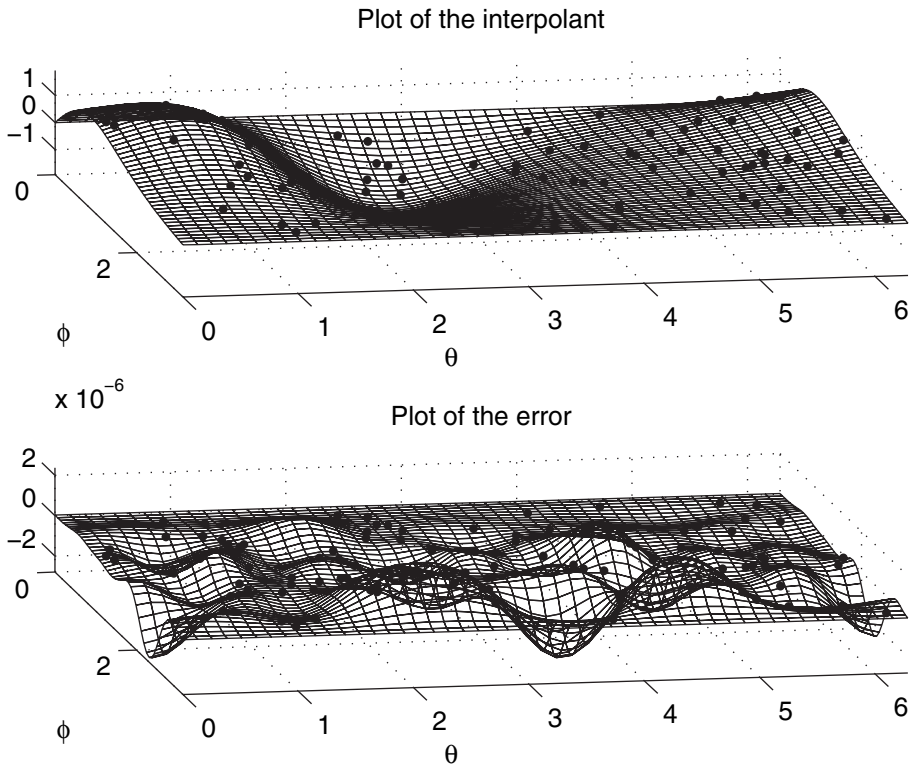

FIG. 7.1. *The graphical outout of the demo code, showing the interpolation error to be of the order* 10^{-6} *when* $\varepsilon = 10^{-8}$ *in the* $n = 100$ *node test problem.*

driver code is given first, followed by the main function RBF-QR and two supporting functions, named COEF and SPH. The function COEF evaluates expansion coefficients according to the formulas in Table 3.2, and the routine SPH evaluates spherical harmonics basis functions at specified locations. The code produces the output shown in Figure 7.1.

```
% ================================ DRIVER CODE ======================================
clear all; close all
epsilon = 10^-6;
rbf = 'IQ';                  % Basis function; valid choices: 'MQ','IMQ','IQ','GA'
n = 100;                     % Number of points to interpolate
rand('seed',4078)            % Create n random node locations
theta = 2*pi*rand(1,n); randCos = 2*rand(1,n)-1; phi = acos(randCos);
[x,y,z] = sph2cart(theta,phi-pi/2,1);
fi = @(x,y,z) x.*exp(y-z);   % Test function to interpolate
res = 50; m = res^2;         % Resolution of the grid for evaluating the interpolant
f = fi(x,y,z);               % Evaluate the data values to interpolate

% ___________________ Evaluation of the interpolant by RBF-QR _____________________
[theta_grid,phi_grid] = meshgrid(linspace(0,2*pi,res),linspace(0,pi,res));
theta_eval = reshape(theta_grid,1,res^2); phi_eval = reshape(phi_grid,1,res^2);
[xe,ye,ze] = sph2cart(theta_eval,phi_eval-pi/2,1);fe = fi(xe,ye,ze);

[beta R] = RBFQR(theta,phi,epsilon,f,rbf); index = 1;
```

```
for mu = 0:sqrt(size(R,1))-1 % Each loop adds a block of columns of SPH of order mu
                             % to Y, evaluated at the grid points
    Y(:,index:2*mu+index) = SPH(mu,theta_eval,phi_eval);
    index = index + 2*mu + 1;
end
f_RBFQR = (Y*R*beta)';       % Call to RBFQR routine

% ___________________ Plot of the interpolant and of the error ______________________
colormap(gray);

subplot(2,1,1)
surf(theta_grid,phi_grid,reshape(f_RBFQR,res,res),'FaceColor','none','LineWidth',0.05)
axis([0 2*pi 0 pi min(f_RBFQR) max(f_RBFQR)]); hold on;

plot3(theta,phi,f,'k.','MarkerSize',10); title('Plot of the interpolant');
view([-10,50]);xlabel('\phi'); ylabel('\theta'); set(gca,'ydir','reverse');

subplot(2,1,2)
surf(theta_grid,phi_grid,reshape((f_RBFQR-fe),res,res),'FaceColor','none',...
    'LineWidth',0.05)
axis([0 2*pi 0 pi min((f_RBFQR-fe)) max((f_RBFQR-fe))]); hold on;

plot3(theta,phi,zeros(size(f)),'k.','MarkerSize',10); title('Plot of the error');
view([-10,50]); xlabel('\phi'); ylabel('\theta'); set(gca,'ydir','reverse');



% ============================== FUNCTION RBFQR ===================================
function [beta, R_new] = RBFQR(theta,phi,epsilon,f,rbf)
% This function finds the RBF interpolant, with shape parameter epsilon, through the
% n node points (theta,phi) with function values f. It outputs beta, the expansion
% coefficients of the interpolant with respect to the RBF_QR basis. It calls the
% functions SPH(), which gives spherical harmonic values and COEF() which provides the
% expansion coefficients.

n = length(theta); Y = zeros(n); B = zeros(n);
mu = 0; index = 1; orderDifference = 0;
mu_n = ceil(sqrt(n))-1;             %the order of the n_th spherical harmonic

while orderDifference < -log10(eps) %eps is the machine precision
    % Each loop adds a block of columns of SPH of order mu to Y and to B.

    % Compute the spherical harmonics matrix
    Y(:,index:2*mu+index) = SPH(mu,theta,phi);

    % Compute the expansion coefficients matrix
    B(:,index:2*mu+index) = Y(:,index:2*mu+index)*COEF(mu,epsilon,rbf);
    B(:,index+mu) = B(:,index+mu)/2;

    % Truncation criterion
    if mu > mu_n-1
        orderDifference = log10(norm(B(:,[mu_n^2+1:(mu_n+1)^2]),inf)/...
            norm(B(:,(mu+1)^2),inf)*epsilon^(2*(mu_n-mu)));
    end

    index = index+2*mu+1; mu = mu+1;   % Calculate column index of next block
end

[Q,R] = qr(B);                         % QR-factorization to find the RBF_QR basis

E = epsilon.^(2*(repmat(ceil(sqrt(n+1:mu^2))-1,n,1) - ...  % Introduce the
    repmat(ceil(sqrt(1:n))-1,mu^2-n,1)'));                 % powers of epsilon
```

```
%Solve the interpolation linear system
R_new = [eye(n),E.*(R(1:n,1:n)\R(1:n,n+1:end))]'; beta = Y*R_new\f';


% ================================ FUNCTION COEF ====================================
function c_mu = COEF(mu,epsilon,rbf)
% Returns the expansion coefficients in the cases of MQ, IMQ and GA radial functions.
switch rbf
    case 'MQ'
        c_mu = -2*pi*(2*epsilon^2+1+(mu+1/2)*sqrt(1+4*epsilon^2))/...
               (mu+1/2)/(mu+3/2)/(mu-1/2)*(2/(1+sqrt(4*epsilon^2+1)))^(2*mu+1);
    case 'IMQ'
        c_mu = 4*pi/(mu+1/2)*(2/(1+sqrt(4*epsilon^2+1)))^(2*mu+1);
    case 'IQ'
        c_mu = 4*pi^(3/2)*factorial(mu)/gamma(mu+3/2)/(1+4*epsilon^2)^(mu+1)*...
               hypergeom([mu+1,mu+1],2*mu+2,4*epsilon^2/(1+4*epsilon^2));
    case 'GA'
        c_mu = 4*pi^(3/2)*exp(-2*epsilon^2)*besseli(mu+1/2,2*epsilon^2)/...
               epsilon^(2*mu+1);
end


% ================================ FUNCTION SPH =====================================
function SPHBlockMu = SPH(mu,theta,phi)
% Returns a matrix containing the spherical harmonics of order mu, evaluated at the
% (theta,phi) node points.
n = length(theta);L_mu_nu(:,1:mu+1) = legendre(mu,cos(phi))'; a = 0:mu;
t = repmat(sqrt(factorial(1+mu-a-1)./factorial(1+mu+a-1)),n,1) ...
    .*L_mu_nu(:,a+1).*exp(i*repmat(a,n,1).*repmat(theta',1,mu+1));
SPHBlockMu = sqrt((2*mu+1)/(4*pi))*[imag(t(:,end:-1:2)),real(t)];
```

Acknowledgments. Discussions with Natasha Flyer, Grady Wright, and Elisabeth Larsson are gratefully acknowledged. Comments from two referees have been very helpful in making our presentation more clear.

REFERENCES

[1] J. P. Boyd, *Chebyshev and Fourier Spectral Methods*, 2nd ed., Dover, New York, 2001.
[2] G. L. Browning, P. N. Hack, and A. Swarztrauber, *A comparison of three different numerical methods for solving differential equations on the sphere*, Monthly Weather Review, 117 (1989), pp. 1058–1075.
[3] M. D. Buhmann, *Radial Basis Functions: Theory and Implementations*, Cambridge University Press, London, 2003.
[4] R. Carlson and T. A. Foley, *The parameter R2 in multiquadric interpolation*, Comput. Math. Appl., 21 (1991), pp. 29–42.
[5] J. R. Driscoll and D. M. Healy, *Computing Fourier transforms and convolutions on the 2-sphere*, Adv. Appl. Math., 15 (1994), pp. 202–250.
[6] T. A. Driscoll and B. Fornberg, *Interpolation in the limit of increasingly flat radial basis functions*, Comput. Math. Appl., 43 (2002), pp. 413–422.
[7] N. Flyer and G. Wright, *Transport schemes on a sphere using radial basis functions*, J. Comput. Phys., 226 (2007), pp. 1059–1084.
[8] N. Flyer and G. Wright, *Solving the Nonlinear Shallow Water Wave Equations Using Radial Basis Functions*, manuscript.
[9] T. A. Foley, *Near optimal parameter selection for multiquadric interpolation*, J. Appl. Sci. Comput., 1 (1994), pp. 54–69.
[10] B. Fornberg, *A Practical Guide to Pseudospectral Methods*, Cambridge University Press, Cambridge, 1996.
[11] B. Fornberg and N. Flyer, *Accuracy of radial basis function interpolation and derivative approximations on 1-D infinite grids*, Adv. Comput. Math., 23 (2005), pp. 5–20.

[12] B. Fornberg and D. Merrill, *Comparison of finite difference and pseudospectral methods for convective flow over a sphere*, Geophys. Res. Lett., 24 (1997), pp. 3245–3248.
[13] B. Fornberg and C. Piret, *On choosing a radial basis function and a shape parameter when solving a convective PDE on a sphere*, J. Comput. Phys., to appear.
[14] B. Fornberg and G. Wright, *Stable computation of multiquadric interpolants for all values of the shape parameter*, Comput. Math. Appl., 48 (2004), pp. 853–867.
[15] B. Fornberg, G. Wright, and E. Larsson, *Some observations regarding interpolants in the limit of flat radial basis functions*, Comput. Math. Appl., 47 (2004), pp. 37–55.
[16] B. Fornberg and J. Zuev, *The Runge phenomenon and spatially variable shape parameters in RBF interpolation*, Comput. Math. Appl., 54 (2007), pp. 379–398.
[17] F. X. Giraldo and T. E. Rosmond, *A scalable spectral element Eulerian atmospheric model (SEE-AM) for NWP: Dynamical core tests*, Monthly Weather Review, 132 (2004), pp. 133–153.
[18] J. J. Hack and R. Jakob, *Description of a Global Shallow Water Model Based on the Spectral Transform Method*, Technical note TN 343 STR NCAR, 1992.
[19] R. L. Hardy, *Multiquadric equations of topography and other irregular surfaces*, J. Geophys. Res., 76 (1971), pp, 1905–1915.
[20] S. Hubbert and B. Baxter, *Radial basis functions for the sphere*, in Progress in Multivariate Approximation, Internat. Ser. Numer. Math. 137, Birkhauser, Boston, 2001, pp. 33–47.
[21] E. J. Kansa, *Multiquadrics - A scattered data approximation scheme with applications to computational fluid-dynamics.* I. *Surface approximations and partial derivative estimates*, Comput. Math. Appl., 19 (1990), pp. 127–145.
[22] E. J. Kansa, *Multiquadrics - A scattered data approximation scheme with applications to computational fluid-dynamics.* II. *Solutions to parabolic, hyperbolic and elliptic partial differential equations*, Comput. Math. Appl., 19 (1990), pp. 147–161.
[23] E. J. Kansa and Y. Hon, *Circumventing the ill-conditioning problem with multiquadric radial basis functions: Applications to elliptic partial differential equations*, Comput. Math. Appl., 39 (2000), pp. 123–137.
[24] E. Larsson and B. Fornberg, *A numerical study of radial basis function based solution methods for elliptic PDEs*, Comput. Math. Appl., 46 (2003), pp. 891–902.
[25] E. Larsson and B. Fornberg, *A Stable Algorithm for Flat Radial Basis Functions*, manuscript.
[26] E. Larsson and B. Fornberg, *Theoretical and computational aspects of multivariate interpolation with increasingly flat radial basis functions*, Comput. Math. Appl., 49 (2005), pp. 103–130.
[27] W. R. Madych and S. A. Nelson, *Bounds on multivariate polynomials and exponential error estimates for multiquadric interpolation*, J. Approx. Theory, 70 (1992), pp. 94–114.
[28] J. Y. McLeod and M. L. Baart, *Geometry and Interpolation of Curves and Surfaces*, Cambridge University Press, Cambridge, 1998.
[29] P. E. Merilees, *The pseudospectral approximation applied to the shallow water equation on a sphere*, Atmosphere, 11 (1973), pp. 13–20.
[30] P. E. Merilees, *Numerical experiments with the pseudospectral method in spherical coordinates*, Atmosphere, 12 (1974), pp. 77–96.
[31] M. Mohlenkamp, *A fast transform for spherical harmonics*, J. Fourier Anal. Appl., 5 (1999), pp. 159–184.
[32] D. Potts, G. Steidl, and M. Tasche, *Fast and stable algorithms for discrete spherical Fourier transforms*, Linear Algebra Appl., 275–276 (1998), pp. 433–450.
[33] M. J. D. Powell, *The theory of radial basis function approximation in* 1990, in Advances in Numerical Analysis, Vol. II: Wavelets, Subdivision Algorithms and Radial Functions, W. Light, ed., Oxford University Press, Oxford, 1990, pp. 105–210.
[34] V. Rokhlin and M. Tygert, *Fast algorithms for spherical harmonic expansions*, SIAM J. Sci. Comput., 27 (2005), pp. 1903–1928.
[35] C. Shu, H. Ding, and K. S. Yeo, *Local radial basis function-based differential quadrature method and its application to solve two-dimensional incompressible Navier-Stokes equations*, Comput. Methods Appl. Mech. Engrg., 192 (2003), pp. 941–954.
[36] S. Rippa, *An algorithm for selecting a good value for the parameter c in radial basis function interpolation*, Adv. Comput. Math., 11 (1999), pp. 193–210.
[37] R. Schaback, *Comparisons of radial basis function interpolants*, in Multivariate Approximation: From CAGD to Wavelets, K. Jetter and F. I. Utreras, eds., World Scientific, Singapore, 1993, pp. 293–305.
[38] R. Schaback, *Multivariate interpolation by polynomials and radial basis functions*, Constr. Approx., 21 (2005), pp. 293–317.

[39] W. F. Spotz, M. A. Taylor, and P. N. Swarztrauber, *Fast shallow water equation solvers in latitude-longitude coordinates*, J. Comput. Phys., 145 (1998), pp. 432–444.
[40] P. N. Swarztrauber, *Spectral transform methods for solving the shallow-water equations on the sphere*, Monthly Weather Review, 124 (1996), pp. 730–744.
[41] M. Taylor, J. Tribbia, and M. Iskandarani, *The spectral element method for the shallow water equations on the sphere*, J. Comput. Phys., 130 (1997), pp. 92–108.
[42] C. Temperton, *On scalar and vector transform methods for global spectral models*, Monthly Weather Review, 119 (1991), pp. 1303–1307.
[43] S. J. Thomas and R. D. Loft, *The NCAR spectral element climate dynamical core: Semi-implicit, Eulerian formulation*, J. Sci. Comput., 25 (2005), pp. 307–322.
[44] L. N. Trefethen, *Spectral Methods in Matlab*, SIAM, Philadelphia, 2000.
[45] R. S. Womersley and I. Sloan, *Interpolation and Cubature on the Sphere*, http://web.maths.unsw.edu.au/rsw/Sphere/.
[46] G. Wright and B. Fornberg, *Scattered node compact finite difference-type formulas generated from radial basis functions*, J. Comput. Phys., 212 (2006), pp. 99–123.
[47] J. Yoon, *Spectral approximation orders of radial basis function interpolation on the Sobolev space*, SIAM J. Math. Anal., 33 (2001), pp. 946–958.

Appendix C

Paper 3 On choosing a radial basis function and a shape parameter when solving a convective PDE on a sphere

On choosing a radial basis function and a shape parameter when solving a convective PDE on a sphere

Bengt Fornberg [*,1], Cécile Piret [2]

University of Colorado, Department of Applied Mathematics, 526 UCB, Boulder, CO 80309, USA

Abstract

Radial basis function (RBF) approximations have been used for some time to interpolate data on a sphere (as well as on many other types of domains). Their ability to solve, to spectral accuracy, convection-type PDEs over a sphere has been demonstrated only very recently. In such applications, there are two main choices that have to be made: (i) which type of radial function to use, and (ii) what value to choose for their shape parameter (denoted by ε, and with flat basis functions -stretched out in the radial direction- corresponding to $\varepsilon = 0$). The recent RBF-QR algorithm has made it practical to compute stably also for small values of ε. Results from solving a convective-type PDE on a sphere are compared here for many choices of radial functions over the complete range of ε-values (from very large down to the limit of $\varepsilon \to 0$). The results are analyzed with a methodology that has similarities to the customary Fourier analysis in equispaced 1-D periodic settings. In particular, we find that high accuracy can be maintained also over very long time integrations. We furthermore gain insights into why RBFs sometimes offer higher accuracy than spherical harmonics (since the latter arise as an often non-optimal special case of the former). Anticipated future application areas for RBF-based methods in spherical geometries include weather and climate modeling.

Key words: Radial basis functions, RBF, shape parameter, Wendland functions, sphere, spherical harmonics, RBF-QR method.
1991 MSC: 58J45, 65D25, 65M70, 76M22

* Corresponding author.
Email addresses: fornberg@colorado.edu (Bengt Fornberg), piret@colorado.edu (Cécile Piret).

[1] The work was supported by the NSF grants DMS-0309803, DMS-0611681, and ATM-0620068.
[2] The work was supported by the first two NSF grants mentioned above.

1 Introduction

Many application areas, such as geophysics (including weather and climate modeling), astrophysics, quantum mechanics, etc. require PDEs to be solved in spherical geometries. Flyer and Wright [7], [8] have recently shown that an RBF-based pseudospectral (PS) approach can be very successful for solving wave-type PDEs (such as pure convection equations and the shallow water equations) on a spherical surface. Compared to other spectral approaches, such as double Fourier methods [13], [29], [30], [36], spherical harmonics methods [2], [19], [21], [38], [40], and spectral element methods [18], [31], [37], [39], [41], they found the RBF approach to be particularly promising since it features

- algebraic simplicity (complete codes for PDE test cases are often less than 50 lines of Matlab),
- immediate generalizability from spherical to arbitrarily shaped surfaces, and
- opportunities for combining spectral accuracy with local refinement.

Most RBFs depend on a shape parameter ε, with $\varepsilon \to 0$ corresponding to the limit of increasing flatness. Lowering the value of ε usually increases the resulting accuracy to some point when one or both of the following two factors halt or reverse this trend:

(1) Onset of disastrous numerical ill-conditioning if using a direct implementation of the RBF procedure (denoted RBF-Direct, to be explained in Section 2.1)
(2) Onset of a Runge phenomenon reminiscent of that for polynomial interpolation, as explained in [17], Section 3 (potentially disastrous mainly in the presence of boundaries or variable node densities, else mainly setting a limit for the accuracy that can be reached).

Figure 1 illustrates these two factors in three different cases from the literature. The top row of subplots shows how the error varies with ε when solving a Poisson equation over a unit disk, as described in [25]. The dashed comparison line shows the accuracy that is reached with the previously most accurate available procedure, Fourier pseudospectral (PS) in the angular direction and Chebyshev PS radially. In all cases, the resolution was 16 nodes on the boundary and 48 in the interior. In the top right subplot, computational ill-conditioning for small ε was eliminated with the Contour-Padé algorithm [15]. The middle row of subplots shows similar trends in the context of interpolating a Gaussian bell over the surface of a sphere when using $n = 1849$ nearly uniformly distributed nodes. For further details in this case, see [14]. The RBF-QR algorithm, introduced in that work, was used (instead of the Contour-Padé algorithm) to eliminate the ill-conditioning for the right subplot. The single subplot in the

bottom row (with data and further explanations given in [7]) shows the max norm error after a cosine bell has been convected once around the sphere when solving the time dependent PDE (5), to be described later in Section 3. The main goal of the present study is to explore this last test case further, in particular when the numerical ill-conditioning for low ε-values has been eliminated. By means of both numerical computations and through some novel analysis, we will

(1) Explore how the accuracy varies with
- RBF type,
- Shape parameter (for full range of $\varepsilon \geq 0$),
- Length of time integration.

(2) Discuss the $\varepsilon = 0$ case since this, as was found in [14], is usually equivalent to using spherical harmonics (SPH) in place of RBFs.

We present in Section 2 first a very brief introduction to RBF interpolation, and we then quote some relevant results from the literature, such as the significance of the flat basis function limit. The convective PDE and results using one type of RBF discretization are presented in Section 3. We extend in Section 4 these results to also include a large number of different RBF choices, again over the full range of ε-values. In the present context, the differences in performance between the smooth RBF types are found to be minor, whereas the performances of the non-smooth RBF are much inferior. Some of these results can be understood through the analysis in Section 5, generalizing to scattered node situations on the sphere the Fourier-based arguments that are routinely used on equispaced periodic problems in 1-D. In Section 6, focusing on summaries and conclusions, we again address why (in the present context of long time integration), smooth basis functions are superior to non-smooth ones, regardless of whether the solution that is convected is smooth or not. The Appendices A and B provide technical details on some RBF-QR implementation issues.

2 RBF methodology

2.1 The form of an RBF interpolant

The basic RBF interpolant takes the form

$$s(\underline{x}) = \sum_{i=1}^{n} \lambda_i \, \phi(\|\underline{x} - \underline{x}_i\|), \tag{1}$$

where $||\cdot||$ denotes the Euclidean norm. In order for it to take the values f_i at locations $\underline{x}_i$, $i = 1, 2, \ldots n$, the expansion coefficients λ_i need to satisfy

$$A\,\underline{\lambda} = \underline{f} \tag{2}$$

where the entries of the matrix A are $A_{i,j} = \phi(||\underline{x}_i - \underline{x}_j||)$. We denote numerical use of (2) followed by (1) as "RBF-Direct". In this study, we will concentrate our attention on the radial functions $\phi(r)$ listed in Table 1. The parameter ε, included in all but the piecewise smooth global cases CU and TPS, is known as the *shape parameter*. The listed Wendland functions [43] are those of lowest degree which guarantee that the A-matrix is positive definite for all distinct node locations in 2 and 3 dimensions. This property holds in all dimensions also for IMQ, IQ, and GA. In the MQ, CU, and TPS cases, A is still symmetric. For MQ, non-singularity remains guaranteed, but positive definiteness is lost. Additional issues arise in the CU and TPS cases. Commonly used variations of (1) are for MQ

$$s(\underline{x}) = \alpha + \sum_{i=1}^{n} \lambda_i\, \phi(\|\underline{x} - \underline{x}_i\|), \quad \text{with the constraint} \quad \sum_{i=1}^{n} \lambda_i = 0 \tag{3}$$

and for CU and TPS

$$s(\underline{x}) = \alpha + \beta x + \gamma y + \delta z + \sum_{i=1}^{n} \lambda_i\, \phi(\|\underline{x} - \underline{x}_i\|), \tag{4}$$

with the constraints

$$\sum_{i=1}^{n} \lambda_i = \sum_{i=1}^{n} \lambda_i x_i = \sum_{i=1}^{n} \lambda_i y_i = \sum_{i=1}^{n} \lambda_i z_i = 0\ .$$

For more detailed discussions, see [3], [33] and [35].

The most notable feature of the Wendland functions is their compact support in case ε is large, leading to sparse A-matrices, and therefore with possibilities for high computational speeds both in evaluating (1) and in solving (2) (for example if using conjugate gradient-type methods). In the present case with nodes on the unit sphere, all sparsity is lost if $\varepsilon < \frac{1}{2}$.

2.2 RBFs for PDEs

In 1990, Kansa introduced collocation with RBFs as a means to approximate spatial derivatives, and thus to numerically solve PDEs [22], [23]. In case of smooth RBFs, this approach is typically spectrally accurate [4], [28], [47]. Another notable advantage with this RBF approach (compared to, say, finite difference, finite element, and finite volume methods) is that it replaces the

often challenging task of creating computational meshes over irregular domains with the easier one of scattering computational nodes.

Driscoll and Fornberg [5] observed that, in the flat basis function limit $\varepsilon \to 0$ for globally smooth RBFs in 1-D, the interpolant in general converges to Lagrange's interpolation polynomial. From this follows that the RBF approach for PDEs can be viewed as a generalization (to irregular domains and to scattered nodes) of the pseudospectral (PS) method [1], [10], [42]. This approach is therefore nowadays often described as the RBF-PS method. In a 1-D periodic setting, the $\varepsilon \to 0$ limit will reproduce the Fourier-PS method [5]. For nodes on a sphere, the corresponding limit was found in [14] to agree with a spherical harmonics (SPH-PS) method. More results about RBF in the flat basis function limit can be found for example in [11], [12], [16], [26], [34].

As noted in the introduction, Flyer and Wright [7] were the first to use RBFs to solve purely convective (i.e. non-dissipative) PDEs over a spherical surface. Because they implemented their scheme based on direct use of (2) followed by (1), ill-conditioning prevented their numerical explorations from being extended also to arbitrarily small values of ε.

Much more materials on both 'RBF methodology' and 'RBFs for PDEs' can be found in the two recent books [43] and [6].

3 Time dependent PDE on a sphere

3.1 Test problem

The standard PDE test problem that we will consider describes 'solid body' rotation/convection around an axis that is inclined by the angle α relative to the polar axis (cf. [7], [13], [44], and Figure 2 a). Following the convention in many applications, we define spherical coordinates as shown in Figure 2 b

$$\begin{cases} x = \rho \cos\varphi \cos\theta \\ y = \rho \sin\varphi \cos\theta \\ z = \rho \sin\theta \end{cases} .$$

This differs from standard spherical coordinates (as used for ex. in [14]) both in the use of latitude (as opposed to co-latitude) and also in the directions denoted by θ and φ. In the present coordinates, the governing PDE becomes

$$\frac{\partial u}{\partial t} + (\cos\alpha - \tan\theta \ \sin\varphi \ \sin\alpha)\frac{\partial u}{\partial \varphi} - \cos\varphi \ \sin\alpha \frac{\partial u}{\partial \theta} = 0. \qquad (5)$$

One full revolution will correspond to the time $t = 2\pi$.

The pole singularities enter through the $\tan\theta$ factor when $\theta = \pm\frac{\pi}{2}$. These singularities are not physical, but arise only as a consequence of the (θ, φ)-system itself being singular at these locations. When the RBF differentiation matrix (DM, representing the spatial operator of (5) in terms of the node values of u) is formed as described in [7], these singularities will therefore vanish (the DM reflects the physical operator, but not what coordinate system it happened to be expressed in during an intermediate derivation step).

The initial condition that we will use is the *Cosine bell*, shown in Figure 3. It can be described in Cartesian coordinates as

$$u(x, y, z, 0) = \begin{cases} \frac{1}{2}(1 - \cos(\frac{\pi}{R} \arccos x)) & x > \cos R \\ 0 & x \leq \cos R \end{cases}, \tag{6}$$

with $R = 1/3$, and restricted to the surface of the unit sphere.

Cosine bells have become standard initial conditions for convective test calculations on a sphere [21], [31], [36], [39] for several reasons:

(1) Their compact support makes it particularly easy to display and to interpret dispersive errors after convection,
(2) The easy-to-change peak width R allows testing to be carried out on different spatial scales,
(3) The discontinuous second derivative at the base of the bell prevents very high order methods from producing misleadingly good results compared to what might be expected in cases of more physically relevant data.

3.2 Different node distributions

Because of the clear advantages seen in previous works [7], [14] of using near-uniform rather than fully random node distributions, we limit the discussion here to the former case. When interpolating using SPH, Womersley and Sloan [45], [46] noticed very large differences also between different types of near-uniform distributions. The two near-uniform node sets that are used in this study are both taken from [45], and are shown in Figure 4. They are described as 'minimal energy' (ME) and 'maximal determinant' (MD), respectively. The former can be obtained as the equilibrium of freely moving nodes on the sphere surface, repelling each other like equal point charges. In the MD case, node locations are instead obtained by maximizing the determinant of a certain 'Gram matrix'. Womersley and Sloan report that SPH interpolation errors

(measured in any standard norm, or as a Lebesgue constant) can be several orders of magnitude larger in ME than in MD cases. Since RBF interpolation in the $\varepsilon \to 0$ limit usually corresponds to SPH interpolation, it is not surprising that the choice of nodes (ME vs. MD) will influence the RBF accuracy also for non-zero ε (although gradually less so when ε is increased, as will be illustrated in Section 3.4).

3.3 Method of lines (MOL) formulation and time stepping considerations for the PDE test problem

The test problem (5) can be written more briefly $\frac{\partial u}{\partial t} + L(u) = 0$, where L is the spatial derivative operator. The RBF-Direct-based DM that arises when approximating the spatial derivative terms in (5) was shown in [7] to take the form

$$D = B \cdot A^{-1} \,, \tag{7}$$

where B is antisymmetric, with elements

$$B_{i,j} = L\ \phi(||\underline{x} - \underline{x}_j||)|_{\underline{x}=\underline{x}_i} \,, \tag{8}$$

and A is defined in (2), with elements

$$A_{i,j} = \phi(||\underline{x}_i - \underline{x}_j||) \,. \tag{9}$$

We will here compute this matrix D either immediately through (7)-(9) (RBF-Direct), or via RBF-QR, as described in Appendix A. The ill-conditioning problem with RBF-Direct originates from the fact that, as $\varepsilon \to 0$, A becomes very nearly singular, causing elements of A^{-1} to diverge to plus or minus infinity. A vast amount of numerical cancellation then occurs when the $O(1)$-sized matrix D is formed as the matrix product (7).

The key concept behind the RBF-QR algorithm is the recognition that the basis functions $\phi(||\underline{x} - \underline{x}_i||)$, $i = 1, 2, \ldots, n$, when ε is small, form a terrible base that nevertheless spans an excellent approximation space. The RBF-QR algorithm expands each basis function in a SPH series, after which it transpires that we can obtain a very well conditioned base *spanning exactly the same space*. Using this new base bypasses the ill-conditioning but leads otherwise to identical results. Explained somewhat differently: For all values of ε, the entries of D behave in a well-conditioned way with respect to perturbations in the input data, i.e. the node locations $\underline{x}_i$. In the case of small ε, RBF-Direct is an ill-conditioned algorithm for numerically computing D, while RBF-QR is a well-conditioned one.

A matrix that is a product of an antisymmetric and a positive definite one can only have purely imaginary eigenvalues. The DMs that arise from RBF

discretization of the spatial operator in (5) will thus be of this type for the positive definite RBF choices in Table 1 (IMQ, IQ, GA, W2, W4, W6). Standard time stepping methods, such as the fourth order Runge-Kutta method (RK4), will therefore be applicable, no matter how the nodes are scattered over the surface of the sphere. An extension to the result above, given in [32], extends it to (3) or (4) rather than (1) in the remaining cases of MQ, CU and TPS. In the present tests, we found the eigenvalues to be purely imaginary also without invoking this extension, allowing us to use (1) in all cases.

Numerical tests using RBFs for convecting the cosine bell (as well as results for the second test problem in [44]) were presented in [7]. The errors they reported after a computational time corresponding to one full revolution around the sphere ($t = 12$ days in their notation, $t = 2\pi$ in our notation) come from three different sources:

(1) Time stepping errors in the RK4 scheme,
(2) Properties of the DM,
(3) Errors when the numerical solution, defined at the grid points, is interpolated and compared against the analytic solution across the complete sphere.

The issue (1) can be resolved by using small enough RK4 time steps, so that the error types (2) and (3) will dominate (this still allows much longer time steps to be taken than what is feasible in the alternative methods, as reported in [7]; see also the discussion here in Section 5). In order to more clearly analyze the errors coming from the DM (issue 2), we will here make use of the fact that the discretized test problem can be integrated analytically in time. Letting $\underline{u}(t)$ denote a column vector with n entries, containing the numerical approximations at the n node points as functions of time, the discretization of (5) takes the form

$$\frac{\partial \underline{u}}{\partial t} + D\ \underline{u} = 0\ , \tag{10}$$

for which the analytic solution is

$$\underline{u}(t) = e^{-\,tD}\ \underline{u}(0)\ .$$

3.4 Numerical tests using IMQ RBF

The RBF-QR method is based on certain series expansions which involve powers of ε, and these might fail to converge for large ε. In contrast, RBF-Direct fails due to ill-conditioning for low values of ε. If the number of nodes n is relatively low (such as $n = 1849$ used throughout this study), there will

usually be some range in which both methods work, but this overlap can get lost as n is increased further.

The first issue that arises (already at time $t = 0$, i.e. before time stepping has even started) is how accurately the cosine bell will be represented as an RBF interpolant of the discrete initial data that is shown in Figure 3 c. Figure 5 (for SPH, i.e. for most smooth RBFs in their $\varepsilon \to 0$ limit) and the curve marked 'Interpolation' in Figure 6 a (for a wide range of ε values) show that direct interpolation based on the values at the $n = 1849$ ME nodes can lead to very large errors in-between the node points (positioned as seen in Figures 3 c and 4). This is entirely in agreement with the observations in [46]. The error level drops significantly when ε is increased from $\varepsilon = 0$, and it is particularly low around $2 \lesssim \varepsilon \lesssim 10$ (Figure 6 a). Only here is the error comparable to what is obtained with MD nodes throughout the full range $0 \leq \varepsilon \lesssim 10$ (Figure 6 b), confirming that the latter node type offers much more 'robust' interpolation. However, a still better option with regard to obtaining a uniformly good RBF representation of the initial condition is possible through a least squares approach, and is illustrated by the curves marked 'Least squares' in Figures 6 a-d. These RBF representations were obtained by a 2-stage process of first finding the best representation of the analytic initial condition (the cosine bell) in terms of SPH up to order $\mu = \sqrt{n} = 43$ (also featuring $\mu^2 = n = 1849$ free parameters) through least squares over a much denser point set, followed by evaluation of this SPH approximation back at the original $n = 1849$ node points. With this initial filter-type step, we obtain the initial condition across the full sphere with higher accuracy than was the case with immediate interpolation using either of the ME or MD node sets. Furthermore, the accuracy becomes almost completely independent of the details of the node distributions. Figures 6 c, d illustrate that the piecewise smooth RBF are much less sensitive in this regard (of ME vs. MD). In all the computations that are described below, we use ME nodes and this least square procedure to get the RBF representation of the initial condition at $t = 0$. The same filter-type strategy as described above is a routine part of most SPH-PS calculations, then typically applied at every time step rather than as here only at $t = 0$.

Figures 7 a,b show how the accuracy at $t = 10$ and $t = 10,000$ vary with ε in the cases of IMQ and W6 - typical results for a smooth and a piecewise smooth radial function, respectively. Including two more RBF types, Figures 8 a,b show the time evolution of the error over $0 \leq t \leq 10$ and over $0 \leq t \leq 10,000$, respectively. We notice that the error degrades severely in time for non-smooth RBF, whereas it holds up extremely well for the smooth ones. In these and the following cases, the error was measured as the maximal discrepancy compared to the analytic solution, over the $n = 1849$ node points.

We extend next these comparisons to include all the radial functions listed in

Table 1.

4 Comparisons between different RBF types

There has been numerous suggestions in the literature that some types of RBFs generally tend to give more accurate results than others. For example, MQ is often particularly highly regarded, whereas concerns have been raised against GA, sometimes for the reason that GA does not support any 'exact polynomial reproduction' properties on infinite lattices (when $\varepsilon > 0$) [3].

The accuracy that is achieved by different RBF methods is highly problem dependent. For example, interpolation of non-smooth data places very different demands on the method than does long-term solution of convective-type PDEs. With the combination of RBF-Direct and RBF-QR, we have now the ability to run the convective test problem for the full set of RBFs shown in Table 1, throughout the full range of ε (from zero and upwards), giving the results shown in Figures 9 and 10. As we have noted already, smooth RBFs give excellent accuracy (not much different from the initial error at $t = 0$) also over very long time integrations. The differences between these smooth RBFs are in the present context seen to be very minor in comparison to the much more rapid loss of accuracy seen for the piecewise smooth RBF. These latter ones differ between themselves largely according to their smoothness, with the higher order ones (such as W4 and W6) being more accurate than, say, TPS, CU, or W2. In order to offer some accuracy over longer time integrations, also the Wendland functions need to be scaled so that they become relatively flat (ε small), causing their A-matrices to lose its sparseness. However, since the Wendland-based D-matrices (7) are never sparse, these RBFs do not (in the present PDE context) seem to offer any speed advantages over the standard smooth RBF types.

In Table 1, we have included ε for all the RBF types apart from CU and TPS. In the case of CU, including ε (i.e. using $\phi(r) = |\varepsilon r|^3$) would be pointless, since all results would turn out ε independent. Thus we always use $\phi(r) = |r|^3$ for CU. Regarding TPS, there would in fact be a weak ε dependence, which mainly would manifest itself in an additional type of singularity as $\varepsilon \to 0$, with no apparent redeeming features. Thus, all TPS results that we give are based on $\phi(r) = r^2 \log |r|$. When CU and TPS results are displayed in Figures 9 and 10, they are thus displayed as ε-independent straight lines (although this is not strictly true in the case of TPS).

5 Analysis of the numerical results via properties of the DMs

The numerical results in Sections 3.4 and 4 can be understood through spectral analysis that is conceptually similar to Fourier analysis of equispaced finite difference (FD) and RBF approximations to the model equation

$$\frac{\partial u}{\partial t} + \frac{\partial u}{\partial x} = 0 \; . \tag{11}$$

These steps are explained in the next subsections.

5.1 1-D equispaced FD approximations

It has been explained and illustrated repeatedly in the literature (with [9] and [24] being early references) how the accuracy of a FD scheme can be understood from how it acts on individual Fourier modes. Since

$$\frac{d}{dx}\, e^{i\omega x} = i\, \omega\, e^{i\omega x} \; ,$$

$u(x) = e^{i\omega x}$ is an eigenfunction to the $\frac{d}{dx}$-operator. If we consider the discrete situation with a grid spacing h, the possible frequency range (due to aliasing) is $\omega \in [-\omega_{\max}, \omega_{\max}]$ where $\omega_{\max} = \frac{\pi}{h}$. Applying a FD2 (centered second order FD) scheme to $u(x) = e^{i\omega x}$ similarly gives

$$\frac{u(x+h) - u(x-h)}{2h} = \frac{e^{i\omega(x+h)} - e^{i\omega(x-h)}}{2h} = i\, \frac{\sin\, \omega h}{h}\, e^{i\omega x} \; , \tag{12}$$

i.e. the Fourier mode is again an eigenfunction, but the eigenvalue has changed from $i\omega$ to $i\, \frac{\sin \omega h}{h}$. Ignoring for now the factor "i", the eigenvalues are $f_{PS}(\omega) = \omega$ and $f_{FD2}(\omega) = \frac{\sin\, \omega h}{h}$, respectively Figure 11 illustrates these eigenvalues, as functions of ω, together with similar factors also for some FD methods of higher orders. While the PS method (limit of FD methods of increasing orders, cf. [10]) correctly treats all modes that can be represented on a grid with spacing h, lower order FD methods contain significant errors in all modes. In the context of time integration of (11), these errors correspond to errors in the phase speed of traveling waves. The longer a time integration extends, the larger number of high modes will end up out of phase, and thereby become 'lost' as far as contributing to the overall accuracy. The lower the order of the FD approximation is, the more severe will this degradation over time become.

If we furthermore simplify by setting $h = 1$ (i.e. consider a unit-spaced infinite

1-D grid), we find

$$\begin{aligned} f_{FD2}(\omega) &= (\sin\omega) \\ f_{FD4}(\omega) &= (\sin\omega)(1+\tfrac{2}{3}(\sin\tfrac{\omega}{2})^2) \\ f_{FD6}(\omega) &= (\sin\omega)(1+\tfrac{2}{3}(\sin\tfrac{\omega}{2})^2+\tfrac{8}{15}(\sin\tfrac{\omega}{2})^4) \\ &\text{etc. ,} \end{aligned} \tag{13}$$

with a closed form expression for arbitrary orders given originally in [24]; see also [10], page 41. If we use an initial condition for (11) that, at locations $x = k$ integer, is described by

$$u(k,0) = \int_0^\pi \widehat{u}(\omega)\ \cos\omega k\ d\omega\ ,$$

for some function $\widehat{u}(\omega)$, the analytic-in-time FD solution at time t (again at the locations $x = k$ integer) becomes

$$u(k,t) = \int_0^\pi \widehat{u}(\omega)\ \cos(\omega k - f(\omega)\ t)\ d\omega\ .$$

If we also want to 'translate away' the unit-speed sideways shift of perfectly traveling waves, so that we only see the dispersive influence of the spatial approximations, we need only modify this relation to

$$u(k,t) = \int_0^\pi \widehat{u}(\omega)\ \cos(\omega k + (\omega - f(\omega))\ t)\ d\omega\ . \tag{14}$$

In the case of a narrow Gaussian initial bell, direct numerical evaluation of this integral produces the solutions shown in Figure 12. It is clear that the low order FD2 method looses its accuracy almost immediately whereas the higher order FD methods manage to keep somewhat more of the pulse integrity over longer times. However, a severe dispersive trailing wave train develops in all cases.

5.2 Dispersive errors in case of 1-D RBF approximations

Figures for RBF approximations, corresponding to Figure 11 for FD approximations, were presented in [11]. For $\varepsilon \to 0$, the curves were seen to rapidly approach the ideal PS straight line case. In the case of IQ RBF, the counterpart to (13) was found to take a particularly simple form

$$f_{IQ}(\omega) = \omega\ -\ \frac{\pi\ \sinh\frac{\omega}{\varepsilon}}{\sinh\frac{\pi}{\varepsilon}\ \cosh\frac{\pi-\omega}{\varepsilon}}\ . \tag{15}$$

For the same test cases as illustrated for FD methods in Figure 12, again by numerically evaluating (14), we obtain for IQ RBF the results seen in Figure 13. While a large value of ε is somewhat acceptable at short times, high long-term accuracy is very clearly seen to benefit from smaller values of ε. Although the RBF scheme is spectrally accurate (as the node density is increased) for all values of ε, these solution pictures for fixed $h = 1$ and different ε are nevertheless reminiscent of the ones for increasing order FD schemes (Figure 12). This is because of the similarities just described in how the eigenvalues of the derivative approximations vary with the Fourier frequency.

We will next carry the analysis of Sections 5.1 and 5.2 over to the case of RBF nodes scattered over the surface of a unit-sized sphere.

5.3 Dispersive errors in case of convection over the sphere

In this geometry, SPH modes $Y_\mu^\nu(\underline{x})$, $\mu \le \mu_{\max}$, $\nu = -\nu, \ldots, -1, 0, 1, \ldots, \nu$, form a counterpart to a truncated set of Fourier modes in a periodic 1-D case. Some low modes (up to $\mu_{\max} = 4$) are illustrated in Figure 14.

As we have already noted, when the spatial operator in (5) is approximated based on (1) or, if needed, instead by (3) or (4), all the DM's eigenvalues will be purely imaginary. From [14], we know that, as $\varepsilon \to 0$, the space spanned by $n = \mu_{\max}^2$ globally smooth RBF will exactly agree with the SPH space for $\mu \le \mu_{\max}$. We can now add to these observations that, in this limit of $\varepsilon \to 0$, the $n = \mu_{\max}^2$ RBF DM eigenvalues will approach

$$\begin{array}{lll} \mu_{\max} + 1 \text{ eigenvalues } 0 & & \\ \mu_{\max} \quad \text{eigenvalues } +i & \text{and equally many} & -i \\ \mu_{\max} - 1 \text{ eigenvalues } +2i & \text{and equally many} & -2i\,. \\ \vdots & & \\ 1 \quad \text{eigenvalue } +\mu i & \text{and also one eigenvalue} & -\mu i \end{array} \tag{16}$$

This can be deduced from two further observations:

(1) Truncated SPH expansions form a closed set with respect to any coordinate system rotation, making a result such as this independent on the value of α in (5)
(2) For $\alpha = 0$, an inspection of the patterns seen in Figure 14 shows that the $\mu_{\max} + 1$ functions in the center column ($\nu = 0$) are unaffected by any rotation around the polar axis (leading to $\mu_{\max} + 1$ eigenvalues 0); the $\mu_{\max}$ functions for $\nu = +1$ and likewise for $\nu = -1$ repeat themselves

after one revolution; the next group after 1/2 revolution, then after 1/3 revolution, etc.

Keeping $\alpha = 0$ and, to make the graphics less cluttered, choosing $\mu_{\max} = 23$ with $n = \mu_{\max}^2 = 529$ (rather than, as elsewhere this study, $n = \mu_{\max}^2 = 1849$), the eigenvalues, as functions of the SPH parameters μ and ν in the case of $\varepsilon = 0$ thus become as shown graphically in Figure 15. This flat triangular section of a plane corresponds to the PS straight line in Figure 11 and the similar straight line for $\varepsilon = 0$ in Figures 4.2 and 4.3 in the reference [11]. Raising ε from zero will cause deviations from the ideal eigenvalue pattern displayed in Figure 15. Figure 16 a displays in a different way than in Figure 11 how the eigenvalues in the 1-D FD case vary with the order p of the FD schemes. Their extent along the imaginary axis decreases by a factor of π when we move from $p = \infty$ (PS) to $p = 2$.

Figure 16 b shows similarly how the SPH ($\varepsilon = 0$) eigenvalues, seen previously in Figure 15, change as ε is increased from zero. In the left column, we see (according to (16)) only $2 \cdot 23 + 1 = 47$ distinct eigenvalues (out of a total of $n = 529$ eigenvalues). As ε increases, the largest eigenvalues decrease the fastest, leaving the lowest ones unchanged the longest. The 'corruption' of increasingly many eigenvalues in the RBF sphere case as ε increases is very reminiscent of how the same occurs in the 1-D equispaced case when the FD order is brought down from infinite (PS) to low order. The range of eigenvalues in these different cases will next be used to explore the time step restrictions that will need to be met for explicit time stepping methods.

5.4 Time stepping stability condition in 1-D

In the equispaced 1-D case of (11) with $\frac{\partial u}{\partial x}$ approximated by centered FD approximation of order p, the time stepping stability condition is that the eigenvalues of the spatial operator, described by $if(\omega)$ and graphically illustrated for $p = 2, 4, 6, 20, 120$ in Figures 11 and 16 a, fall within the time stepping methods stability domain, defined as usual in a complex $\xi = \lambda k$ domain, where the time stepping scheme is applied to $u_t = \lambda u$ with the time step k. For example, if we use leap-frog (LF) in time (which features as its

stability domain the line section between $\xi = +i$ and $\xi = -i$), we get

FD method	Condition on k/h
FD2	< 1
FD4	< 0.7287
FD6	< 0.6305
...	...
PS	$< \frac{1}{\pi} \approx 0.3183$

The maximum permissible values of k/h can be read off directly from the (inverse of the) maximum values of the corresponding curves in Figure 11, which in turn corresponds to the heights of the columns in Figure 16 a. For the LF-FD2 case, the actual stability condition thus exactly matches the result imposed by the CFL (Courant-Friedrichs-Levy) condition. As the order of spatial accuracy is increased from 2 to ∞, the actual stability condition becomes more restrictive by a factor of π (whereas the CFL condition becomes less sharp and fails to rule out increasingly long time steps).

Using (15) in place of (13), we get similar conditions on k/h (strictly valid only in our present case of $h = 1$; for details about an additional type of h-influence, see [11]):

IQ RBF	Condition on k/h
$\varepsilon = 1$	< 0.6997
$\varepsilon = 0.5$	< 0.4771
$\varepsilon = 0.2$	< 0.3803
...	...
$\varepsilon = 0$ (PS)	$< \frac{1}{\pi} \approx 0.3183$

The PS limit occurs in both cases (as FD order $\to \infty$ or in RBF cases as $\varepsilon \to 0$, respectively). With regard to these stability conditions, there are only very minor differences between the smooth RBF types.

5.5 Time stepping stability condition on the sphere

On the sphere, we can see from the results in Figure 16 b how the extent of the purely imaginary eigenvalue spectrum varies with ε. As we move from

$\varepsilon = 0$ (SPH) to $\varepsilon \approx 1$, the spectrum shrinks by less than 10%. Importantly - and in contrast with for example spectral elements or Chebyshev-type spectral methods - there are no spurious eigenvales further out in the complex plane than where the actual physical eigenvalues are located. The estimate below is made based on $\varepsilon = 0$. Scattering $n = \mu^2$ points on the sphere, we see from (16) that the largest eigenvalue is $\mu = n^{1/2}$ in magnitude. With any type of near-uniform (locally hexagonal-like) node distribution, the distance between adjacent nodes (for $n = \mu^2$ large) becomes approximately $h = \left(\frac{8\pi}{n\sqrt{3}}\right)^{1/2}$, i.e. with LF time stepping, we would need to use

$$\frac{k}{h} < \left(\frac{\sqrt{3}}{8\pi}\right)^{1/2} \approx 0.2625 \quad . \tag{17}$$

The longest possible stable time step for any ε-value on the sphere is thus not much different from the one in the case of PS for 1-D equispaced nodes, when expressed in terms of the ratio k/h. This could have been expected since, in both test problems, the maximal physical velocity is unity and no spurious eigenvalues are present. If one uses, say, RK4 in place of LF, all the stability conditions get multiplied by $2\sqrt{2}$, i.e. for $\varepsilon = 0$ we get in 1-D $k/h < 0.9003$ and on the sphere $k/h < 0.7425$.

6 Summary and Conclusions

6.1 Background to present work

The recent work by Flyer and Wright [7] clearly demonstrated some key strengths of RBF methods for solving convective-type PDEs over spherical geometries. These PDEs are particularly challenging computationally because any inaccuracies that are introduced will not only persist but will also accumulate indefinitely. At the same time, these PDEs are very important in many geophysical applications in which convection strongly dominates over dissipation. For the model problem (5), the work in [7] was limited to GA RBF with $\varepsilon \gtrsim 1$ and the only integration time that was considered was one full revolution, in our notation $t = 2\pi \approx 6.28$. In this particular case, our corresponding result can be represented as seen in Figure 17, which can be used to fill the empty bottom right subplot space in Figure 1. We have otherwise in this work avoided showing errors at times that correspond to an exact integer number of revolutions. This is because measuring the error as we are doing it (at node points only) would then always give zero convection errors in case of $\varepsilon = 0$, and thus might be misleadingly good also for low values of ε. However, the fact that we always start with a least square approximation means that the errors we show nevertheless are a good measure.

We have in the present work extended the earlier calculation in three aspects:

- Tested with a large number of different types of radial functions,
- Computed stably for ε-values all the way down to $\varepsilon = 0$,
- Presented results at both short ($t = 10$) and long ($t = 10,000$) times, in order to contrast time scales appropriate for weather and for climate modeling, respectively.

6.2 Main Conclusions

It follows both from the present numerical results and from the accompanying analysis that very long time integrations are completely feasible with the RBF approach, but that the shape parameter ε then will need to be kept quite low, especially when integration times increase (typically bringing the computations out of reach for the RBF-Direct approach when using standard 16 digit double precision arithmetic). All of the smooth RBF give virtually the same accuracy, whereas the piecewise smooth ones are not at all competitive in the present context.

These general results just mentioned follow from properties of the DMs, i.e. they are not influenced by the smoothness of the convected solution. This observation is similar to the one for PS vs. FD methods, as described in [10], Section 4.2, where it was shown that PS and high order FD methods were much better than low order FD methods, even when convecting a step function. In case of interpolation (rather than long-time advection), the situation is quite different and there will in that application probably be little point using basis functions that are much smoother than the data they are applied to.

At $n = 1849$ nodes (as used in all the calculations in the present study), it so happened that RBF-Direct just barely (with the perfect choice of ε) could reach the error level that RBF-QR featured for all sufficiently small ε. It is at present unclear whether this will remain the case if n is increased further.

It follows from the RBF-QR algorithm that $\varepsilon \to 0$ with globally smooth RBF leads to the same results as using SPH basis functions. One might therefore ask why not just use SPH as a computational basis on the sphere (as has often been done in the past). There are however several reasons in favor of an RBF approach:

- The limit $\varepsilon \to 0$ is not always the best parameter choice.
- RBFs can combine spectral accuracy with local refinement wherever this is needed (cf. discussion in [17]); SPH offer no such opportunities.
- RBF non-singularity is guaranteed whenever $\varepsilon > 0$, but not for all node sets

if $\varepsilon = 0$.

- Typical SPH-PS implementations require conversions between SPH and node values on some dense grid at every time step.
- RBF codes are algebraically far less complex than SPH codes (even when implemented by means of the RBF-QR method; cf. the Appendix in [14]).

The main present concern about RBF-based methods stems from their global character, and the associated cost of full matrix×vector multiplications at each time step. Although this task is well suited for massively parallel processing, it would nevertheless be desirable to be able to effectively apply either 'fast' (iterative) algorithms, or domain decomposition. Both these avenues have seen significant progress in recent years, but will not be surveyed here.

7 Appendix A: Construction of the DM with RBF-QR

The key step in the RBF-QR algorithm, as described in [14], is that a column vector containing the original RBF basis functions can be rewritten as a certain matrix product times another column vector that contains SPH functions:

$$\begin{bmatrix} \phi(\|\underline{x} - \underline{x}_1\|) \\ \phi(\|\underline{x} - \underline{x}_2\|) \\ \vdots \\ \phi(\|\underline{x} - \underline{x}_n\|) \end{bmatrix} = \begin{bmatrix} \\ Q \\ \\ \end{bmatrix} \begin{bmatrix} \\ E \\ \\ \end{bmatrix} \begin{bmatrix} \\ R \\ \\ \end{bmatrix} \begin{bmatrix} \\ \\ \underline{y}_1(\underline{x}) \\ \\ \\ \end{bmatrix}.$$

Here Q is unitary, E is diagonal (with entries that are increasingly high powers of ε), and R (with more columns than rows) is upper triangular (This equation holds to computational machine precision but not in a strict mathematical sense unless we let the number of columns in R and entries in $\underline{y}_1(\underline{x})$ be infinite). Transposing this relation gives

$$\left[\phi(\|\underline{x} - \underline{x}_1\|) \ \ldots \ \phi(\|\underline{x} - \underline{x}_n\|) \right] = (R\, \underline{y}_1(\underline{x}))^T \ E^T \ Q^T \ . \tag{18}$$

Next, applying this relation in turn to $\underline{x} = \underline{x}_1, \ldots, \underline{x} = \underline{x}_n$ and placing the resulting row vectors below each other allows us to allows us to write A (defined in (2) and (9)) as

$$A = (R\, Y_1)^T \ E^T \ Q^T.$$

All the ill-conditioning of A is now confined to the *analytically known* matrix E^T. Next we apply the differential operator L to (18) and obtain

$$\Big[\, L\phi(\|\underline{x}-\underline{x}_1\|) \;\ldots\; L\phi(\|\underline{x}-\underline{x}_n\|) \,\Big] = (R\,\underline{y}_2(\underline{x}))^T\; E^T\; Q^T$$

(where $y_2(\underline{x}) = L\; y_1(\underline{x})$) and therefore, after applying this to $\underline{x} = \underline{x}_1, \ldots, \underline{x} = \underline{x}_n$; cf. (8),

$$B = (R\; Y_2)^T\; E^T\; Q^T.$$

Because of (7), the DM then becomes

$$\begin{aligned} D = B\cdot A^{-1} &= (R\;Y_2)^T (E^TQ^T)(E^TQ^T)^{-1}((R\;Y_1)^{-1})^T \\ &= (R\;Y_2)^T((R\;Y_1)^{-1})^T = ((R\;Y_1)^{-1}(R\;Y_2))^T \end{aligned} \quad .$$

Computing D by means of the last expression above has avoided all the ill-conditioning even as $\varepsilon \to 0$ (eliminated through our *analytic* knowledge that $(E^TQ^T)(E^TQ^T)^{-1} = I$).

8 Appendix B: The RBF-QR method in the case of Wendland functions

Hubbert and Baxter [20] noted that RBFs, when centered at an arbitrary location $\underline{x}_i$ on the unit sphere, can be expanded in terms of SPH as

$$\phi(\|\underline{x}-\underline{x}_i\|) = \sum_{\mu=0}^{\infty} \sum_{\nu=-\mu}^{\mu}{}' \{c_\mu\; Y_\mu{}^\nu(\underline{x}_i)\}\; Y_\mu{}^\nu(\underline{x}) \tag{19}$$

where

$$c_\mu = \frac{\pi}{2^{k-1}k!}\int_{-1}^{1}(1-t^2)^k \frac{d^k}{dt^k}\phi\left(\sqrt{2-2t}\right) dt\;. \tag{20}$$

They also gave explicit formulas for the coefficients c_μ in several cases, such as MQ, IMQ and GA. A formula for IQ was given in [14]. In these formulas, the potentially dangerous ε-dependence of the radial functions $\phi(\|\underline{x}-\underline{x}_i\|)$ takes the simple form of explicit high powers of ε in the coefficients, thereby permitting their analytic elimination in the RBF-QR algorithm. Typical examples include

$$\begin{aligned} &\text{MQ:}\;\; c_\mu = -\varepsilon^{2\mu}\; \tfrac{2\pi(2\varepsilon^2+1+(\mu+1/2)\sqrt{1+4\varepsilon^2})}{(\mu+3/2)(\mu+1/2)(\mu-1/2)} \left(\tfrac{2}{1+\sqrt{4\varepsilon^2+1}}\right)^{2\mu+1} \\ &\text{IMQ:}\; c_\mu = \varepsilon^{2\mu}\; \tfrac{4\pi}{(\mu+1/2)} \left(\tfrac{2}{1+\sqrt{4\varepsilon^2+1}}\right)^{2\mu+1} \end{aligned}$$

Since expansions of the type (19) have not previously been given in the case of the Wendland radial functions, and these functions' limited smoothness causes

some difficulties in the RBF-QR algorithm, we give below some comments on these issues. The Wendland function W2 of order 2 can be written as

$$\phi(r) = \begin{cases} (1-\varepsilon r)^4(4\varepsilon r+1) & \text{if} \quad r < \frac{1}{\varepsilon} \\ 0 & \text{if} \quad r \geq \frac{1}{\varepsilon} \end{cases}$$

Since we are interested in these expansions (19) only for for small ε (in order to apply the RBF-QR algorithm), we assume $\varepsilon < \frac{1}{2}$. The Wendland functions on the sphere are then no longer of compact support, and the formula for W2 simplifies to

$$\phi(r) = (1-\varepsilon r)^4(4\varepsilon r+1)\ .$$

Straightforward application of (20) now gives

$$\begin{cases} c_0 = 4\pi(2 - 40\varepsilon^2 + 128\varepsilon^3 - 160\varepsilon^4 + \frac{512}{7}\varepsilon^5) \\ c_1 = \varepsilon^2\ \frac{32}{63}\pi(105 - 432\varepsilon + 630\varepsilon^2 - 320\varepsilon^3) \\ c_2 = \varepsilon^3\ \frac{64}{231}\pi(88 - 231\varepsilon + 160\varepsilon^2) \\ c_k = \varepsilon^3\ \frac{45\cdot 2^9\pi((2k-5)(2k+7)-20\varepsilon^2)}{(2k+7)(4k^2-1)(4k^2-9)(4k^2-25)} \qquad\qquad k = 3,4,... \end{cases}$$

The expansions for W4 and W6 are easily found in a similar way, but are more lengthy and will not be explicitely given here. The fact that the expansion coefficients c_k for the smooth radial functions go to zero like $O(\varepsilon^{2k})$ is utilized in the RBF-QR algorithm. In the W2-case, c_k remains of size $O(\varepsilon^3)$ for $k = 3,4,...$, and the RBF-QR method requires a minor modification. At the key stage in that algorithm (Section 3.5 in [14]), we have now instead

$$\begin{bmatrix} \phi(\|\underline{x}-\underline{x}_1\|) \\ \phi(\|\underline{x}-\underline{x}_2\|) \\ \vdots \\ \phi(\|\underline{x}-\underline{x}_n\|) \end{bmatrix} = \begin{bmatrix} \overbrace{\frac{c_{0,\varepsilon}}{2}Y_0^0(\underline{x}_1)}^{O(1)} & \overbrace{\frac{c_{1,\varepsilon}}{1}Y_1^{-1}(\underline{x}_1) & \frac{c_{1,\varepsilon}}{2}Y_1^0(\underline{x}_1) & \frac{c_{1,\varepsilon}}{1}Y_1^1(\underline{x}_1)}^{O(\varepsilon^2)} & \overbrace{....}^{O(\varepsilon^3)} \\ \frac{c_{0,\varepsilon}}{2}Y_0^0(\underline{x}_2) & \frac{c_{1,\varepsilon}}{1}Y_1^{-1}(\underline{x}_2) & \frac{c_{1,\varepsilon}}{2}Y_1^0(\underline{x}_2) & \frac{c_{1,\varepsilon}}{1}Y_1^1(\underline{x}_2) & .... \\ ... & ... & ... & ... & .... \\ \frac{c_{0,\varepsilon}}{2}Y_0^0(\underline{x}_n) & \frac{c_{1,\varepsilon}}{1}Y_1^{-1}(\underline{x}_n) & \frac{c_{1,\varepsilon}}{2}Y_1^0(\underline{x}_n) & \frac{c_{1,\varepsilon}}{1}Y_1^1(\underline{x}_n) & .... \end{bmatrix} \begin{bmatrix} Y_0^0(\underline{x}) \\ Y_1^{-1}(\underline{x}) \\ Y_1^0(\underline{x}) \\ Y_1^1(\underline{x}) \\ Y_2^{-2}(\underline{x}) \\ Y_2^{-1}(\underline{x}) \\ \vdots \end{bmatrix}$$

$$= B \cdot Y$$

QR factorization of B gives

$$
\begin{aligned}
B = &\begin{bmatrix} & & \\ & Q & \\ & & \end{bmatrix}
\begin{bmatrix}
1 & & & & & & \\
& \varepsilon^2 & & & & & \\
& & \varepsilon^2 & & & & \\
& & & \varepsilon^2 & & & \\
& & & & \varepsilon^3 & & \\
& & & & & \ddots &
\end{bmatrix} \times \\
\times &\begin{bmatrix}
* & . & . & . & . & . & . & . & . & . & . & . & \dots \\
& * & * & * & . & . & . & . & . & . & . & . & \dots \\
& & * & * & . & . & . & . & . & . & . & . & \dots \\
& & & * & . & . & . & . & . & . & . & . & \dots \\
& & & & * & * & * & * & * & * & * & * & \dots \\
& & & & & \ddots & \dots & \dots & \dots & \dots & \dots & \dots & \dots & \dots
\end{bmatrix} \\
= &\, Q \cdot E \cdot R
\end{aligned}
$$

After the fourth row, the elements of R do not contain factors of ε anymore, and these elements therefore no longer vanish when $\varepsilon \to 0$. Each row can be seen as a perturbed spherical harmonic function. The fact that the perturbation doesn't vanish as $\varepsilon \to 0$ means that the RBF interpolant no longer converges towards the SPH interpolant (as was the case with smooth RBFs). The situation is similar for all other non-smooth radial functions. This also means that the convergence of the expansion will not be sped up when $\varepsilon \to 0$, but rather will be strictly algebraic in k. We will therefore need a much larger number of terms in the expansions to attain the desired accuracy in the RBF-QR method. However, since non-smooth radial functions seldom are used near their flat limit, this may be of little practical significance.

References

[1] J.P. Boyd, Chebyshev and Fourier Spectral Methods (second edition), Dover (2001).

[2] G.L. Browning, J.J. Hack, and P.N. Swarztrauber, A comparison of three different numerical methods for solving differential equations on the sphere, Mon. Wea. Rew. 117 (1989), 1058-1075.

[3] M. Buhmann, Radial Basis Functions, Cambridge University Press, Cambridge (2003).

[4] M. Buhmann, M.D. and Dyn, N., Spectral convergence of multiquadric interpolation. Proc. Edinburgh Math. Soc. 36 (1993), 319-333.

[5] T.A. Driscoll and B. Fornberg, Interpolation in the limit of increasingly flat radial basis functions, Comp. Math. with Applications 43 (2002), 413-422.

[6] G.E. Fasshauer, Meshfree Approximation Methods with Matlab, World Scientific Publishing, Singapore (2007)

[7] N. Flyer and G. Wright, Transport schemes on a sphere using radial basis functions, Journal of Computational Physics. 226 (2007), 1059-1084.

[8] N. Flyer and G. Wright, Solving the nonlinear shallow water wave equations using radial basis functions, to be submitted.

[9] B. Fornberg, On a Fourier method for the integration of hyperbolic equations, SIAM J. Numer. Anal. 12 vol 4 (1975), 509-528.

[10] B. Fornberg, A Practical Guide to Pseudospectral Methods, Cambridge University Press, Cambridge (1996).

[11] B. Fornberg and Flyer, N., Accuracy of radial basis function interpolation and derivative approximations on 1-D infinite grids, Advances in Computational Mathematics 23 (2005), 5-20.

[12] B. Fornberg, E. Larsson and G. Wright, A new class of oscillatory radial basis functions, Computers and Mathematics with Applications 51 (2006), 1209-1222.

[13] B. Fornberg and D. Merrill, Comparison of finite difference and pseudospectral methods for convective flow over a sphere, Geophys. Res. Lett. 24 (1997), 3245-3248.

[14] B. Fornberg and C. Piret, A stable algorithm for flat radial basis functions on a sphere, to appear in SIAM J. Sci. Comp.

[15] B. Fornberg and G. Wright, Stable computation of multiquadric interpolants for all values of the shape parameter, Comp. Math. with Applications 48 (2004), 853-867.

[16] B. Fornberg, G. Wright and E. Larsson, Some observations regarding interpolants in the limit of flat radial basis functions, Comp. Math. with Applications 47 (2004), 37-55.

[17] B. Fornberg and J. Zuev, The Runge phenomenon and spatially variable shape parameters in RBF interpolation, Comp. Math. with Applications 54 (2007), 379-398.

[18] F.X. Giraldo and T.E. Rosmond, A scalable spectral element Eulerian atmospheric model (SEE-AM) for NWP: Dynamical core tests, Monthly Weather Review, 132 (2004), 133–153.

[19] J.J. Hack and R. Jakob, Description of a global shallow water model based on the spectral transform method, NCAR Technical Note TN 343 STR (1992).

[20] S. Hubbert and B. Baxter, Radial basis functions for the sphere, Progress in Multivariate Approximation, Volume 137 of the International Series of Numerical Mathematics, Birkhauser, (2001) 33-47.

[21] R. Jakob-Chien, J.J. Hack and D.L. Williamson, Spectral transform solutions to the shallow water test set, J. Comp. Phys. 119 (1995), 164-187.

[22] E.J. Kansa, Multiquadrics - A scattered data approximation scheme with applications to computational fluid-dynamics. I. Surface approximations and partial derivative estimates, Comput. Math. Appl. 19 (8/9) (1990), 127-145.

[23] E.J. Kansa, Multiquadrics - A scattered data approximation scheme with applications to computational fluid-dynamics. II. Solutions to parabolic, hyperbolic and elliptic partial differential equations, Comput. Math. Appl. 19 (8/9) (1990), 147-161.

[24] H.-O. Kreiss and J. Oliger, Comparison of accurate methods for the integration of hyperbolic equations, Tellus 24 (1972), 199-215.

[25] E. Larsson and B. Fornberg, A numerical study of radial basis function based solution methods for elliptic PDEs, Comp. Math. Applic. 46 (2003), 891-902.

[26] E. Larsson and B. Fornberg, Theoretical and computational aspects of multivariate interpolation with increasingly flat radial basis functions, Comp. Math. Applic. 49 (2005), 103-130.

[27] E. Larsson and B. Fornberg, A stable algorithm for flat radial basis functions, to be submitted.

[28] W.R. Madych and S.A. Nelson, Bounds on multivariate polynomials and exponential error estimates for multiquadric interpolation, J. Approx. Theory 70 (1992), 94-114.

[29] P.E. Merilees, The pseudospectral approximation applied to the shallow water equation on a sphere, Atmosphere 11 (1973), 13-20.

[30] P.E. Merilees, Numerical experiments with the pseudospectral method in spherical coordinates, Atmosphere 12 (1974), 77-96.

[31] R.D. Nair, S.J. Thomas and R.D. Loft, A discontinuous Galerkin transport scheme on the cubed sphere. Mon. Wea. Rev. 133 (2005), 814-828.

[32] R. Platte and T.A. Driscoll, Eigenvalue stability of radial basis function discretizations for time-dependent problems, Computers Math. Appl. 51 (2006), 1251-1268.

[33] M.J.D. Powell, The theory of radial basis function approximation in 1990, in Advances in Numerical Analysis, Vol. II: Wavelets, Subdivision Algorithms and Radial Functions, W. Light, ed., Oxford University Press, Oxford (1990), 105-210.

[34] R. Schaback, Multivariate interpolation by polynomials and radial basis functions, Constr. Approx. 21 (2005), 293-317.

[35] R. Schaback and H. Wendland, Characterization and construction of radial basis functions, In Multivariate Approximation and Applications, ed. Dyn, N. et al. Cambridge University Press (2001), 1-24.

[36] W.F. Spotz, M.A. Taylor and P.N. Swarztrauber, Fast shallow water equation solvers in latitude-longitude coordinates, Journal of Computational Physics 145 (1998), 432-444.

[37] A. St-Cyr, C. Jablanowski, J.M. Dennis, H.M. Tufo and S.J. Thomas, A comparison of two shallow water models with non-conforming adaptive grids, to appear in Monthly Weather Review.

[38] P.N. Swarztrauber, Spectral transform methods for solving the shallow-water equations on the sphere, Monthly Weather Review, 124 (1996), 730–744.

[39] M. Taylor, J. Tribbia, and M. Iskandarani, The spectral element method for the shallow water equations on the sphere, Journal of Computational Physics 130 (1997), 92-108.

[40] C. Temperton, On scalar and vector transform methods for global spectral models, Mon. Wea. Rew. 119 (1991), 1303-1307.

[41] S.J. Thomas and R.D. Loft, The NCAR spectral element climate dynamical core: Semi-implicit, Eulerian formulation, J. Sci. Comp. 25 (2005), 307-322.

[42] L.N. Trefethen, Spectral Methods in Matlab, SIAM, Philadelphia (2000).

[43] H. Wendland, Scattered Data Approximation, Cambridge University Press, Cambridge (2005).

[44] D.L. Williamson, J.B. Drake, J.J. Hack, R. Jakob and P.N. Swarztrauber, A standard test set for numerical approximations to the shallow water equations in spherical geometry, J. Comput. Phys. 102 (1992), 211–224.

[45] R.S. Womersley and I. Sloan, Interpolation and cubature on the sphere, http://web.maths.unsw.edu.au/rsw/Sphere/.

[46] R.S. Womersley and I. Sloan, How good can polynomial interpolation on the sphere be?, Advances in Computational Mathematics 14 (2001), 195-226.

[47] J. Yoon, Spectral approximation orders of radial basis function interpolation on the Sobolev space, SIAM J. Math. Anal. 23 (2001), 946-958.

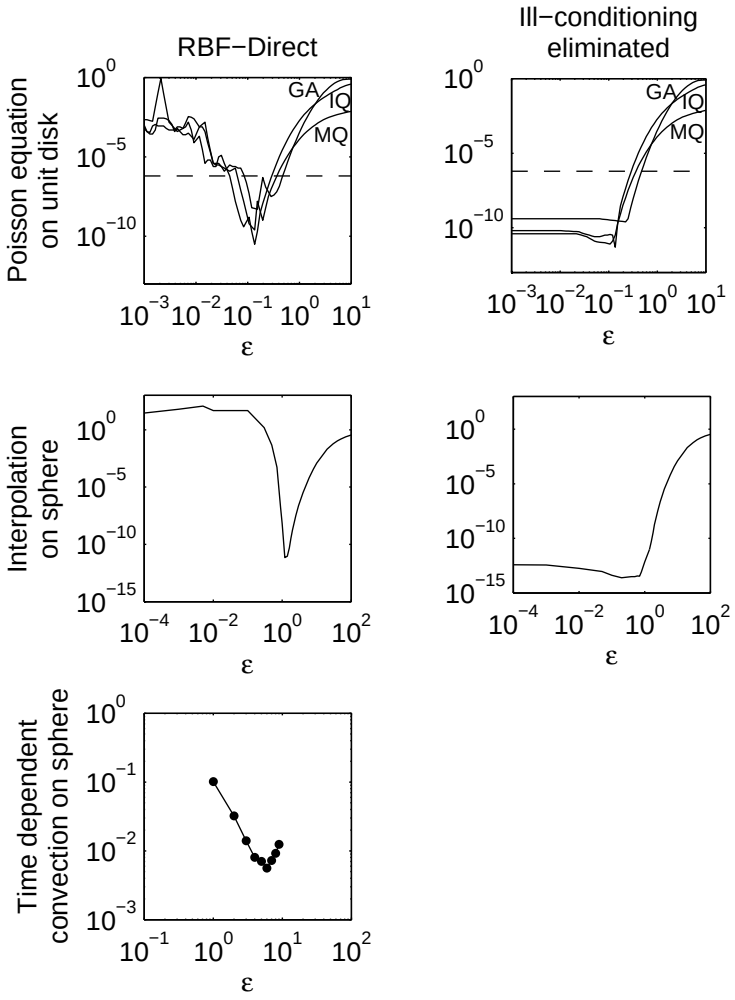

Fig. 1. RBF errors in three applications, displayed as functions of the shape parameter ε. The three rows of subplots reproduce data from [25], [14], and [7], respectively. The abbreviations MQ, IQ, GA are explained in Section 2.

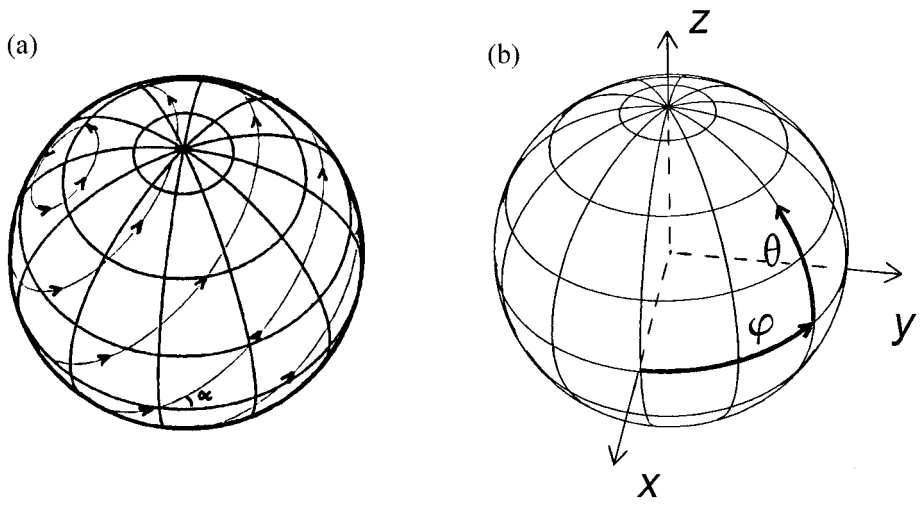

Fig. 2. (a) Flow directions in the 'solid body' convection test problem, (b) Spherical latitude-longitude-type coordinate system.

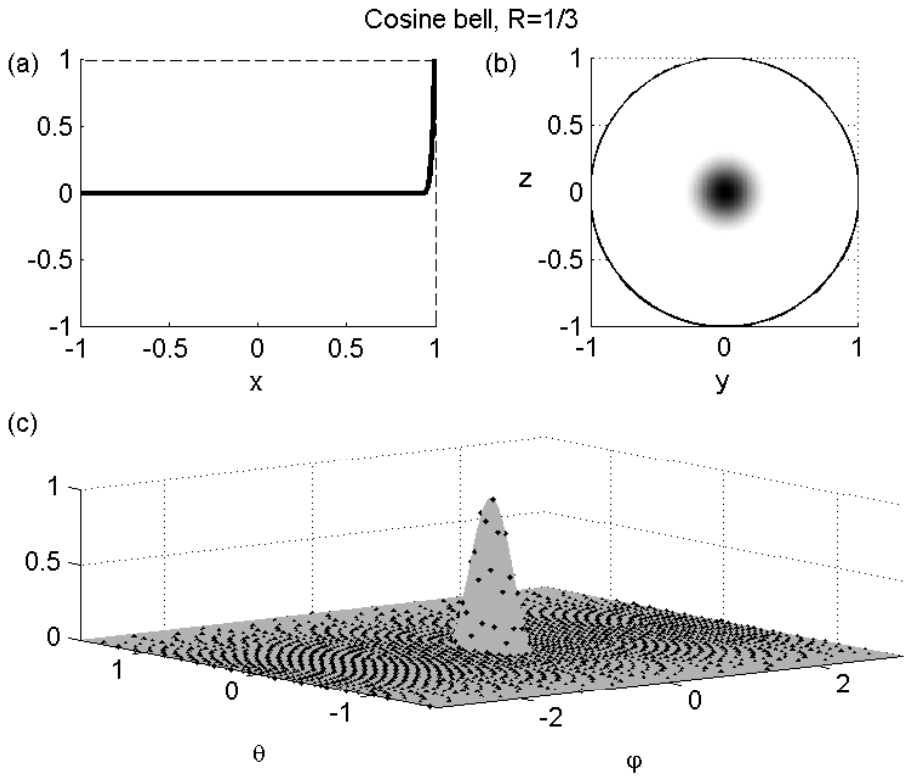

Fig. 3. Three illustrations of the cosine bell (a) as a function of x according to (6), (b) in grey-scale on sphere surface, viewed from positive x-direction, and (c) on an 'unrolled' φ, θ-plane (with the $n = 1849$ ME node locations also marked).

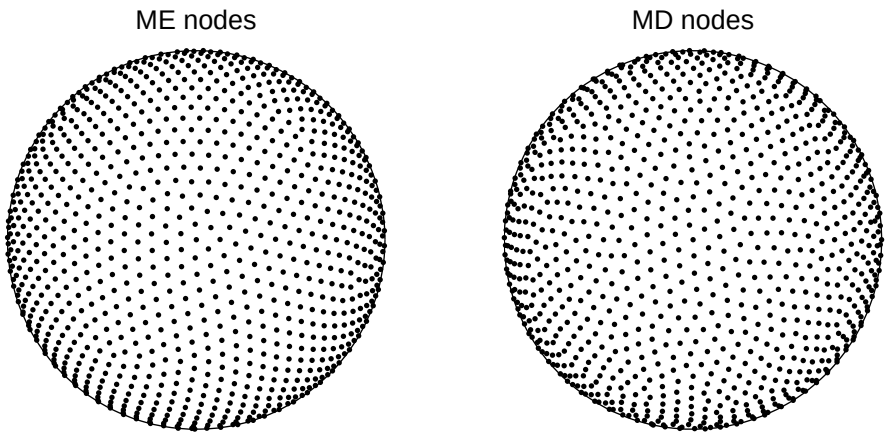

Fig. 4. Illustration of the minimal energy (ME) and maximal determinant (MD) $n = 1849$ node sets.

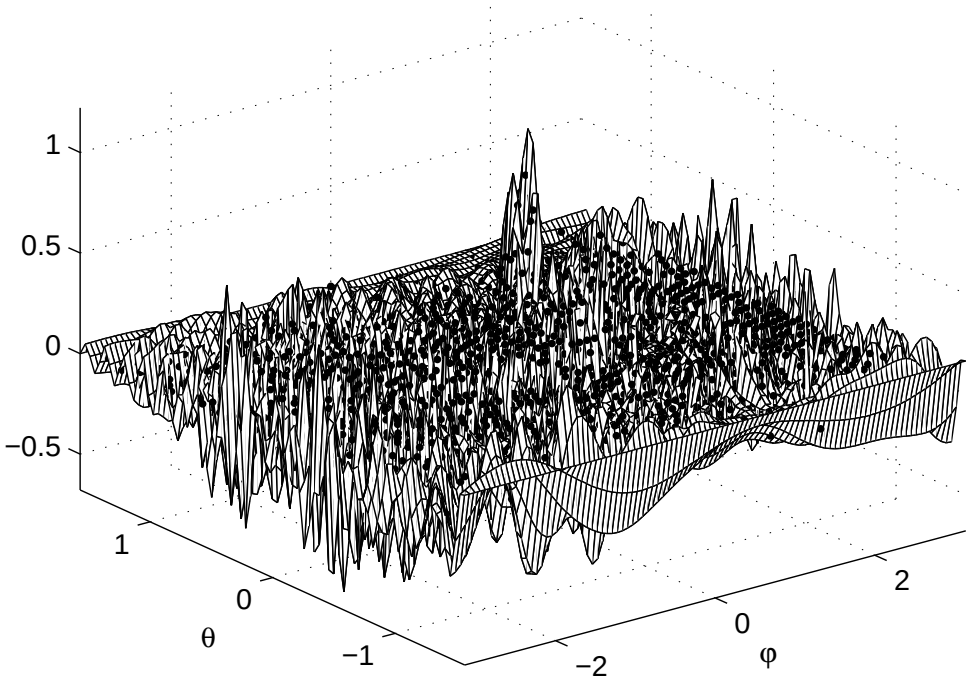

Fig. 5. The SPH interpolant to the cosine bell over the $n = 1849$ ME node points. The input data is as exactly as shown by the data points in Figure 3 c.

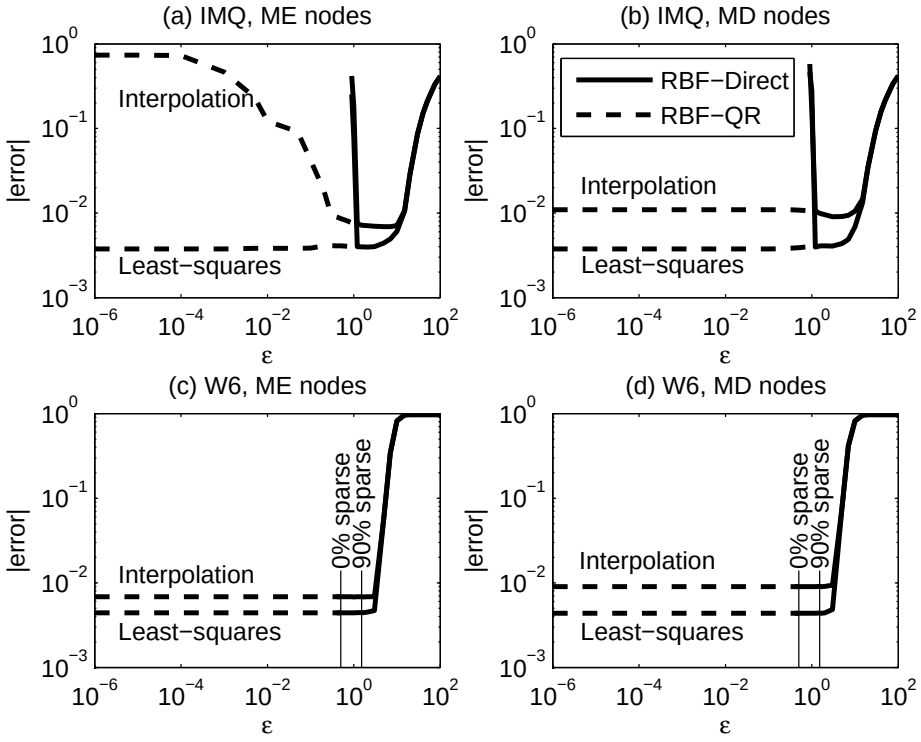

Fig. 6. The errors (in max norm) when the initial cosine bell is brought to an $n = 1849$ node RBF representation (a) IMQ on ME nodes, (b) IMQ on MD nodes, (c) W6 RBF on ME nodes, and (d) W6 on MD nodes. In the W6 cases, the ε values corresponding to 0% and 90% sparsity of the A-matrix are marked. In all cases, we contrast direct interpolation with the least square approach described in Section 3.4. We display the divergence of RBF-Direct for decreasing ε in subplots a,b (appearing as near-vertical solid lines around $\varepsilon = 1$). In subplots c,d and in the following Figures 7, 9, 10, similar divergence occurs but is not explicitly marked.

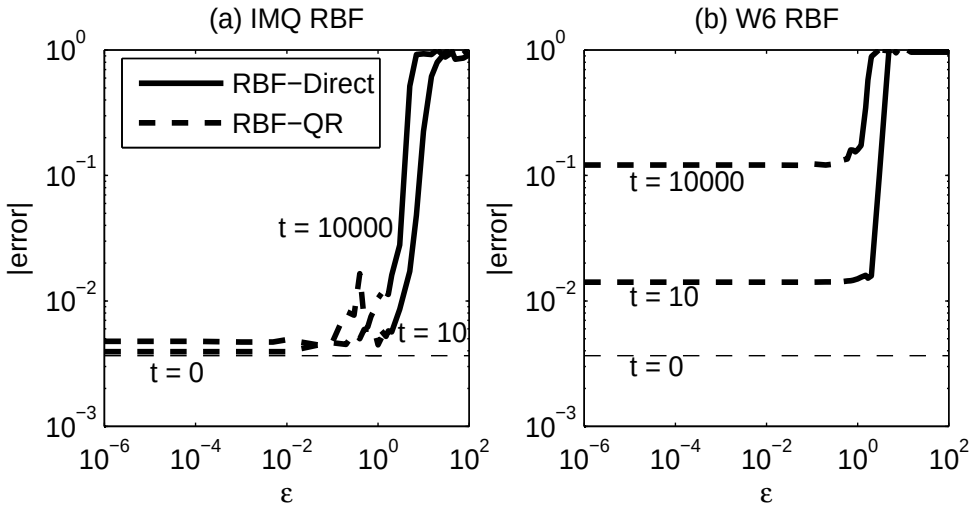

Fig. 7. Errors at times $t = 10$ and $t = 10,000$ as functions of ε in case of (a) IMQ and (b) W6. The thin dashed line shows the (ε-independent) error of the initial SPH representation of the initial data at $t = 0$.

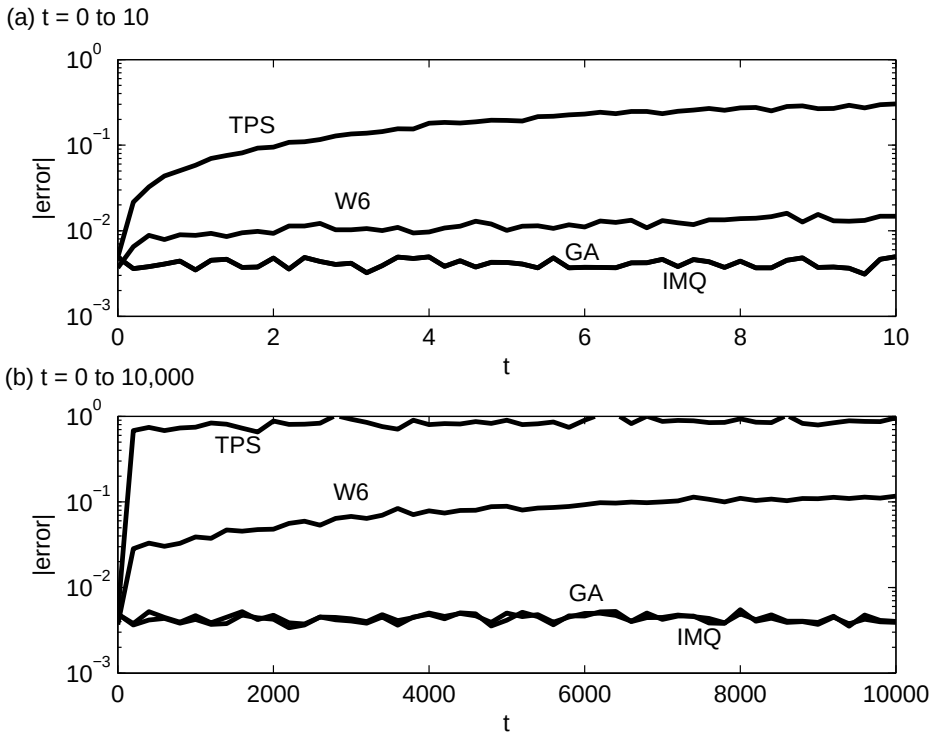

Fig. 8. Evolution of the error with time over (a) $0 \leq t \leq 10$ and (b) $0 \leq t \leq 10,000$. The ε values for IMQ, GA and W6 were near zero, whereas TPS does not include any ε.

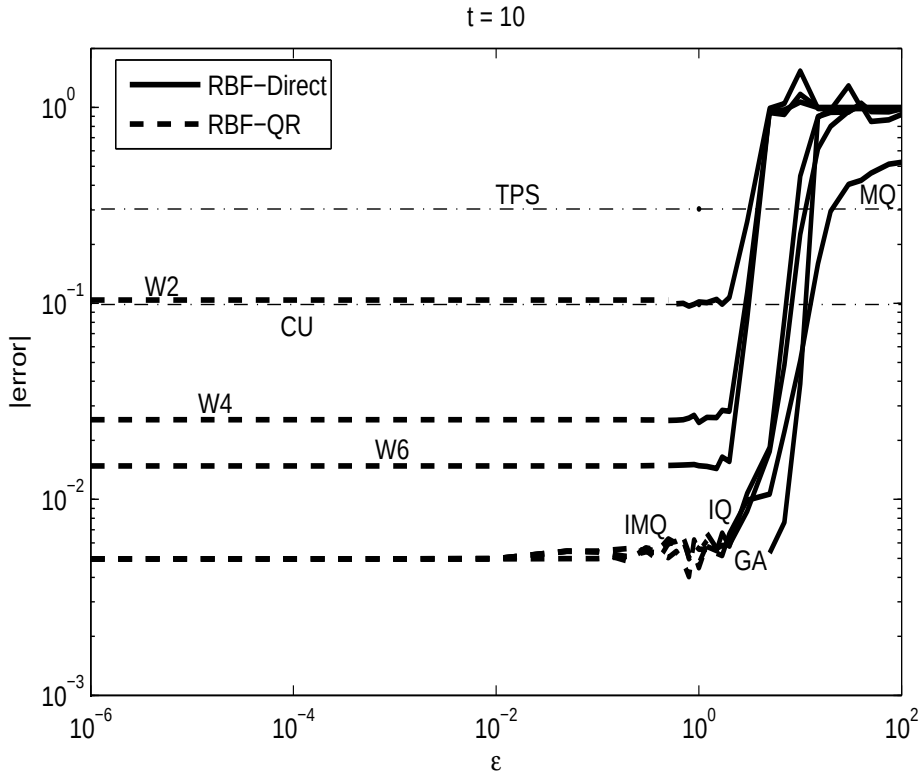

Fig. 9. The errors at $t = 10$, as functions of ε, for all the RBF choices considered in this study. In the case of GA, the ill-conditioning for RBF-Direct occurs somewhat earlier than for the other smooth RBF types, leaving a small gap (visible also in Figure 10) between the ranges of RBF-QR and RBF-Direct. For large values of ε, the MQ results are notably more accurate than those for the other RBF types (although not nearly as good as what all the smooth RBFs achieve for small ε-values).

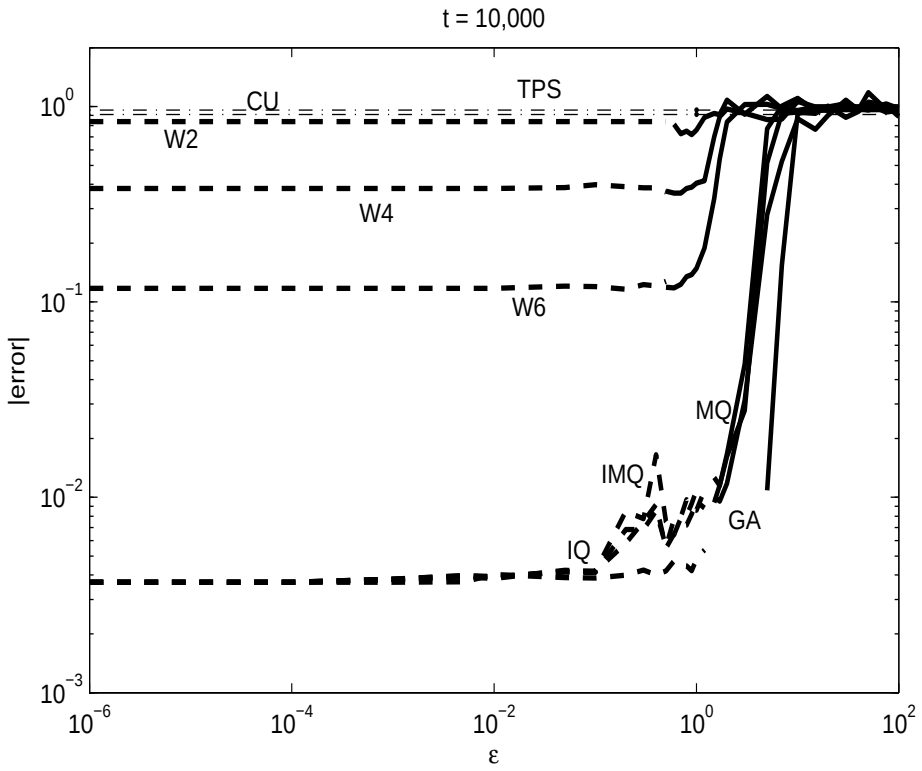

Fig. 10. The errors at $t = 10,000$, as functions of ε, for all the RBF choices considered in this study.

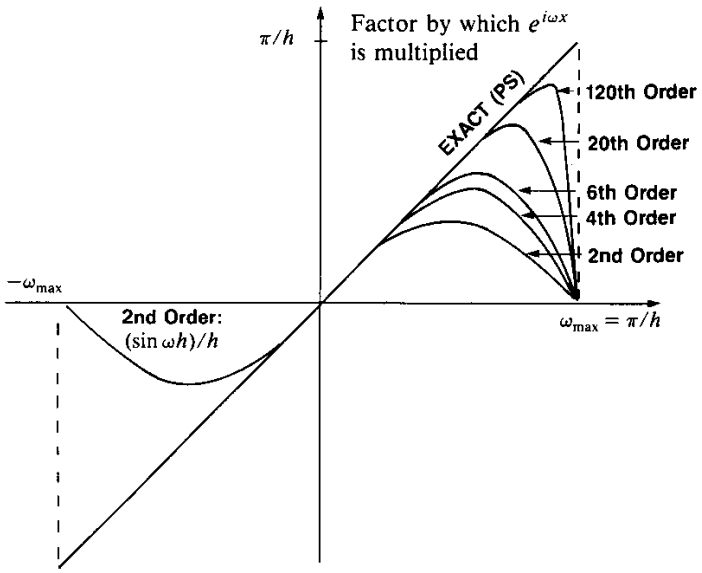

Fig. 11. Effect of $\frac{d}{dx}$ and of finite difference approximations of different orders of $\frac{d}{dx}$ when applied to a basic Fourier mode $e^{i\omega x}$. The highest mode that can be present on a grid of spacing h is denoted by $\omega_{\max} = \pi/h$ (Reproduced from [10], with permission from Cambridge University Press).

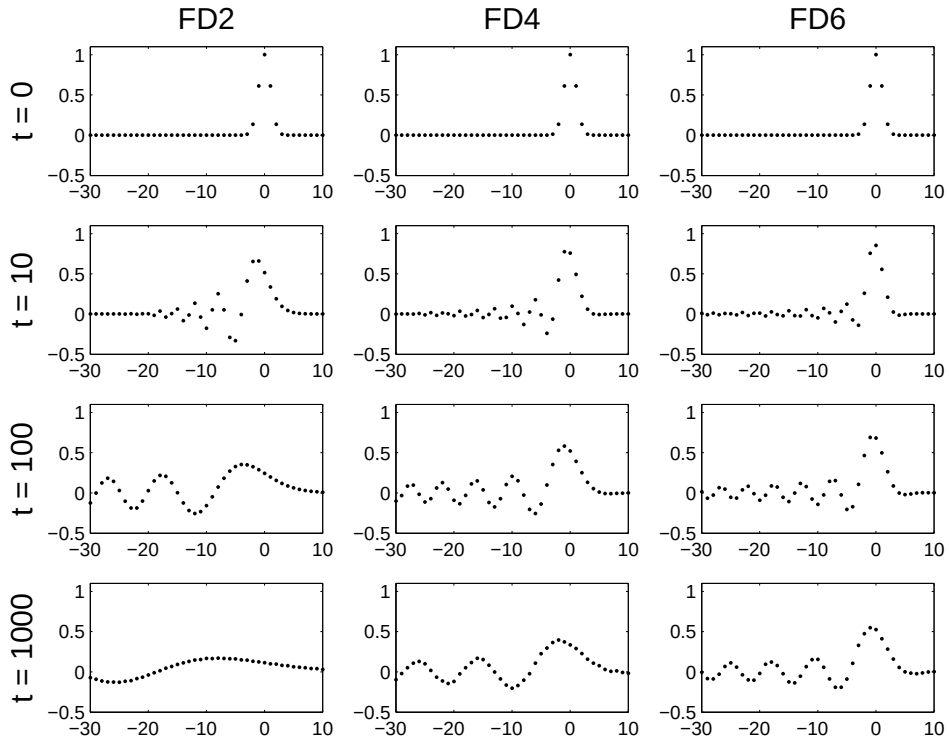

Fig. 12. The integrity of a narrow Gaussian pulse (shown as dots on a grid with $h = 1$) when integrated exactly in time, using FD2, FD4 and FD6, respectively, in space.

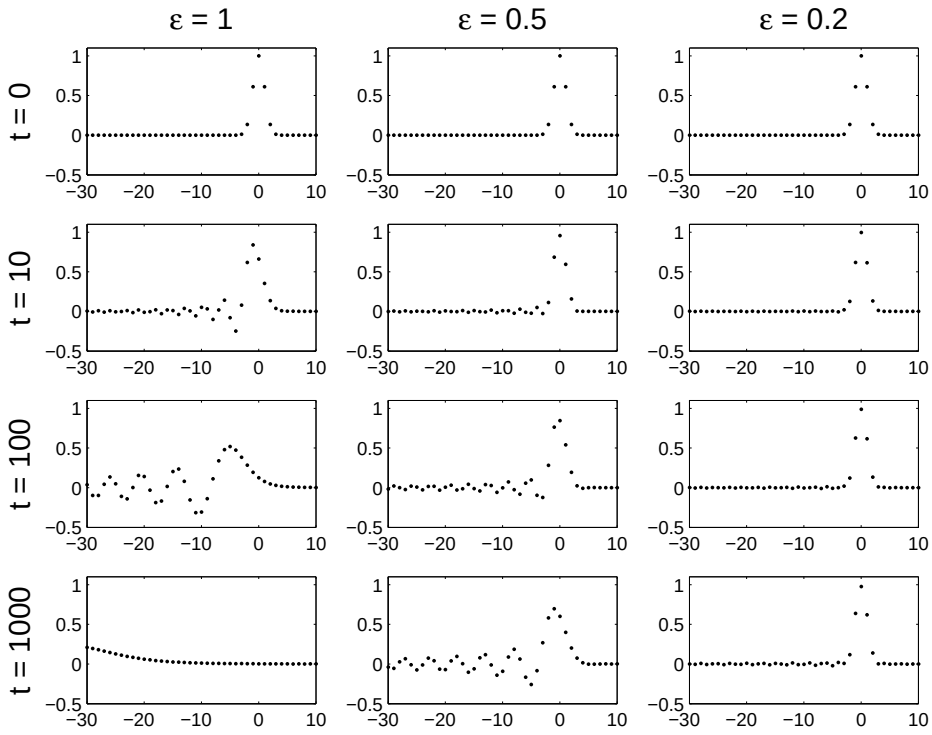

Fig. 13. Corresponding results to those in Figure 12, but using IQ RBF with different ε-values.

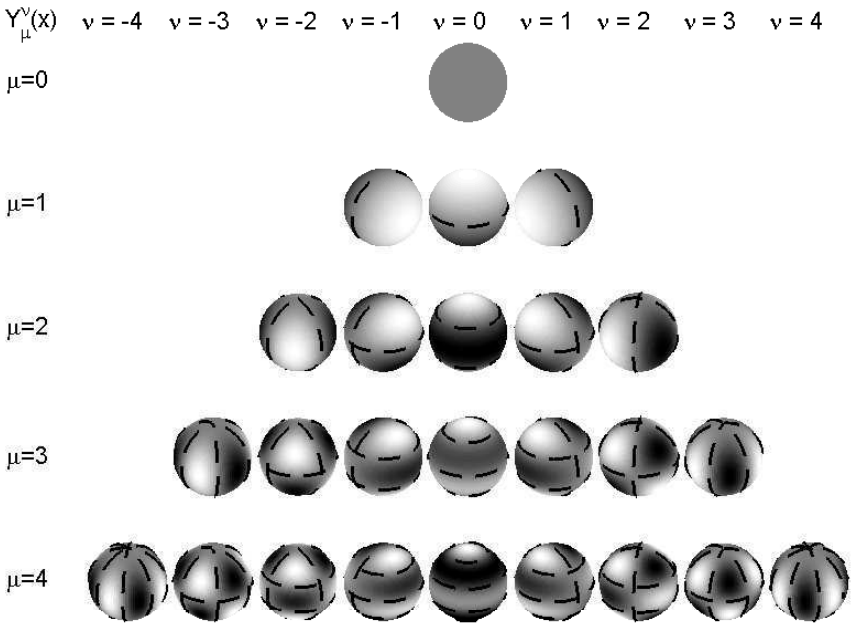

Fig. 14. Illustration of the SPH basis functions Y_μ^ν for orders $\mu \leq \mu_{\max} = 4$. The dashed lines show where they change sign.

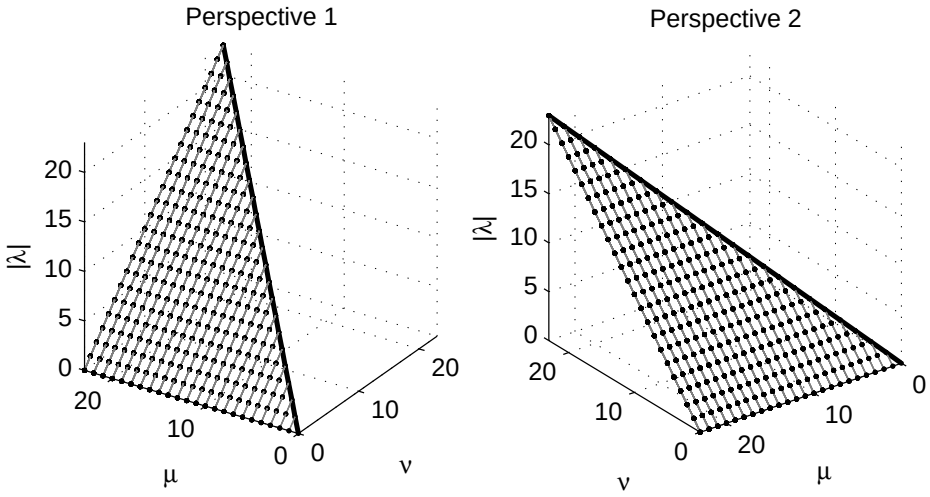

Fig. 15. The eigenvalues to the convective operator in the sphere case, computed by using IQ RBF in the $\varepsilon = 0$ limit. According to the motivation for (16), they can be associated with μ and ν-values as shown.

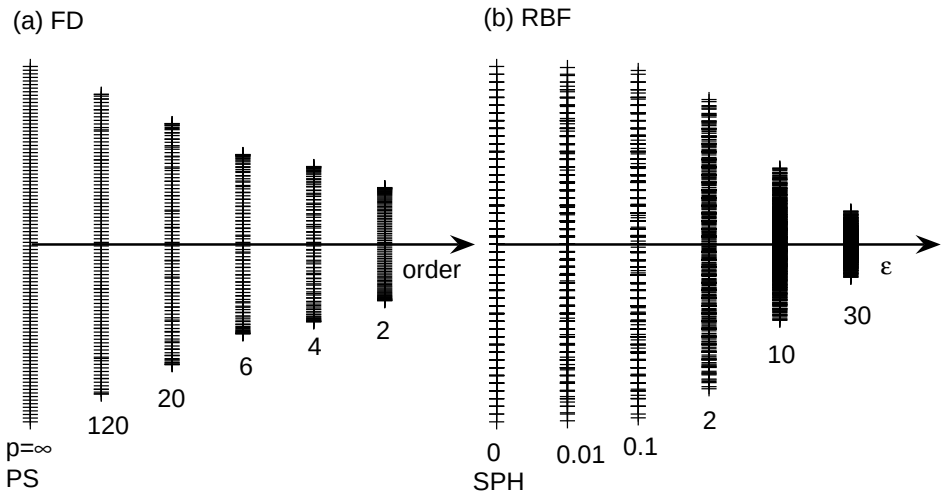

Fig. 16. (a) The $n = 51$ 1-D convection PDE eigenvalues for different orders of FD schemes in case of $h = 1$ and a periodic domain $[-25, 25]$ (rather than $[-\infty, \infty]$), (b) The $n = 529$ sphere convection problem eigenvalues for different ε-values (in the case of MQ; results for other smooth RBF types are very similar). The vertical scales are not marked since the present issue of interest is to show qualitatively how the extents in the two cases vary with FD order and with ε-value, respectively.

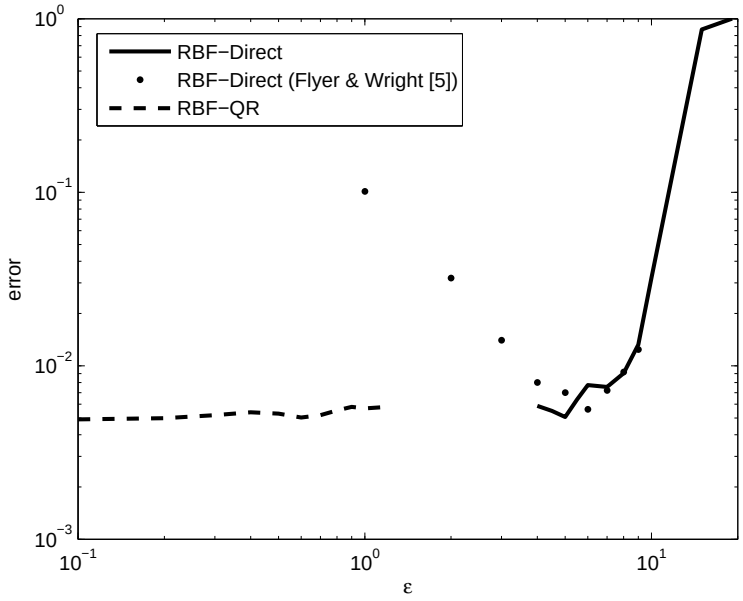

Fig. 17. Comparison between the results reported in [7] and the present ones for the test case of convecting the cosine bell one time around the sphere (GA RBF using $n = 1849$ ME nodes). The results are in close agreement for $\varepsilon \geq 3$ (where both computations vere based on RBF-Direct). RBF-QR (in this case convergent only for $\varepsilon \lesssim 1$), in combination with the least squares approach, has overcome the previously seen low-ε divergence.

Name of RBF	**Abbreviation**	**Definition**
Smooth, global		
Multiquadric	MQ	$\sqrt{1+(\varepsilon r)^2}$
Inverse multiquadric	IMQ	$\frac{1}{\sqrt{1+(\varepsilon r)^2}}$
Inverse quadratic	IQ	$\frac{1}{1+(\varepsilon r)^2}$
Gaussian	GA	$e^{-(\varepsilon r)^2}$
Piecewise smooth, global		
Cubic	CU	$\lvert r\rvert^3$
Thin plate spline	TPS	$r^2 \ln \lvert r\rvert$
Piecewise smooth, compact		(for $0 \le r \le \frac{1}{\varepsilon}$; equal to zero for $r > \frac{1}{\varepsilon}$)
Wendland type, order 2	W2	$(1-\varepsilon r)^4(4\varepsilon r+1)$
order 4	W4	$(1-\varepsilon r)^6(\frac{35}{3}(\varepsilon r)^2+6\varepsilon r+1)$
order 6	W6	$(1-\varepsilon r)^8(32(\varepsilon r)^3+25(\varepsilon r)^2+8\varepsilon r+1)$

Table 1
Definitions of some types of radial functions. The shape parameter ε controls their 'flatness'. In the case of the Wendland functions, their 'order' refers to their degree of smoothness (C^2, C^4, C^6 respectively).